The Pennsylvania State University

The Graduate School

Graduate Program in Acoustics

REFLECTION, RADIATION, AND COUPLING OF HIGHER ORDER MODES AT DISCONTINUITIES IN FINITE LENGTH RIGID WALLED RECTANGULAR DUCTS

A Thesis in

Acoustics

by

Ralph T. Muehleisen

Submitted in Partial Fulfillment
of the Requirements
for the Degree of

Doctor of Philosophy

May 1996

We approve the thesis of Ralph T. Muehleisen.

Date of Signature

David C. Swanson Assistant Professor of Acoustics Research Associate Thesis Adviser Chair of Committee	
Jiri Tichy Professor of Acoustics Chairman of the Graduate Program in Acoustics	
Scott D. Sommerfeldt Assistant Professor of Acoustics Research Associate	
Douglas Werner Research Associate	

Abstract

The effects of discontinuities on higher order modes is important in the design of passive and active noise control systems in ducts which operate near or above the cut-off frequency of the duct. Accurate acoustic monitoring of mechanical systems in ducts at frequencies near and above the cut-off frequency of the first mode must include the effects of discontinuities.

This thesis examines the reflection, transmission, and coupling of higher order modes at discontinuities in finite length rigid walled rectangular ducts. Using a method of generalized scattering coefficients, analytic expressions for the reflection and transmission of higher order modes at size discontinuities, junctions, and baffled terminations are developed. A technique to measure the higher order modes is discussed and implemented.

When written in matrix form, the equations for the reflection and transmission coefficients for all three discontinuities take on the standard form for reflection and transmission of plane waves at a change of impedance. For all the examples given, the magnitude of the mutual coupling coefficients can be significant, often larger than that of the self reflection and transmission coefficients, showing that modal coupling must be included when working with models near and above the cut-off frequency of the first higher order mode.

Analytic expressions for the reflection and transmission coefficients of a general multi-port junction are derived in terms of the Green's function of the junction region. Examples of a right angle bend and a T junction are given. It is shown that the magnitude

of the self transmission coefficient for the plane wave mode in the side branch to the end of a T junction is found to have many zeros and the overall magnitude decreases with increasing frequency indicating that side mounted speakers are poor plane wave sources at frequencies near and above the cut-off of the first mode.

Analytic expressions for the radiation impedances and reflection coefficients for the termination of a duct in an infinite baffle are derived. It is shown that the radiation directivity is proportional to the wavenumber transform of the modal velocity. The plane wave mode radiates omni-directionally at low frequencies and begins beaming on axis at higher frequencies. The higher order modes radiate toward the sides, with the main lobes moving toward the axis at higher frequencies. Equations for the total radiated power in terms of the reflection coefficients of the duct termination and the incident modal amplitudes are developed.

Experimental measurements of the reflection coefficients of an infinite baffle are shown to be consistent with theory. Experimental measurements of the reflection and transmission coefficients of a right angle bend are shown to be consistent with the junction theory. The thesis also gives a description of some of the potential problems involved with modal measurement and microphone calibration.

Table of Contents

List of Figures

List of Symbols

A_M, B_M	modal amplitudes of mode M
$\bar{A}, \bar{B}$	modal amplitude vectors
C_M	total amplitude of mode M
$D_M(\phi, \theta)$	radiation directivity function of mode M
$G(\vec{x}\|\vec{x_0})$	Green's function
$\bar{G}$	generalized inverse of $\bar{H}$
H_{RM}	step discontinuity coupling constant from mode M to mode R
$\bar{H}$	step discontinuity coupling constant matrix
K_M	eigenvalue for mode M of an enclosure
L_x, L_y, L_z	duct dimensions
M, N, R, S	mode number pairs or triplets
P_M	modal pressure amplitude
$\bar{P}_M$	modal pressure amplitude matrix
$\bar{P}_{MZ}$	modal pressure amplitude matrix, alternate form
$R(x, y, z)$	position vector
R_{MN}	reflection coefficient from mode N to mode M
$\bar{R}$	reflection matrix
S_{RM}^{li}	scattering parameter between mode M in duct i and mode R in duct l
$\bar{S}^{li}$	scattering matrix from duct i to duct l
T_{MN}	transmission coefficient from mode N to mode M

$\bar{T}$	transmission matrix
Y_M	specific acoustic modal admittance of mode M
$\bar{Y}$	specific acoustic modal admittance matrix
$\bar{Z}_c$	specific acoustic modal impedance matrix
Z_{RM}	mutual modal impedance between modes M and R
$\bar{Z}$	mutual modal impedance matrix
Z_{rRM}	mutual modal radiation impedance between modes M and R
$\bar{Z}_r$	mutual modal radiation impedance matrix
$\mathcal{N}_{subscript}$	number of modes in region *subscript*
$\mathcal{S}_{subscript}$	area of region *subscript*
a, b, c, d	duct dimensions
c	ambient speed of sound in air
j	$\sqrt{-1}$
k	acoustic wavenumber
m_x, n_x, r_x, s_x	mode numbers in the $\hat{x}$ direction
m_y, n_y, r_y, s_y	mode numbers in the $\hat{y}$ direction
m_z, n_z, r_z, s_z	mode numbers in the $\hat{y}$ direction
$\vec{n}$	surface normal vector
$p'(x, y, z, t)$	linear acoustic pressure perturbation
$p(x, y, z, \omega)$	Fourier transform of the linear acoustic pressure perturbation
$\bar{p}$	pressure amplitude matrix
p_M	pressure amplitude of mode M

$r(x, y, z)$	position vector
t	time
$u'(x, y, z, t)$	linear acoustic velocity perturbation
$u(x, y, z, \omega)$	Fourier transform of the linear acoustic velocity perturbation
x, y, z	Cartesian coordinates
x_0, y_0, z_0	source location in Cartesian coordinates
Π_M	power in mode M
Π_+, Π_-	total incident and reflected power
Π_{Rad}	total radiated power
$Psi_M(k_x, k_y)$	spatial Fourier transform of $psi_M(x, y)$
χ_M	eigenvalue of Ψ_M
$\Lambda_{m_x}, \Lambda_{m_y}$	integration constant
δ_{mn}	Kronecker delta function
$\delta_{\vec{x}}$	Dirac delta function at position $\vec{x}$
η_{RM}	normalized mutual modal impedance from mode M to mode R
$\bar{\eta}$	normalized mutual modal impedance matrix
α, β	polar transformation variables
γ_M	propagation constant for mode M
$\psi_M(x, y)$	eigenfunction (mode shape) of mode M
ρ	ambient density of air
ω	radian frequency
ϕ	polar angle in $\hat{x}, \hat{z}$ plane

$\bar{\phi}_+, \bar{\phi}_-$	propagation matrices
θ	polar angle from $\hat{z}$ axis
ζ_{RM}	normalized mutual modal radiation impedance from mode M to mode R
$\bar{\zeta}$	normalized mutual modal radiation impedance matrix
∇	gradient operator
∇^2	Laplacian operator
$matrix^H$	matrix hermitian operator
$\Im\{q\}$	imaginary part of the complex argument q
$\Re\{q\}$	real part of the complex argument q
$matrix^T$	matrix transpose operator

Acknowledgments

I would like to thank "The man of a thousand and one ideas", my advisor, David Swanson. His patience, encouragement, guidance and financial support were essential to the completion of this thesis.

I would like to thank my other thesis committee members for their suggestions and criticism, and especially Doug Werner for his willingness to serve on such short notice.

I thank the other members of Dave Swanson's research group, especially Karl Reichard and Mark Mahon for their overall help in the completion of this thesis.

I want to thank the Applied Research Lab and Dr. Richard Stern for early financial support through the Exploratory and Foundational Research program.

I would like to thank all the wonderful instructors here at Penn State, but in particular I'd like to thank Courtney Burroughs, Gary Koopman, Allan Pierce (despite the 8am classes), Victor Sparrow, Scott Sommerfeldt, Jiri Tichy and William Thompson Jr. for always keeping me thinking and for always being willing to answer even the most stupid questions.

I would like to thank Brian Bourgault of Mathworks for providing a free beta copy of MATLAB for Linux which was used for most of the numerical analysis in the thesis.

Big thanks go to the greatest set of administrative assistants at Penn State, Karen Brooks, Catherine Brown, Barbara Crocken, and Carolyn Smith for all their help throughout the years.

I would like to thank all my fellow students and friends in the Graduate Program in Acoustics for all their support, witty banter, mindless diversions and willingness to help me whenever I needed it, especially Ben Bard, Scott Hansen, Mary Herr, Brian Katz, Doug Koehn, Rod Korte, Tim Leishmann, Andy Mills, Judy Rochat, Tad Rollow, Dan Russell, and Brian Scott. In particular, I'd like to thank Ed "Reverse the Drill" Maniet and Paul "Carriage Bolts" Moran who helped keep me sane during the last few months of work. I wish everyone could have office-mates as great as you two. I would like thank a few former students and other friends who have given me guidance and encouragement: Paul Kovitz, Rob and Tammie Lepage (and the uncountable clan), Russ McMillan, Martin Manley, Doug Mast and Andy Piascek.

I would like to thank my parents, my brother, my Brother-in-law Jerome and my sister Vicky for their encouragement. I especially thank Vicky for letting me finish first.

Most of all I have to thank my dear wife Sally Laurent-Muehleisen. Without her love, encouragement, guidance, patience and example, this thesis could never have been written. This thesis is dedicated to her, with love until love has no meaning.

Chapter 1

Introduction

1.1 Historical Background

1.1.1 Early Work on Reflection and Radiation From Finite Ducts

Research on acoustic waveguides dates back at least as far as Lord Rayleigh [52]. Rayleigh determined the eigenfunctions of infinitely long rigid walled rectangular and circular waveguides. Rayleigh also analytically determined end corrections (from which reflection coefficients can be determined) for low frequency radiation from a baffled circular duct. The analysis was limited to frequencies far below the cut-off frequency of the first higher order mode. Rayleigh did not determine end corrections for rectangular ducts. Rayleigh was unable to determine analytic expressions for end corrections to an unbaffled circular duct, but he did determine empirical expressions.

Analysis of the unbaffled circular duct proved most troublesome. It was not until Levine and Schwinger [32] employed the Weiner-Hopf technique that analytic expressions of the reflection coefficients for an unbaffled circular duct were obtained. However, their analysis was still limited to frequencies below the cut-off frequency of the first higher order mode. This analysis was refined by several authors [42, 47].

Weinstein [68], also employing Weiner-Hopf methods, was able to determine reflection coefficients for higher order modes at the end of an unbaffled circular duct. In addition, Weinstein obtained analytic expressions for the reflection coefficients from the

end of plane parallel waveguides (two semi-infinite parallel plates). Weinstein found that for an incident plane wave above the cut-off frequency of the first higher order mode, the magnitude of the mutual reflection coefficient between the plane wave mode and the first higher order mode can be significantly greater than the magnitude of the plane wave self reflection coefficient. This result showed that coupling between modes at the end of a duct is very important when analyzing wave propagation at higher frequencies.

Unfortunately, the Weiner-Hopf method does not allow one to determine the radiation from the end of rectangular ducts [68]. Even if it did, the mathematics of the Wiener-Hopf method is steeped in the concepts of analytic function theory and is very involved. The results are often difficult to numerically evaluate and meaningful physical interpretation of the results can get lost in the myriad of mathematical symbols.

Zorumski [70] developed the concept of generalized radiation impedances and reflection coefficients for infinitely baffled circular ducts. He developed matrix formulations for the generalized impedance. The method of analysis used in this thesis is similar to the method Zorumski used.

Recently there has been a large number of papers about radiation from baffled and unbaffled circular ducts [22, 37, 48, 67]. Much of the work has been prompted by research in the acoustics of turbofan and turbojet engines.

1.1.2 Early work on other Duct Discontinuities

The low frequency lumped element analysis of acoustic duct discontinuities such as constrictions, bifurcations, and size changes dates back to Rayleigh as well, but an early thorough analysis dates back to Mason's work [36] on acoustical filters.

Miles [38, 39, 40] extended this work to be valid at frequencies much closer to the cut-off frequency of the first higher order mode. He basically used a truncated version of the mode matching technique that Mittra and Lee were to later use in electromagnetic problems. The thrust of Miles' research was to develop more accurate lumped element equivalents of discontinuities.

Soon after Miles' papers appeared, Lippert [33, 34] published his research on modal measurement techniques along with theory and experiments on right angled bends.

Doak's excellent set of papers [18, 19] which discusses higher order modes in rigid walled rectangular ducts, was a thorough analysis of the generation and propagation of higher order modes. However Doak's analysis did not give a good description of the coupling of higher order modes, an effect which is important at any discontinuity when higher order modes can propagate. This paper was an important basis for the analysis of ducting systems and mufflers at higher frequencies. It also rekindled interest in higher order mode research.

Following Doak's work, a number of other papers looking at the propagation and coupling of higher order modes for several different discontinuities in rectangular and circular ducts were written.

Cummings [17] looked at propagation through 180 degree bends. Firth and Fahy [21] and Furnell and Bies [23, 24] both looked at curved bends in ducts.

Said [58] looked at propagation in right angle bends and T junctions. He derived and measured energy coupling coefficients instead of pressure coupling coefficients.

About this same time, the finite element technique began to be applied to acoustic waveguide problems [14, 15]. While this powerful method allows one to determine the

overall propagation through a complicated system, it is difficult to determine quantities like modal amplitudes and coupling coefficients using it. In addition, much of the physics is lost because there are no analytic results, just tables of numbers.

Nevertheless, Shepherd and Cabelli [59, 60] looked at propagation through right angled bends using finite elements. They compared their finite element results to experimental results and showed a high degree of accuracy.

Redmore and Mulholland [54] looked at propagation past a side branch (a T junction) using modal analysis. However, they didn't explicitly derive reflection and transmission coefficients, they simply predicted the pressure at a given point in the side branch.

Working with electromagnetic waveguides, Mittra and Lee [41] developed mode matching techniques which lend themselves to numerical solutions for problems in which the Wiener-Hopf method does not apply. The idea of mode matching techniques at a discontinuity is to expand the solution on either side of the discontinuity in an orthogonal modal series. Using equations of continuity (in acoustics the pressure and normal velocity are usually continuous) a number of simultaneous equations are developed. Through the use of orthogonality the equations can be reduced and solved.

The development of planar microwave waveguide circuits has lead to great advances in scattering theory for microwave junctions using mode matching techniques and generalized scattering parameters. [28, 49, 56]. In particular, MacPhie and Zaghloul published a paper on radiation from a baffled rectangular waveguide [35]. However, the electromagnetic waveguide is different enough from the acoustic waveguide that the work done in microwave research cannot be applied directly to acoustic waveguides. Hudde

[26, 27] has recently begun applying the mode-matching and generalized scattering parameter techniques to acoustic waveguide problems; however, his work has been limited to circular waveguides.

A need to examine propagation at higher frequencies has re-emerged with the development of active noise control systems. Much analysis has been done assuming plane wave propagations. A few researchers have investigated the effects of higher order modes on active control [65], while others have looked at the effects of modal coupling on plane wave propagation [45]. A number of initial investigations into higher order modal control [3, 4, 55, 61, 62, 63, 64] have been made, but none have considered the modal coupling present at discontinuities.

1.2 Motivation for Research and Thesis Goals

While there certainly has not been an absence of work in duct acoustics, there has not been much done on the scattering and coupling of higher order acoustic modes, especially for rectangular ducts.

The main goal of this thesis is to develop a coherent theory of scattering at modal discontinuities. In particular, reflection and transmission coefficients will be determined in terms of generalized scattering parameters and generalized impedances. A few of the calculations will be experimentally verified.

The applications of such theory are numerous. An obvious application is in acoustical analysis of air flow and industrial HVAC systems with large cross sections. Such systems often have higher order mode propagation in them. It is often impractical to add enough damping to an air flow system for the desired acoustic noise reduction. Proper

design of acoustical filters would let the acoustical properties of the ducts themselves reduce the propagated noise. Standard plane wave analysis is an insufficient tool for higher frequency filter design. As active noise control (ANC) strives to make inroads into industry, the bandwidth of such systems will have to be increased to control sound above the cut-off frequency of the ducting system. Proper analysis of modal scattering is essential in the design of an effective higher frequency ANC system. A less obvious application is the acoustical monitoring of mechanical systems, where often the acoustical signal that is desired to be measured is a high frequency signal traveling though a ducting system (e.g. turbofans, fluid piping systems). A knowledge of how the ducting system modifies the acoustic spectrum is essential in acoustical monitoring.

1.3 Thesis Outline

Chapter 2 of the thesis reviews some of the mathematics and physics of duct acoustics and modal analysis. In particular, the chapter discusses the equations governing wave propagation in ducts and discusses their solution in modal form. It develops matrix forms of those same solutions. It also reviews the use of generalized scattering parameters and Green's functions in the solution of acoustic waveguide problems.

Chapter 3 of the thesis derives the scattering parameters for step (size) discontinuity. Examples of symmetric and asymmetric steps in a rectangular waveguide are given.

Chapter 4 of the thesis derives the scattering parameters for multi-port junctions. Right angle bends and T junctions in rectangular waveguides are used as examples. The

analytical results for the right angle bend are compared with the experimental results fo Sheperd and Cabelli [59].

Chapter 5 of the thesis derives expressions for the radiation impedance and reflection coefficients for a duct terminating in an infinite baffle. Numerical results are obtained for a rectangular waveguide. Expressions for the radiated power and directivity of the radiation from the duct termination are developed.

Chapter 6 of the thesis discusses the experimental methods used to investigate radiation from the end of a baffled rectangular duct.

Chapter 7 states some conclusions which can be drawn from the work and gives suggestions for future research.

Chapter 2

Math and Physics Review

This chapter of the thesis will briefly review some of the basic mathematics and physics of duct acoustics and scattering parameters. In particular, it will cover modal decomposition, the edge condition, scattering parameters, matrix notation and Green's functions.

2.1 Modal Decomposition

A linear fluid pressure perturbation $p'(x, y, z)$ inside an acoustic waveguide satisfies the linear acoustic pressure wave equation

$$(\nabla^2 - \frac{1}{c^2}\frac{\partial}{\partial t^2})p'(x, y, z, t) = 0 \tag{2.1}$$

where t represents time and c represents the acoustic speed of sound in the medium. The fluid pressure perturbation, p', and the particle velocity perturbation, u', are related by the linearized momentum equation, also known as Euler's equation

$$\rho\frac{\partial\vec{u}'(x, y, z, t)}{\partial t} = -\nabla p'(x, y, z, t) \tag{2.2}$$

where ρ is the ambient density of the medium.

The linearized wave and Euler's equation can be Fourier transformed in time to yield the constant frequency versions of the equations.

The forward Fourier time transform is defined as

$$F(x,y,z,\omega) = \int_{-\infty}^{\infty} f(x,y,z,t)e^{-jwt}dt. \tag{2.3}$$

The inverse Fourier time transform is defined as

$$f(x,y,z,t) = \frac{1}{2\pi}\int_{-\infty}^{\infty} F(x,y,z,\omega)e^{jwt}d\omega. \tag{2.4}$$

Denoting the Fourier Transform of the linear pressure perturbation p' as p, the Fourier transformed wave equation (also known as the Helmholtz equation) can be written as

$$(\nabla^2 + k^2)p(x,y,z,\omega) = 0 \tag{2.5}$$

where the wavenumber $k = \omega/c$.

Denoting the Fourier transform of the linear velocity perturbation $\vec{u}'$ as $\vec{u}$, the the Fourier transformed form of Euler equation is

$$\vec{u}(x,y,z,\omega) = \frac{j}{k\rho c}\nabla p(x,y,z,\omega). \tag{2.6}$$

The solution to the differential equation 2.5 depends upon the boundary conditions. If the fluid is confined to a rectangular duct with rigid walls at $x = 0$, $x = a$,

$y = 0$, and $y = b$, the normal velocity is zero on each wall. The boundary conditions are then

$$\frac{\partial}{\partial x}p \Big|_{x=0} = \frac{\partial}{\partial x}p \Big|_{x=a} = \frac{\partial}{\partial y}p \Big|_{y=0} = \frac{\partial}{\partial y}p \Big|_{y=b} = 0. \tag{2.7}$$

The pressure can be expressed as an expansion of the eigenfunctions of the partial differential equation. The eigenfunctions are called the modes of the system, and the eigenfunction expansion is called the modal solution.

In the case of a duct constrained in the x and y direction the modal solution for the pressure is

$$p(x, y, z) = \sum_{m_x} \sum_{m_y} (A_{m_x m_y} e^{-\gamma_{m_x m_y} z} + B_{m_x m_y} e^{\gamma_{m_x m_y} z}) \psi_{m_x m_y}(x, y) \tag{2.8}$$

where $\psi_{m_x m_y}$ is the eigenfunction (also known as the duct mode) and the propagation constant $\gamma_{m_x m_y} = \sqrt{\chi^2_{m_x m_y} - k^2}$ where $\chi_{m_x m_y}$ is the eigenvalue associated with $\psi_{m_x m_y}$.

Because the modes are the eigenfunctions of a self-adjoint differential equation, they are real and orthogonal [31, 43, 69]. When the modes are properly normalized, the orthogonality integral takes the form

$$\iint_{\mathcal{S}} \psi_{m_x m_y}(x, y) \psi_{n_x n_y}(x, y) dS = \delta_{m_x n_x} \delta_{m_y n_y} \tag{2.9}$$

where $\mathcal{S}$ is the cross sectional area of the duct and δ_{mn} is the Kronecker delta defined by

$$\delta_{mn} = \begin{cases} 1 & m = n \\ 0 & m \neq n \end{cases} . \tag{2.10}$$

The coefficients $A_{m_x m_y}$ and $B_{m_x m_y}$ in equation 2.8 are called the modal amplitudes. $A_{m_x m_y}$ is the amplitude of the waves traveling in the $+\hat{z}$ direction, while $B_{m_x m_y}$ is the amplitude of the waves traveling in the $-\hat{z}$ direction.

$\psi_{m_x m_y}(x, y)$ are the modes of the duct. They represent standing waves that exist in the $\hat{x}$ and $\hat{y}$ directions of the duct.

For each m_x, m_y there is a frequency at which $\gamma_{m_x m_y}$ is zero. That frequency is called the cut-off frequency. Below the cut-off frequency the mode is called *evanescent* because $\gamma_{m_x m_y}$ is real and the mode no longer propagates, but decays exponentially. The propagation constant $\gamma_{m_x m_y}$ is used instead of the modal wavenumber $k_{m_x m_y} = \sqrt{k^2 - \chi^2_{m_x m_y}}$ because using this notation ensures that evanescent waves are represented with decaying amplitude. To ensure that evanescent modes are represented with decaying amplitude, one must take the negative root of $k^2 - \chi^2_{m_x m_y}$ when $k^2 < \chi^2_{m_x m_y}$, something which is not easily implemented when solving the propagation equations numerically.

For a rectangular duct of sides a and b the normalized mode $\psi_{m_x m_y}$ is given by

$$\psi_{m_x, m_y}(x, y) = \frac{\cos(\frac{m_x \pi}{a} x) \cos(\frac{m_y \pi}{b} y)}{\sqrt{ab \Lambda_{m_x} \Lambda_{m_y}}} \tag{2.11}$$

where the integration constant Λ_{m_x} is given by

$$\Lambda_{m_x} = \begin{cases} 1 & m_x = 0 \\ \\ \frac{1}{2} & m_x > 0 \end{cases} . \tag{2.12}$$

For the same duct the propagation number is given by

$$\gamma_{m_x m_y} = \sqrt{(\frac{m_x \pi}{a})^2 + (\frac{m_y \pi}{b})^2 - k^2}. \tag{2.13}$$

Because nearly all the summations in this thesis will be double or triple summations (for the x, y, and z modes), a new terminology will be used. Capital letters will be used to denote summation pairs or triplets. For example, M refers to $m_x m_y$ or $m_x m_y m_z$ and N to $n_x n_y$ or $n_x n_y n_z$.

With the new summation notation equations 2.8 through 2.13 become

$$p(x,y,z) = \sum_M (A_M e^{-\gamma_M z} + B_M e^{\gamma_M z}) \psi_M(x,y) \tag{2.14}$$

$$\psi_M(x,y) = \frac{\cos(\frac{m_x \pi}{a} x) \cos(\frac{m_y \pi}{b} y)}{\sqrt{ab \Lambda_{m_x} \Lambda_{m_y}}} \tag{2.15}$$

and

$$\gamma_M = \sqrt{(\frac{m_x \pi}{a})^2 + (\frac{m_y \pi}{b})^2 - k^2}. \tag{2.16}$$

The axial velocity, u_z, in the duct can be determined using Euler's equation. Application of Euler's equation to equation 2.14 yields

$$u_z(x,y,z) = \sum_M Y_M (A_M e^{-\gamma_M z} - B_M e^{\gamma_M z}) \psi_M(x,y) \tag{2.17}$$

where the specific modal admittance Y_M is given by

$$Y_M = \frac{-j\gamma_M}{k\rho c}. \tag{2.18}$$

The specific modal admittance is the ratio of the acoustic velocity to the acoustic pressure for a particular mode propagating in one direction in an infinite duct.

2.2 Matrix Notation

Many of the modal summations can be more simply represented as matrix multiplications. With a more simple representation the physics of the problem should be easier to see. In addition, the matrix representation is easily coded when using a higher level language like MATLAB.

First, a number of vectors and matrices must be defined. Let

$$\bar{A} = \begin{bmatrix} A_0 \\ A_1 \\ \vdots \end{bmatrix} \quad \bar{B} = \begin{bmatrix} B_0 \\ B_1 \\ \vdots \end{bmatrix} \quad \bar{\psi} = \begin{bmatrix} \psi_0(x,y) \\ \psi_1(x,y) \\ \vdots \end{bmatrix} \quad \bar{Y} = \begin{bmatrix} Y_0 & 0 & \cdots \\ 0 & Y_1 & \cdots \\ \vdots & \vdots & \ddots \end{bmatrix} \tag{2.19}$$

$$\bar{\phi}_- = \begin{bmatrix} e^{-\gamma_0 z} & 0 & \cdots \\ 0 & e^{-\gamma_1 z} & \cdots \\ \vdots & \vdots & \ddots \end{bmatrix} \quad \bar{\phi}_+ = \begin{bmatrix} e^{\gamma_0 z} & 0 & \cdots \\ 0 & e^{\gamma_1 z} & \cdots \\ \vdots & \vdots & \ddots \end{bmatrix}. \tag{2.20}$$

With these definitions, and noting that ^{T} denotes the transpose operation, equation 2.14 can be rewritten

$$p(x,y,z) = \bar{\psi}^T \bar{\phi}_- \bar{A} + \bar{\psi}^T \bar{\phi}_+ \bar{B} \tag{2.21}$$

and equation 2.17 can be rewritten

$$u_z(x,y,z) = \bar{\psi}^T \bar{Y} \bar{\phi}_- \bar{A} - \bar{\psi}^T \bar{Y} \bar{\phi}_+ \bar{B}. \tag{2.22}$$

2.3 Generalized Scattering Parameters

When a propagating mode meets a discontinuity, part of it is reflected and part of it is transmitted. The magnitude and phase of the reflected and transmitted modes can be calculated if one knows the reflection and transmission coefficients. If the discontinuity is a multiple port junction, there are a number of reflection and transmission coefficients. The generalized relationships between the incident and reflected modes at the junction are called the scattering parameters. The linear relationships can often be written in matrix form in which case the matrix is called the scattering matrix [10, 11, 27, 28, 46]

Consider an N port junction as shown in figure 2.1 . If a mode in section i is incident on the junction, many different modes may be reflected in section i and transmitted to the other sections. The ratio of the magnitude of the reflected or transmitted mode Q in section l to the incident mode M in section i is S^{li}_{QM}. Thus, between a particular

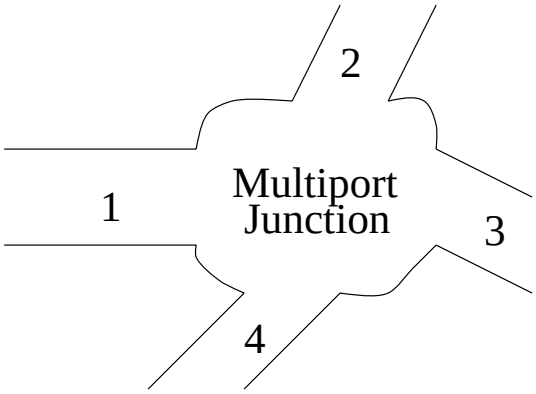

Fig. 2.1. A general N port junction

incident and reflected or transmitted mode

$$B_Q^l = S_{QM}^{li} A_M^i. \tag{2.23}$$

By defining a matrix

$$\bar{S}^{li} = \begin{bmatrix} S_{00}^{li} & S_{01}^{li} & \cdots \\ S_{10}^{li} & S_{11}^{li} & \cdots \\ \vdots & \vdots & \ddots \end{bmatrix} \tag{2.24}$$

one can write an equation which relates all the incident modes to all the reflected and transmitted modes. Defining $\bar{A}^i$ and $\bar{B}^i$ as the incident and reflected modal amplitude

vectors in the ith section this equation is

$$\begin{bmatrix} \bar{B}^1 \\ \bar{B}^2 \\ \vdots \\ \bar{B}^N \end{bmatrix} = \begin{bmatrix} \bar{S}^{11} & \bar{S}^{12} & \dots & \bar{S}^{1N} \\ \bar{S}^{21} & \bar{S}^{22} & \dots & \bar{S}^{2N} \\ \vdots & \vdots & \ddots & \vdots \\ \bar{S}^{N1} & \bar{S}^{N2} & \dots & \bar{S}^{NN} \end{bmatrix} \begin{bmatrix} \bar{A}^1 \\ \bar{A}^2 \\ \vdots \\ \bar{A}^N \end{bmatrix}. \tag{2.25}$$

2.4 Edge Condition

When doing numerical computations using modal analysis, the infinite sums and infinite dimension matrices developed earlier must be truncated to a finite size. When working with modal expansions in two connected regions one must be very careful about the number of modes which are used in each region. Early work with electromagnetic waves showed a phenomenon known as relative convergence, whereby the solution converges to different values depending upon how the modal decomposition was truncated. By changing the ratio of number of modes in each region, different solutions were obtained.

It has been found that relative convergence is related to the violation of energy relations at the edge of a discontinuity [28, 41]. By imposing conservation of energy at the boundary, specific ratios of the number of modes required in each region can be developed. For regions of similar geometry (i.e circular to circular, rectangular to rectangular) Mittra and Lee found that the ratio of number of modes was the same as the ratio of the characteristic sizes. For example, when dealing with two circular ducts with a radius ratio of 2:1 the number of modes must be 2:1.

2.5 Green's Functions

Solving the wave equation with finite sized sources can sometimes be a daunting task. One of the more powerful techniques for solving boundary value problems like those posed by duct acoustics is the use of Green's functions [2, 12, 13, 31, 43, 44, 50, 69]. The use of Green's functions will be essential for determining reflection and transmission at junctions and reflection and radiation from the end of the duct.

A Green's function $G(\vec{x}|\vec{x_0})$ for the Helmholtz equation satisfies the inhomogeneous differential equation

$$(\nabla^2 + k^2)G(\vec{x}|\vec{x_0}) = -\delta(\vec{x} - \vec{x_0}). \tag{2.26}$$

In acoustics, the Green's function $G(\vec{x}|\vec{x_0})$ describes the propagation of radiation from a point source at $\vec{x_0}$ to the point $\vec{x}$. The pressure at $\vec{x}$ radiated from a vibrating region of space $\mathcal{S}_0$ propagating through a region with a Green's function $G(\vec{x}|\vec{x_0})$ can be determined using the Kirchoff-Helmholtz integral theorem [30, 44, 50] which states

$$p(\vec{x}) = -\iint_{\mathcal{S}_0} [G(\vec{x}|\vec{x_0})\nabla p(\vec{x_0}) - p(\vec{x_0})\nabla G(\vec{x}|\vec{x_0})] \cdot \vec{n} d\mathcal{S}_0 \tag{2.27}$$

where $\vec{n}$ is the surface normal and $\mathcal{S}_0$ is the radiating surface area.

For a point source in free space the Green's function can be shown to be [44, 50]

$$G(\vec{x}|\vec{x_0}) = \frac{e^{jkr}}{4\pi r} \tag{2.28}$$

where $r = \sqrt{(x-x_0)^2 + (y-y_0)^2 + (z-z_0)^2}$.

If the point source is above a rigid plane the particle velocity at the rigid plane must be zero. A new Green's function can be developed through the use of image sources which satisfies this boundary condition. If the source is located on the rigid plane (not just above) at $z_0 = 0$ a suitable Green's function is [44, 50]

$$G(\vec{x}|\vec{x_0}) = \frac{e^{jkr}}{2\pi r} \tag{2.29}$$

where $r = \sqrt{(x-x_0)^2 + (y-y_0)^2 + z^2}$.

This Green's function has the property that $\nabla g(\vec{x}|\vec{x_0}) \cdot \hat{z} = 0$ on the plane $z = 0$. Thus when equation 2.29 is used, equation 2.27 reduces to

$$p(\vec{x}) = jk\rho c \iint_{\mathcal{S}_0} u_z(\mathcal{S}_0) G(\vec{x}|\vec{x_0}) d\mathcal{S}_0. \tag{2.30}$$

This equation is known as the Rayleigh Integral. It is an indispensable equation for determining the radiation from a planar region in an infinite baffle.

If the source is inside an enclosure instead of in free space the Green's function can be found as an expansion of modes of the enclosure [44, 50]

$$G(\vec{x}|\vec{x_0}) = \sum_{m_x} \sum_{m_y} \sum_{m_z} \frac{\phi_{m_x m_y m_z}(\vec{x}) \phi_{m_x m_y m_z}(\vec{x_0})}{K^2_{m_x m_y m_z} - k^2} = \sum_{M} \frac{\phi_M(\vec{x}) \phi_M(\vec{x_0})}{K^2_M - k^2} \tag{2.31}$$

For a rigid walled parallelepiped with sides $x = L_x$, $y = L_y$, $z = L_z$ the modes ϕ_M are given by

$$\phi_M(\vec{x}) = \phi_{m_x m_y m_z}(\vec{x}) = \frac{\cos(\frac{m_x \pi}{L_x} x)\cos(\frac{m_y \pi}{L_y} y)\cos(\frac{m_z \pi}{L_z} z)}{\sqrt{L_x L_y L_z \Lambda_{m_x} \Lambda_{m_y} \Lambda_{m_z}}}. \tag{2.32}$$

The eigenvalue K_M is given by

$$K_M = K_{m_x m_y m_z} = \sqrt{(\frac{m_x \pi}{L_x})^2 + (\frac{m_y \pi}{L_y})^2 + (\frac{m_z \pi}{L_z})^2}. \tag{2.33}$$

For an enclosure, the Green's function has the property that $\nabla G \cdot \vec{n} = 0$ on the walls of the enclosure. If the only acoustic source is the normal surface velocity of the enclosure, the pressure anywhere within the enclosure is given by

$$p(\vec{x}) = jk\rho c \iint_{\mathcal{S}_0} G(\vec{x}|\vec{x_0}) u_n(\mathcal{S}_0) d\mathcal{S}_0 \tag{2.34}$$

where $\mathcal{S}_0$ is the surface of the enclosure.

Chapter 3

Modal Scattering at Step Discontinuities

Two of the discontinuities present in many ducting systems are constrictions and expansions - changes in the area of the duct. This is known in the microwave field as a step discontinuity. Step discontinuities are essential parts of acoustical filter design.

This chapter of the thesis will present a thorough analysis of the reflection and transmission of different modes at a step discontinuity. Using the formalism of generalized scattering parameters, both the constriction and expansion problems can be solved at the same time.

3.1 General Step Discontinuity Theory

A general step discontinuity is shown in figure 3.1. Consider a change of size in an infinite duct at $z = 0$. The main duct, in region 1, has a cross sectional area $\mathcal{S}_1$. The smaller duct, in region 2, has a cross sectional area $\mathcal{S}_1$. The area at $z = 0$ of $\mathcal{S}_1$ outside $\mathcal{S}_2$ will be denoted $\mathcal{S}_3$. In region 1 modes A^1_M are incident on the junction and B^1_M are traveling away from it. In region 2 modes A^2_M are incident on the junction and B^2_M are traveling away from it.

Using the notation of chapter 2, the pressure in region 1 and 2 can be written

$$p^1(x, y, z) = \sum_M (A^1_M e^{-\gamma^1_M z} + B^1_M e^{\gamma^1_M z})\psi^1_M(x, y) \tag{3.1}$$

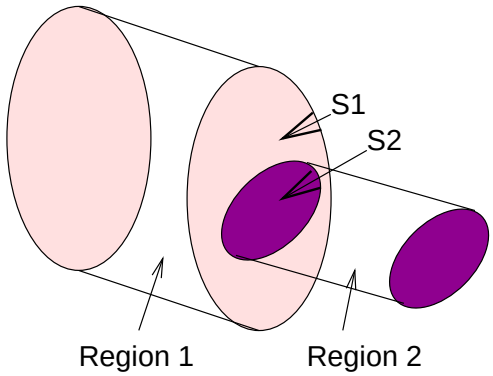

Fig. 3.1. Geometry of the Stepped Duct in Example 3.4.1.

and

$$p^2(x,y,z) = \sum_M (A_M^2 e^{\gamma_M^2 z} + B_M^2 e^{-\gamma_M^2 z})\psi_M^2(x,y). \tag{3.2}$$

The modes traveling away from the junction, B_M^1 and B_M^2, are made up of modes reflected and transmitted the modes that were incident on the junction. Thus they can be rewritten as

$$B_M^1 = \sum_N S_{MN}^{11} A_N^1 + S_{MN}^{12} A_N^2 \tag{3.3}$$

and

$$B_M^2 = \sum_N S_{MN}^{22} A_N^2 + S_{MN}^{21} A_N^1. \tag{3.4}$$

S_{MN}^{11} and S_{MN}^{22} are the reflection coefficients in regions 1 and 2 between incident mode N and reflected mode M while S_{MN}^{12} and S_{MN}^{21} are the transmission coefficients from region 2 mode N to region 1 mode M and region 1 mode N to region 2 mode M,

respectively. By solving for S^{11}_{MN} and S^{21}_{MN} the reflection and transmission coefficients for a constriction are found. By solving for S^{22}_{MN} and S^{12}_{MN} the reflection and transmission coefficients for an expansion are found.

Using equations 3.3 and 3.4, equation 3.1 and 3.2 can be rewritten as

$$p^1(x,y,z) = \sum_M (A^1_M e^{-\gamma^1_M z} + \sum_N [S^{11}_{MN} A^1_N + S^{12}_{MN} A^2_N] e^{\gamma^2_M z}) \psi^1_M(x,y) \tag{3.5}$$

and

$$p^2(x,y,z) = \sum_M (A^2_M e^{\gamma^2_M z} + \sum_N [S^{22}_{MN} A^2_N + S^{21}_{MN} A^1_N] e^{-\gamma^2_M z}) \psi^2_M(x,y). \tag{3.6}$$

Using Euler's equation, the velocity in the $+\hat{z}$ direction is found to be

$$u^1_z(x,y,z) = \sum_M Y^1_M (A^1_M e^{-\gamma^1_M z} - \sum_N [S^{11}_{MN} A^1_N + S^{12}_{MN} A^2_N] e^{\gamma^1_M z}) \psi^1_M(x,y) \tag{3.7}$$

and

$$u^2_z(x,y,z) = \sum_M Y^2_M (-A^2_M e^{\gamma^2_M z} + \sum_N [S^{22}_{MN} A^2_N + S^{21}_{MN} A^1_N] e^{-\gamma^2_M z}) \psi^2_M(x,y). \tag{3.8}$$

At $z = 0$ the pressure and normal velocity are continuous across $\mathcal{S}_2$ so

$$\begin{aligned} p^1(x,y) &= \sum_M (A^1_M + \sum_N [S^{11}_{MN} A^1_N + S^{12}_{MN} A^2_N]) \psi^1_M(x,y) \\ = \quad p^2(x,y) &= \sum_M (A^2_M + \sum_N [S^{22}_{MN} A^2_N + S^{21}_{MN} A^1_N]) \psi^2_M(x,y) \end{aligned} \tag{3.9}$$

and

$$u_z^1(x,y) = \sum_M Y_M^1 (A_M^1 - \sum_N [S_{MN}^{11} A_N^1 + S_{MN}^{12} A_N^2]) \psi_M^1(x,y)$$

$$= \quad u_z^2(x,y) = \sum_M Y_M^2 (-A_M^2 + \sum_N [S_{MN}^{22} A_N^2 + S_{MN}^{21} A_N^1]) \psi_M^2(x,y). \qquad (3.10)$$

If equation 3.9 is multiplied by ψ_R^2 and integrated across the interface ($\mathcal{S}_2$), the sum on the right hand side will be eliminated because of the orthogonality of the modes in region 2. Equation 3.9 then becomes

$$\sum_M H_{RM} (A_M^1 + \sum_N [S_{MN}^{11} A_N^1 + S_{MN}^{12} A_N^2]) = A_R^2 + \sum_N [S_{RN}^{22} A_N^2 + S_{RN}^{21} A_N^1] \qquad (3.11)$$

where the coupling constant H_{RM} is defined as

$$H_{RM} = \frac{\iint_{\mathcal{S}_2} \psi_R^2(x,y) \psi_M^1(x,y) dxdy}{\iint_{\mathcal{S}_2} (\psi_R^2(x,y))^2 dxdy}$$

$$= \iint_{\mathcal{S}_2} \psi_R^2(x,y) \psi_M^1(x,y) dxdy. \qquad (3.12)$$

The normal velocity at $z = 0$ over the area $\mathcal{S}_3$ (part of $\mathcal{S}_1$ outside of $\mathcal{S}_2$) is zero. From this constraint it follows that for any function $f(x,y)$

$$\iint_{\mathcal{S}_2} u_z^1(x,y,0) f(x,y) dxdy = \iint_{\mathcal{S}_1} u_z^1(x,y,0) f(x,y) dxdy. \qquad (3.13)$$

If equation 3.10 is multiplied by ψ_R^1 and integrated across the interfaces ($\mathcal{S}_2$) and if the integration over the left side of equation 3.10 is extended using equation 3.13, the

sum on the left hand side will be eliminated because of the orthogonality of the modes in region 1. Thus equation 3.10 reduces to

$$Y_M^1(A_R^1 - \sum_N [S_{RN}^{11} A_N^1 + S_{RN}^{12} A_N^2]) = \sum_M H_{MR} Y_M^2 (-A_M^2 + \sum_N [S_{MN}^{22} A_N^2 + S_{MN}^{21} A_N^1]). \quad (3.14)$$

These equations can be rewritten using the matrix notation of chapter 2. First however, a few new matrices must be defined; let the scattering matrix $\bar{S}$ and the coupling matrix $\bar{H}$ be defined as

$$\bar{S}^{\mu\nu} = \begin{bmatrix} S_{00}^{\mu\nu} & S_{01}^{\mu\nu} & \cdots \\ S_{10}^{\mu\nu} & S_{11}^{\mu\nu} & \cdots \\ \vdots & \vdots & \ddots \end{bmatrix} \quad \bar{H} = \begin{bmatrix} H_{00} & H_{01} & \cdots \\ H_{10} & H_{11} & \cdots \\ \vdots & \vdots & \ddots \end{bmatrix}. \quad (3.15)$$

With these definitions equations 3.11 and 3.14 become

$$\bar{H}(\bar{I} + \bar{S}^{11})\bar{A}^1 + \bar{H}\bar{S}^{12}\bar{A}^2 = (\bar{I} + \bar{S}^{22})\bar{A}^2 + \bar{S}^{21}\bar{A}^1 \quad (3.16)$$

and

$$\bar{Y}^1(\bar{I} - \bar{S}^{11})\bar{A}^1 - \bar{Y}^1\bar{S}^{12}\bar{A}^2 = \bar{H}^T\bar{Y}^2(\bar{S}^{22} - \bar{I})\bar{A}^2 + \bar{H}^T\bar{Y}^2\bar{S}^{21}\bar{A}^1. \quad (3.17)$$

These equations hold for arbitrary $\bar{A}^1$ and $\bar{A}^2$. By setting $\bar{A}^2 = 0$ one finds

$$\bar{S}^{11} = (\bar{Y}^1 + \bar{H}^T\bar{Y}^2\bar{H})^{-1}(\bar{Y}^1 - \bar{H}^T\bar{Y}^2\bar{H}) \quad (3.18)$$

and

$$\bar{S}^{21} = \bar{H}(\bar{I} + \bar{S}^{11}). \tag{3.19}$$

By setting $\bar{A}^1 = 0$ and defining the generalized inverse of $\bar{H}$ as $\bar{G} = (\bar{H}^T\bar{H})^{-1}\bar{H}^T$ one finds

$$\bar{S}^{22} = 2(\bar{Y}^2 + \bar{G}^T\bar{Y}^1\bar{G})^{-1}(\bar{Y}^2 - \bar{G}^T\bar{Y}^1\bar{G}) \tag{3.20}$$

and

$$\bar{S}^{12} = \bar{G}(\bar{I} + \bar{S}^{22}). \tag{3.21}$$

Equations 3.18 and 3.20 have a very familiar form. The equations for S^{11} and S^{22} are the same form as that for reflection of a plane wave in a medium with a characteristic admittance y_a incident on a medium with an admittance y_b, i.e. $z = (y_a - y_b)/(y_a + y_b)$. Thus one can identify $\bar{H}^T\bar{Y}^2\bar{H}$ as the equivalent impedance matrix seen from region 1 looking toward the discontinuity and $\bar{G}^T\bar{Y}^1\bar{G}$ as the equivalent impedance as seen from region 2 looking toward the discontinuity. Since $\bar{Y}^1$ and $\bar{Y}^2$ are diagonal matrices one can also see that all the mutual modal coupling is contained in the $\bar{H}$ and $\bar{H}^T$ matrices.

3.2 Numerical Considerations

In numerically solving for $\bar{S}^{\mu\nu}$, the summations (and hence the matrix size) must be finite. As indicated in chapter 2, in order for the truncated solution to converge toward the exact value, the number of modes in each region is not arbitrary - a certain ratio is required to achieve convergence. As an example, consider region 1 to be a rectangular duct of dimensions a_1, b_1 and region 2 to be a rectangular duct of dimensions a_2, b_2. If

$\mathcal{N}_{1x}$ and $\mathcal{N}_{1y}$ denote the number of modes in the x direction and y direction of region 1, and $\mathcal{N}_{2x}$ and $\mathcal{N}_{2y}$ the number of modes in the x and y direction in region 2 the ratios are $\mathcal{N}_{1x}/\mathcal{N}_{2x} = a_1/a_2$ and $\mathcal{N}_{1y}/\mathcal{N}_{2y} = b_1/b_2$. Thus the total number of modes is $\mathcal{N}_1 = \mathcal{N}_{1x}\mathcal{N}_{1y}$ in region 1 and $\mathcal{N}_2 = \mathcal{N}_{2x}\mathcal{N}_{2y}$ in region 2.

In addition, there are alternate forms of equations 3.18 to 3.20. The form used above was chosen because it helps to show the physics of the problem by drawing analogies to known situations. However, it requires computing several $\mathcal{N}_1$x$\mathcal{N}_1$ matrix inversions, one being a generalized inverse which can often be difficult. Defining $\bar{Z}_c^1$ as $(\bar{Y}^1)^{-1}$, equations 3.18 to 3.20 can be rewritten as

$$\bar{S}^{11} = \bar{I} - \bar{Z}_c^1 \bar{H}^T \bar{Y}^2 \bar{S}^{21}, \tag{3.22}$$

$$\bar{S}^{21} = 2(\bar{H}\bar{Z}_c^1 \bar{H}^T \bar{Y}^2 + \bar{I})^{-1} \bar{H}, \tag{3.23}$$

$$\bar{S}^{22} = (\bar{H}\bar{Z}_c^1 \bar{H}^T \bar{Y}^2 + \bar{I})^{-1} (\bar{H}\bar{Z}_c^1 \bar{H}\bar{Y}^2 - \bar{I}), \tag{3.24}$$

and

$$\bar{S}^{12} = \bar{Z}_c^1 \bar{H}^T (\bar{I} - \bar{S}^{22}). \tag{3.25}$$

In this form only one inversion of an $\mathcal{N}_2$x$\mathcal{N}_2$ matrix is required (recall that $\mathcal{N}_2 < \mathcal{N}_1$ and note that $\bar{Z}_c$ isn't counted because $\bar{Y}$ is diagonal in inversion is simple). The computational workload has been extremely reduced by eliminating several time consuming matrix inversions and since the matrix being inverted is smaller, accuracy should be increased - especially if the matrices being inverted are close to singular.

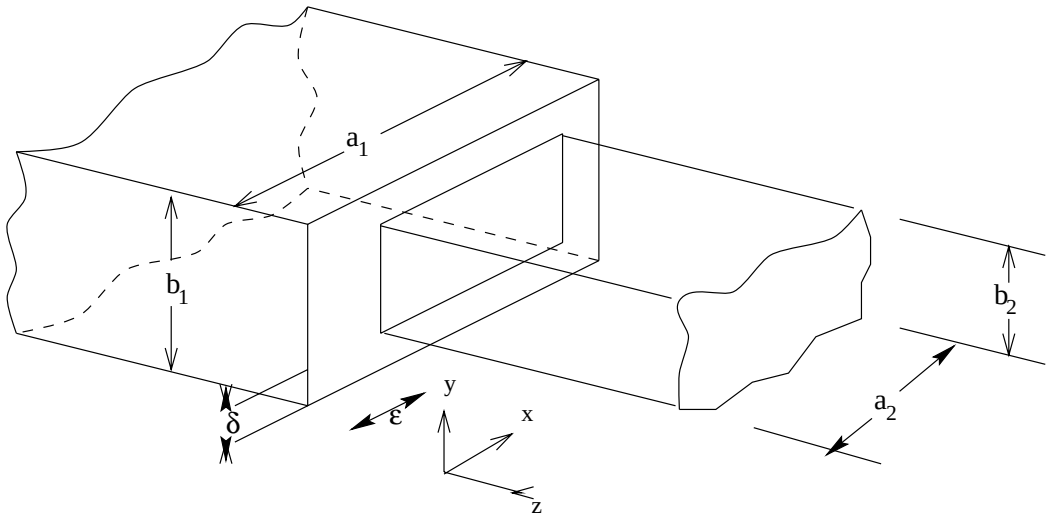

Fig. 3.2. Geometry of a General Rectangular Stepped Duct

3.3 Coupling Matrix H_{RM} for a Rectangular Duct

The term H_{RM} is an integral which, for a rectangular duct, is straightforward to do analytically. However, it is probably easiest to factor H_{RM} into x and y terms first. Consider region 1 to be a duct of size a_1, b_1 and region 2 to be a duct of size a_2, b_2 offset ϵ, δ from region 1 as shown in figure 3.2. Equation 3.12 becomes

$$H_{RM} = H_{Xr_x m_x} H_{Yr_y m_y} \tag{3.26}$$

where

$$H_{Xr_x m_x} = \frac{1}{\sqrt{a_1 a_2 \Lambda_{m_x} \Lambda r_y}} \int_{\epsilon}^{\epsilon + a_2} \cos(\frac{m_x \pi}{a_1} x) \cos(\frac{r_x \pi}{a_2}(x - \epsilon)) dx \tag{3.27}$$

and

$$H_{Yr_ym_y} = \frac{1}{\sqrt{b_1 b_2 \Lambda_{m_y} \Lambda r_y}} \int_{\delta}^{\delta+b_2} \cos(\frac{m_y \pi}{b_1} y) \cos(\frac{r_y \pi}{b_2}(y-\delta)) dy. \tag{3.28}$$

In general, the integrals yield

$$H_{Xr_xm_x} = \frac{a_2\sqrt{a_1 a_2}\, m_x}{\pi\sqrt{\Lambda m_x \Lambda r_x}} \frac{(-1)^{r_x} \sin(\frac{m_x\pi}{a_1}(a_2+\epsilon)) - \sin(\frac{m_x\pi}{a_1}\epsilon)}{(m_x a_2)^2 - (r_x a_1)^2} \tag{3.29}$$

$$H_{Yr_ym_y} = \frac{b_2\sqrt{b_1 b_2}\, m_y}{\pi\sqrt{\Lambda m_x \Lambda r_x}} \frac{(-1)^{r_y} \sin(\frac{m_y\pi}{b_1}(b_2+\delta)) - \sin(\frac{m_y\pi}{b_1}\delta)}{(m_y b_2)^2 - (r_y b_1)^2}. \tag{3.30}$$

When $m_x = r_x a_1/a_2$ the first integral yields

$$H_{Xr_xm_x} = \sqrt{\frac{a_1}{a_2}}\, \cos(\frac{m_x\pi}{a_1}\epsilon). \tag{3.31}$$

When $m_y = r_y b_1/b_2$ the second integral yields

$$H_{Yr_ym_y} = \sqrt{\frac{b_2}{b_1}}\, \cos(\frac{m_y\pi}{b_1}\delta). \tag{3.32}$$

It should be noted that equation 3.31 holds even when $m_x = 0$ and 3.32 holds even when $m_y = 0$.

When $m_x = 0$ but $r_x \neq 0$ or $m_y = 0$ but $r_y \neq 0$

$$H_{RM} = 0. \tag{3.33}$$

3.4 Examples

To demonstrate applications of the theory, two examples will be developed. First is an asymmetric duct. This duct is commonly used for example problems in microwave theory [28, 41]. The second problem is a symmetric duct which is probably a more common size change found in industrial ducting systems. It has also been investigated by microwave waveguide researchers [56, 57].

3.4.1 An Asymmetric Stepped Duct

Consider a duct as shown in figure 3.3. At $z = 0$ the duct changes from a duct with $0 < x < a$ to a duct with $0 < x < a/2$. To simplify the calculation, only a discontinuity in the x direction is considered. Since there is no discontinuity in the y direction, all the y dependence and terms in the problem will drop out.

Figure 3.4 shows the magnitude of the pressure self reflection coefficients of an asymmetric constriction. The magnitude of the plane wave coefficient, $|S_{00}^{11}|$, approaches 1/3 at low frequencies. That is the expected value obtained from the standard low frequency analysis which can be used as a limiting check for the theory presented here. The plane wave coefficient increase with frequency, reaching unity at $ka = \pi$, the cut-off frequency of the first horizontal mode. At that frequency the magnitude of the first mode self reflection coefficient, $|S_{11}^{11}|$, is also unity. Above the cut-off frequency of the mode the first mode coefficient magnitude quickly drops to a small value. The reflection coefficient of the second mode, $|S_{22}^{11}|$, is not unity at its cut-off frequency, but is about 1/3. Above the cut-off frequency it rises.

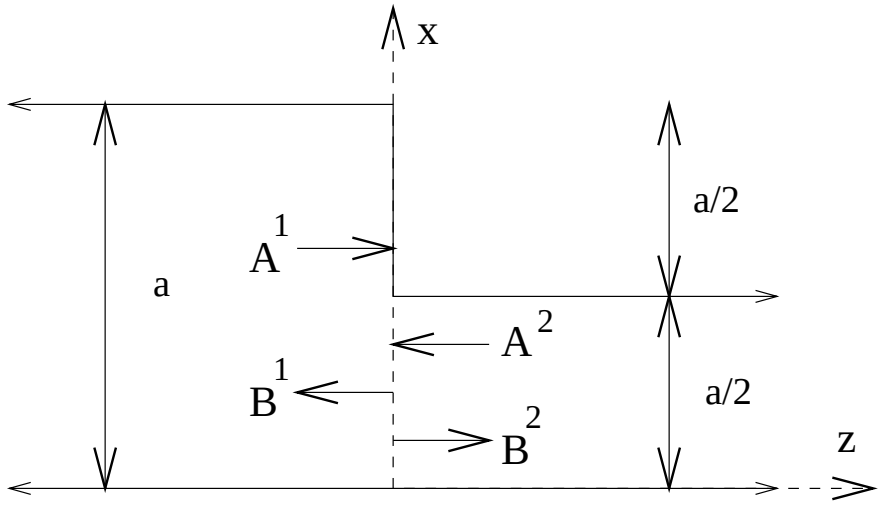

Fig. 3.3. Geometry of the Asymmetric Stepped Duct in Example 3.4.1.

Figure 3.5 shows the phase of the self reflection coefficients of an asymmetric constriction. The phase of the plane wave reflection coefficient is pretty close to π for all frequencies. So, at the cut-off frequency of the first mode, when the magnitude is unity, the constriction looks like a pressure release surface to the plane wave mode. The phase of the first mode coefficient is zero at the cut-off frequency however, so at the cut-off frequency of that mode, the constriction looks like a rigid termination. The phase of the second mode coefficient is about π for all frequencies.

Figure 3.6 shows the magnitude of the pressure self reflection coefficients of an asymmetric expansion. At low frequencies the magnitude of the plane wave reflection coefficient, $|S_{00}^{22}|$, approaches 1/3, the value obtained from the standard low frequency analysis. It rises to unity at the cut-off frequency of the first mode. The magnitude of the first mode reflection coefficient, $|S_{11}^{22}|$, approaches 0.3 at its cut-off frequency and

rises more above the cut-off frequency of the second mode. The magnitude of the second mode reflection coefficient, $|S_{22}^{22}|$, stays about 0.15 until close to the cut-off frequency of the third mode.

Figure 3.7 shows the phase of the pressure self reflection coefficients of an asymmetric expansion. The phase of the plane wave reflection coefficient starts at π but drops to zero at the cut-off frequency of the first mode. Since the magnitude is unity there, at the cut-off frequency of the first mode, the expansion looks like a rigid termination to the plane wave. Above the cut-off frequency of the first mode the phase stays close to zero. The phase of the first mode reflection coefficient starts at zero, goes through $\pi/2$ at the cut-off frequency of the mode and goes through π at the cut-off frequency of the second mode. The phase of the second mode reflection coefficient stays pretty close to zero until close to the cut-off frequency of the third mode.

Figure 3.8 shows the magnitude of the pressure self transmission coefficients from region 1 to region 2. The plane wave mode transmission and the first mode transmission drops to zero at the cut-off frequency of the first mode. The transmission coefficient of the second mode is zero at its cut-off frequency, rising at higher frequencies. So, at the cut-off frequency of the first mode, there is little transmission.

Figure 3.9 shows the magnitude of the pressure self transmission coefficients from region 2 to region 1. The plane wave mode transmission drops to zero at the cut-off frequency of the first mode but then rises again. The first mode transmission coefficient is well transmitted near its cut-off frequency, but the transmission drops to zero at the cut-off frequency of the second mode.

Figure 3.10 shows the magnitude of the mutual pressure reflection and transmission coefficients from the plane wave mode to the first mode. There is significant coupling to the first mode from a plane wave mode incident from region 1 and region 2. All the coefficients have local peaks near the cut-off frequency of the first mode. The mutual reflection coefficient, S_{10}^{11}, is larger than unity, which at first might seem to be impossible, but only the self reflection coefficients cannot exceed unity, mutual reflection coefficients can exceed unity if the coefficient is for a plane wave mode to a higher order mode because the plane wave mode carries more energy than the higher order modes with the same amplitude, thus the pressure coupling coefficient may be greater than unity but the energy transfer coefficient will not be. With coupling coefficients approaching and exceeding unity, it is easy to see that modal coupling is not negligible.

Figure 3.11 shows the magnitude of the mutual pressure reflection and transmission coefficients from the first mode to the plane wave mode. The reflection and transmission coefficients in region 1 go to zero at the cut-off frequency of the first mode. The reflection and transmission coefficients in region 2 are largest at the cut-off frequency of the first mode but they go to zero at the cut-off frequency of the second mode. There is significant coupling from the first mode to the plane wave mode incident in region 2 near the cut-off frequency of the first mode and in region I above the cut-off frequency of the first mode.

Figure 3.12 shows the magnitude of the mutual pressure reflection and transmission coefficients from the plane wave mode to the second mode. All the coefficients have a local peak at the cut-off frequency of the first mode. Recall however, that the second

mode can not yet propagate at that frequency. All the coefficients rise again at the cut-off frequency of the third mode. The overall level is quite low however.

Figure 3.13 shows the magnitude of the mutual pressure reflection and transmission coefficients from the second mode to the plane wave mode. All the coefficients peak at the cut-off frequency of the first mode, below the cut-off frequency of the second mode. All the coefficients are zero at the cut-off frequency of the second mode. The only significant peak is below the cut-off frequency of the second mode.

Figure 3.14 shows the magnitude of the mutual pressure reflection and transmission coefficients from the first mode to the second mode. Most of the coefficients are zero at the cut-off frequency of the first mode. There is significant transmission of the first mode in region 1 to the second mode in region 2.

Figure 3.15 shows the magnitude of the mutual pressure reflection and transmission coefficients from the second mode to the first mode. At the cutoff frequency of the second mode the mutual reflection coefficient in region 1 is zero and remains a low value for higher frequencies, while the transmission coefficient from region 2 to 1 approaches unity and remains high for higher frequencies. One would expect high transmission from mode 2 in region 1 to mode 1 in region 2 because the wavelengths of both modes are the same.

Some simple conclusions about the asymmetric step can be made from observation of the plots. First, at the cut-off frequency of the first mode, a constriction looks like a pressure release surface for the plane wave mode and rigid wall to the first mode. At that same frequency the expansion looks like a rigid wall to the plane wave mode. At the cutoff frequency of the first mode there major coupling from the plane wave mode

in region 1 and 2 to the first mode in region 1. At higher frequencies the first mode in region 1 couples well to the plane wave mode in regions 1 and 2. By comparing the magnitudes of the mutual reflection coefficients to the magnitudes of the self reflection coefficients, it is clear that modal coupling is significant and important.

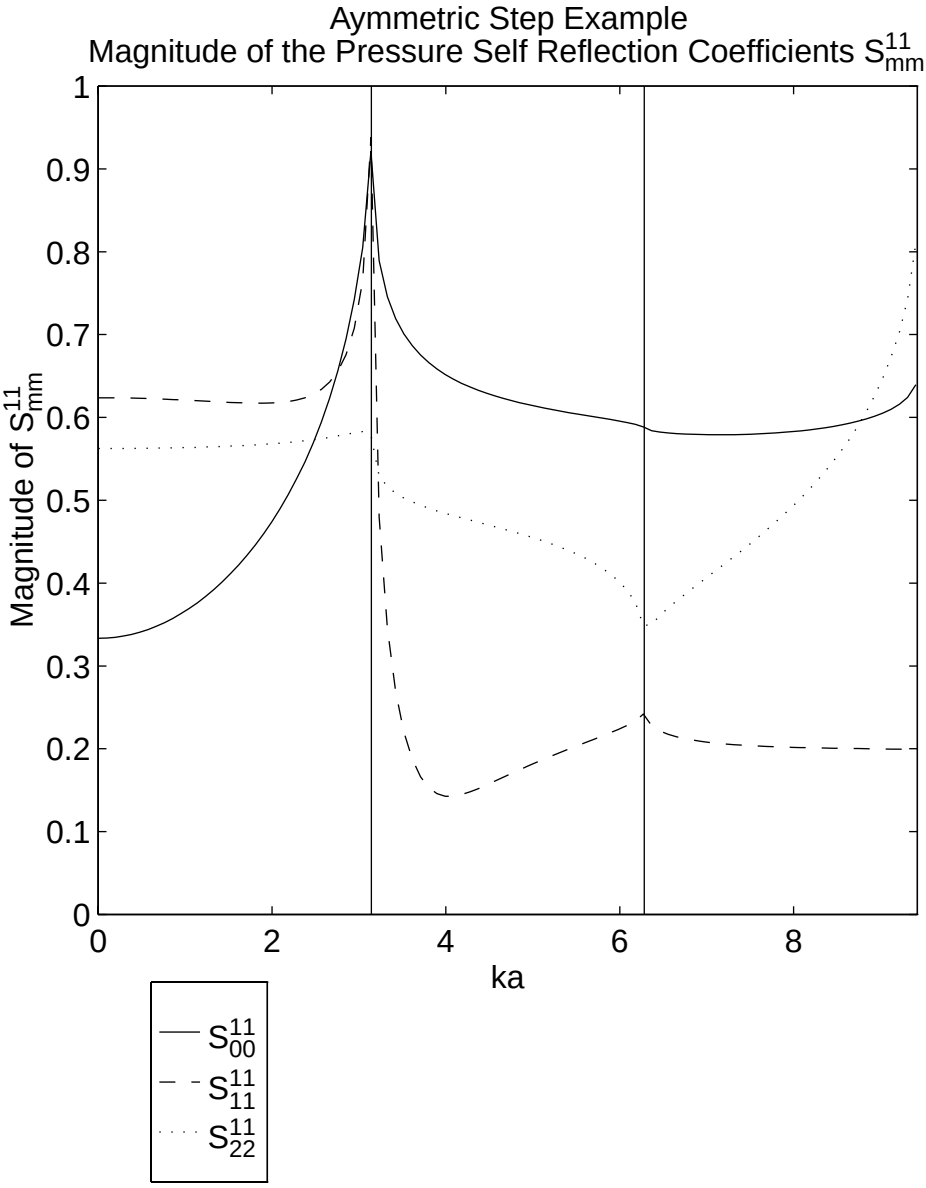

Fig. 3.4. Magnitude of the pressure self reflection coefficients in region 1, S^{11}_{mm}, for incident modes $m = 0, 1, 2$, with $a_1/a_2 = 2$ and $\epsilon = 0$.

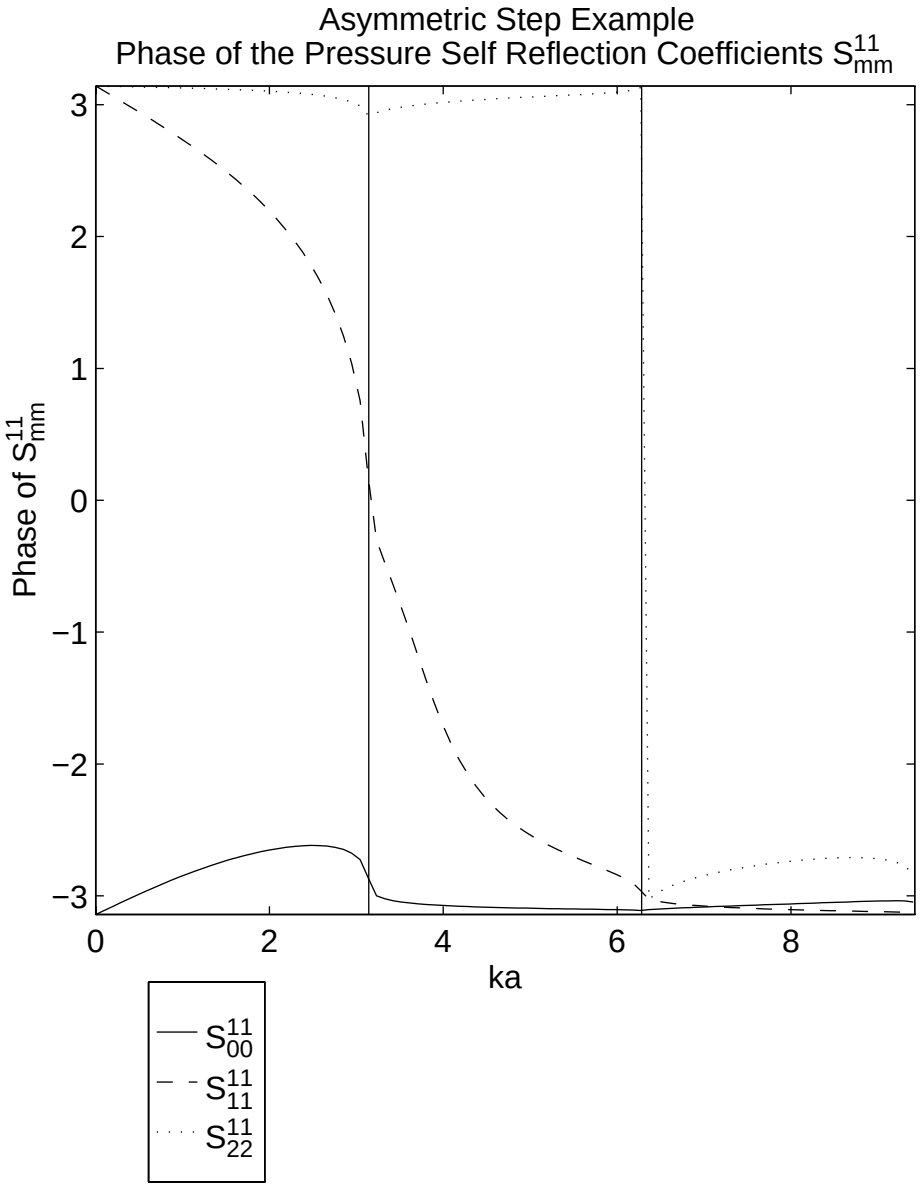

Fig. 3.5. Phase of the pressure self reflection coefficients in region 1, S^{11}_{mm}, for incident modes $m = 0, 1, 2$, with $a_1/a_2 = 2$ and $\epsilon = 0$.

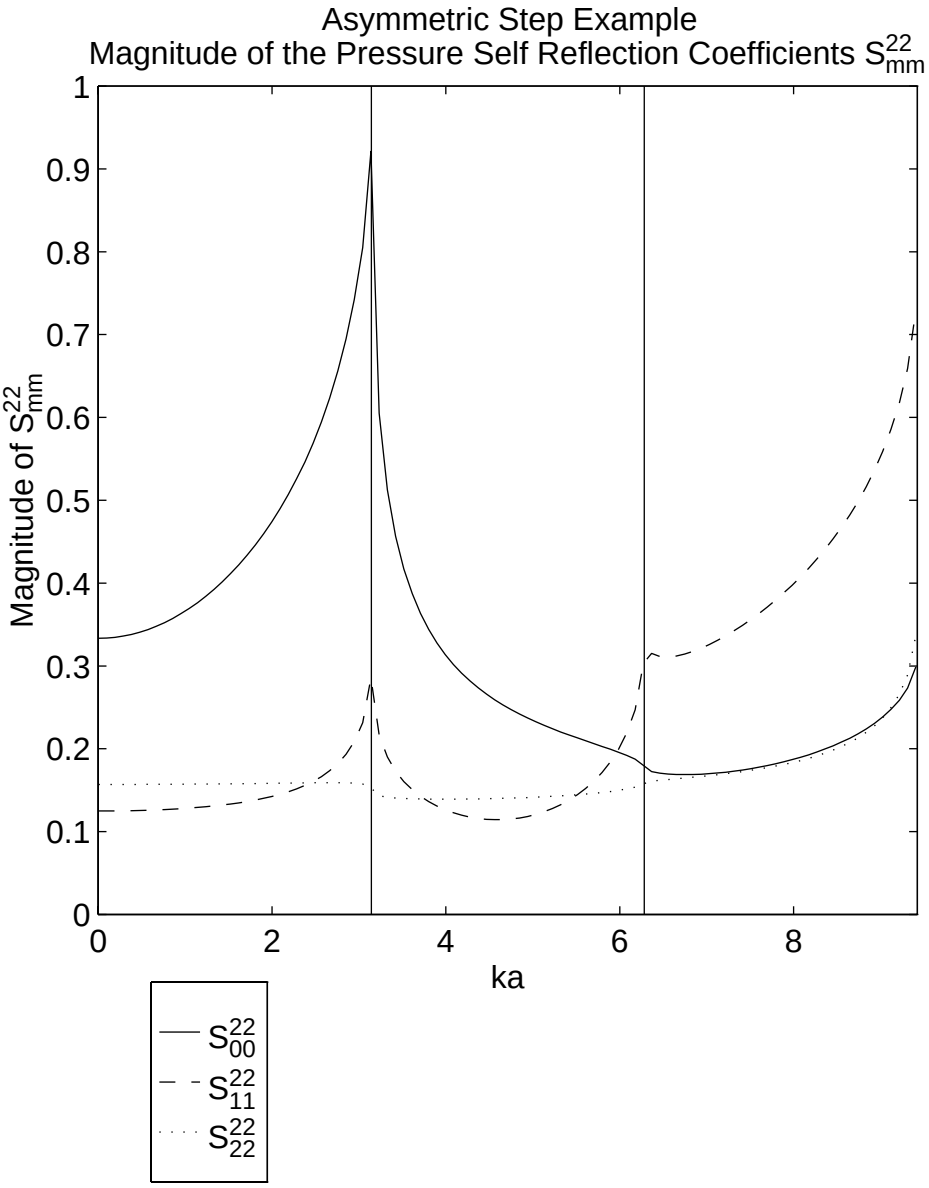

Fig. 3.6. Magnitude of the pressure self reflection coefficients in region 2, S^{22}_{mm}, for incident modes $m = 0, 1, 2$, with $a_1/a_2 = 2$ and $\epsilon = 0$.

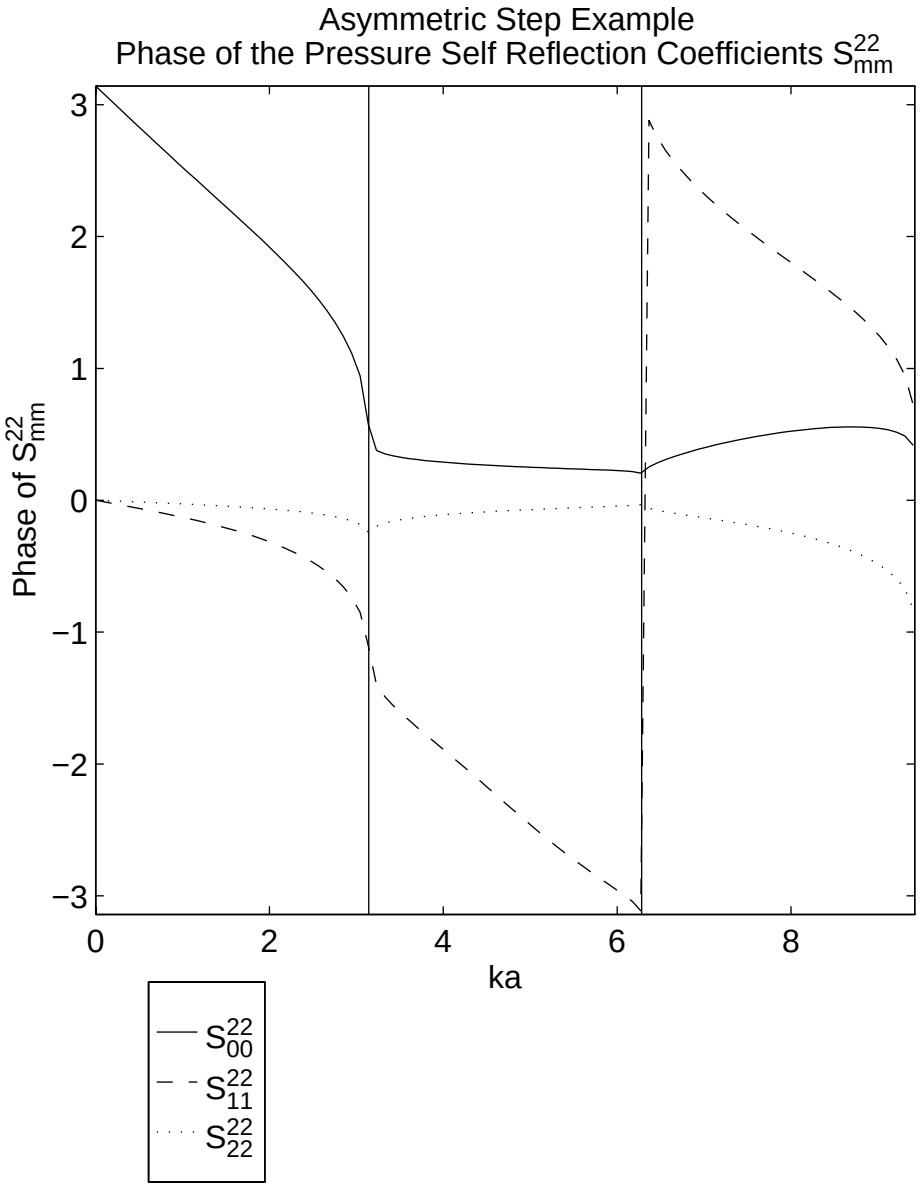

Fig. 3.7. Phase of the pressure self reflection coefficients in region 2, S^{22}_{mm}, for incident modes $m = 0, 1, 2$, with $a_1/a_2 = 2$ and $\epsilon = 0$.

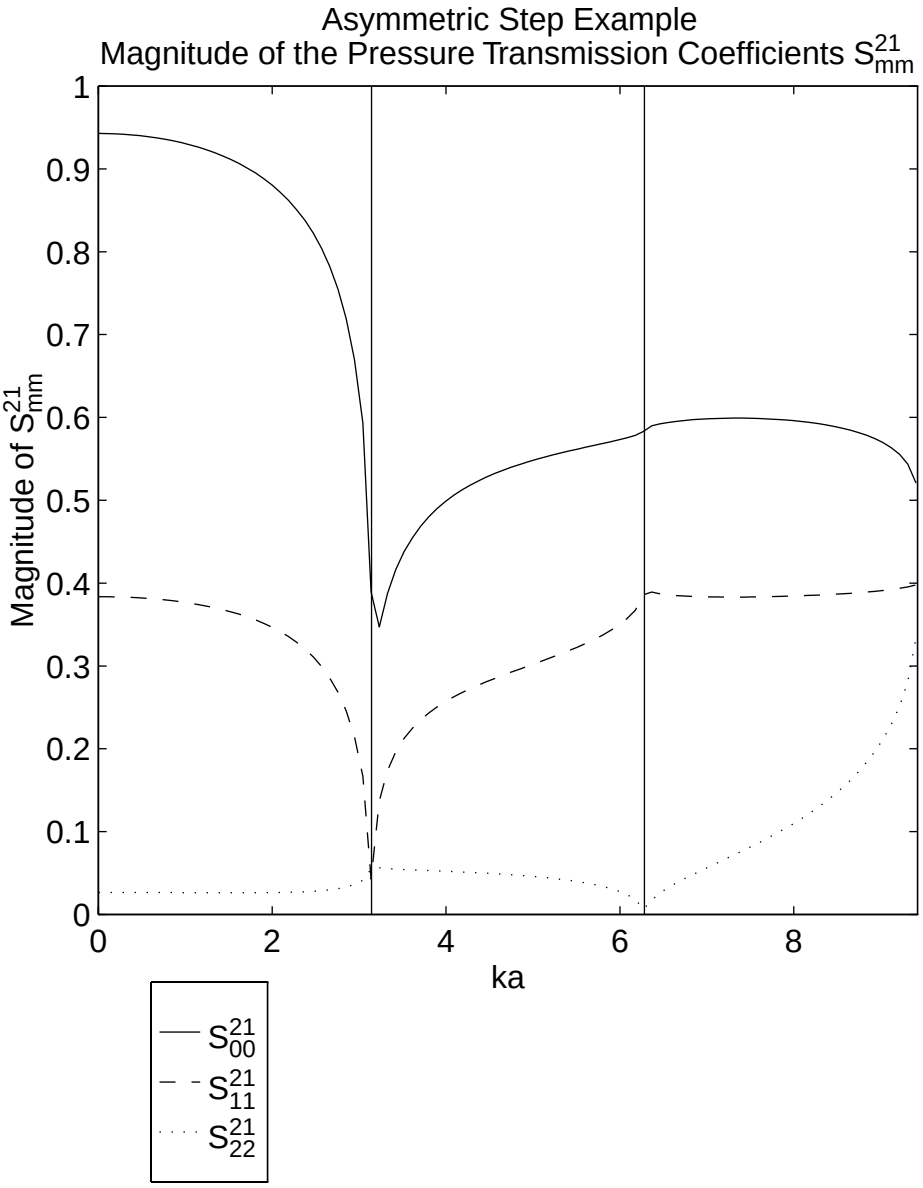

Fig. 3.8. Magnitude of the pressure self transmission coefficient of region 1 to region 2, S^{21}_{mm}, for incident modes $m = 0, 1, 2$, with $a_1/a_2 = 2$ and $\epsilon = 0$.

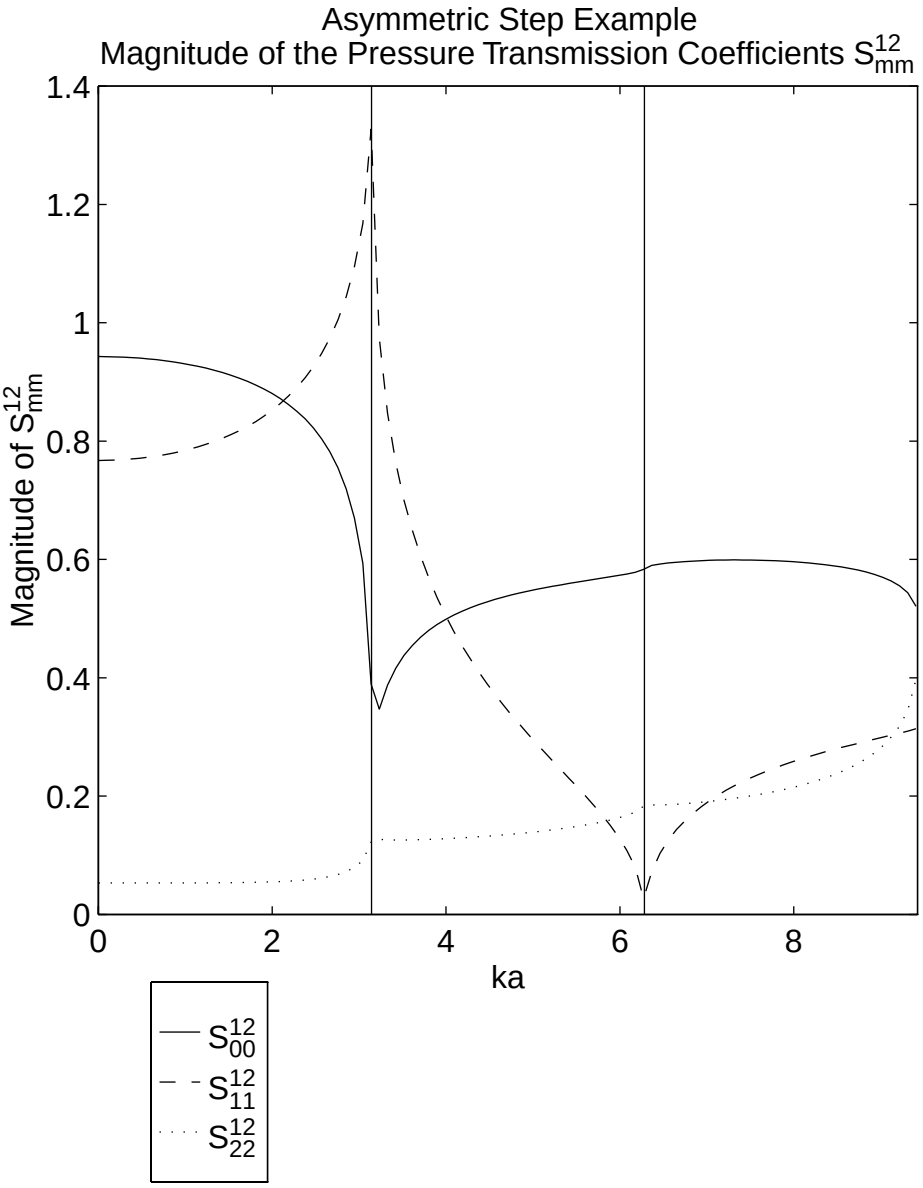

Fig. 3.9. Magnitude of the pressure self transmission coefficient of region 2 to region 1, S^{12}_{mm}, for incident modes $m = 0, 1, 2$, with $a_1/a_2 = 2$ and $\epsilon = 0$.

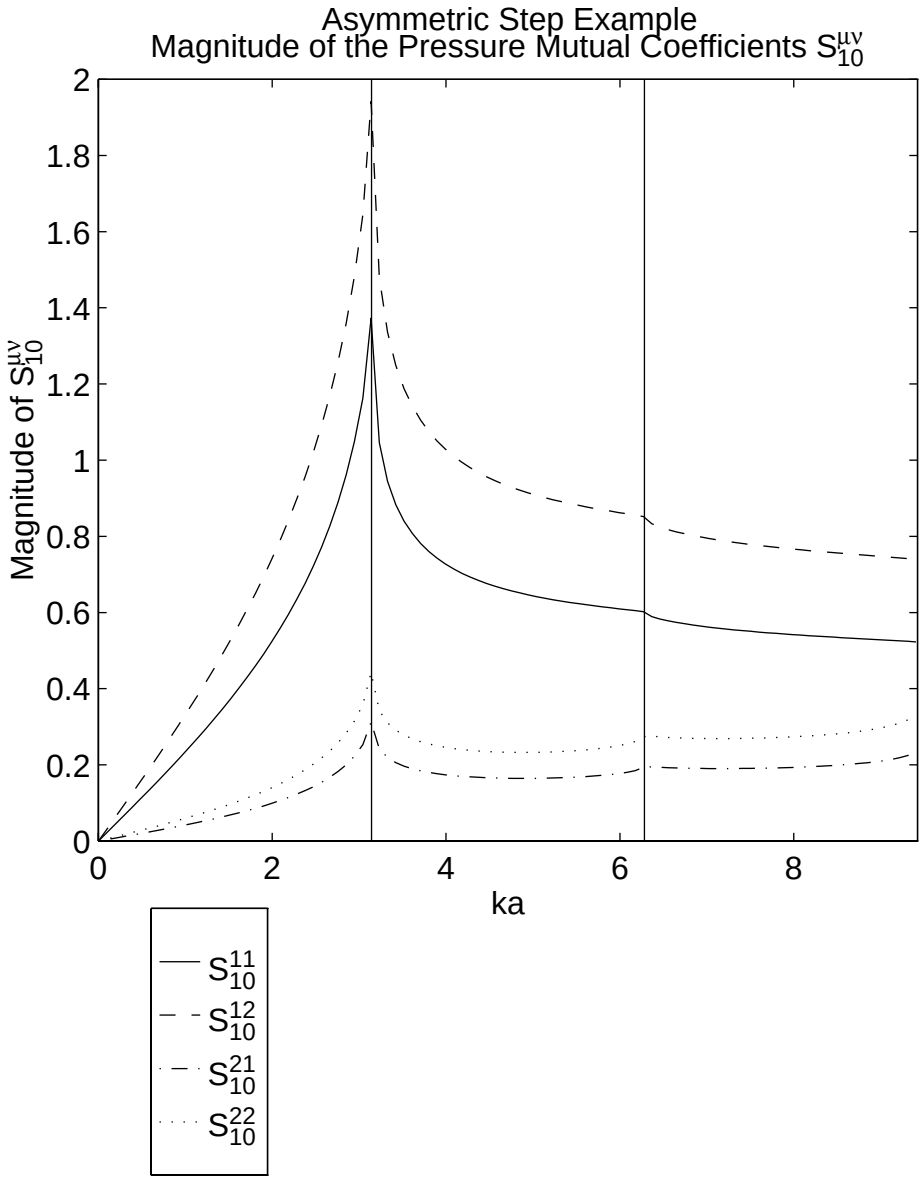

Fig. 3.10. Magnitude of the pressure mutual reflection and transmission coefficients for incident mode 0 in region ν to mode 1 in region μ, $S_{10}^{\mu\nu}$, with $a_1/a_2 = 2$ and $\epsilon = 0$.

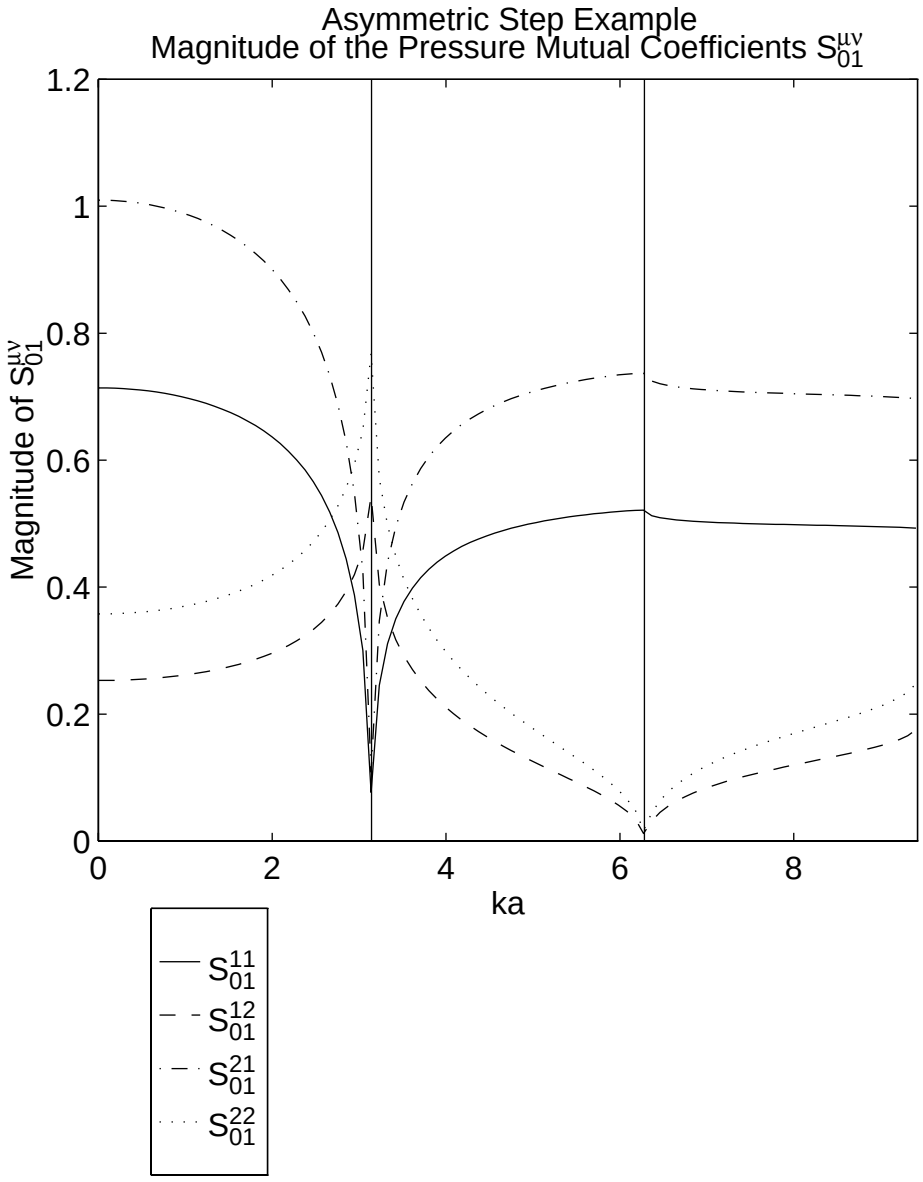

Fig. 3.11. Magnitude of the pressure mutual reflection and transmission coefficients for incident mode 1 in region ν to mode 0 in region μ, $S_{01}^{\mu\nu}$, with $a_1/a_2 = 2$ and $\epsilon = 0$.

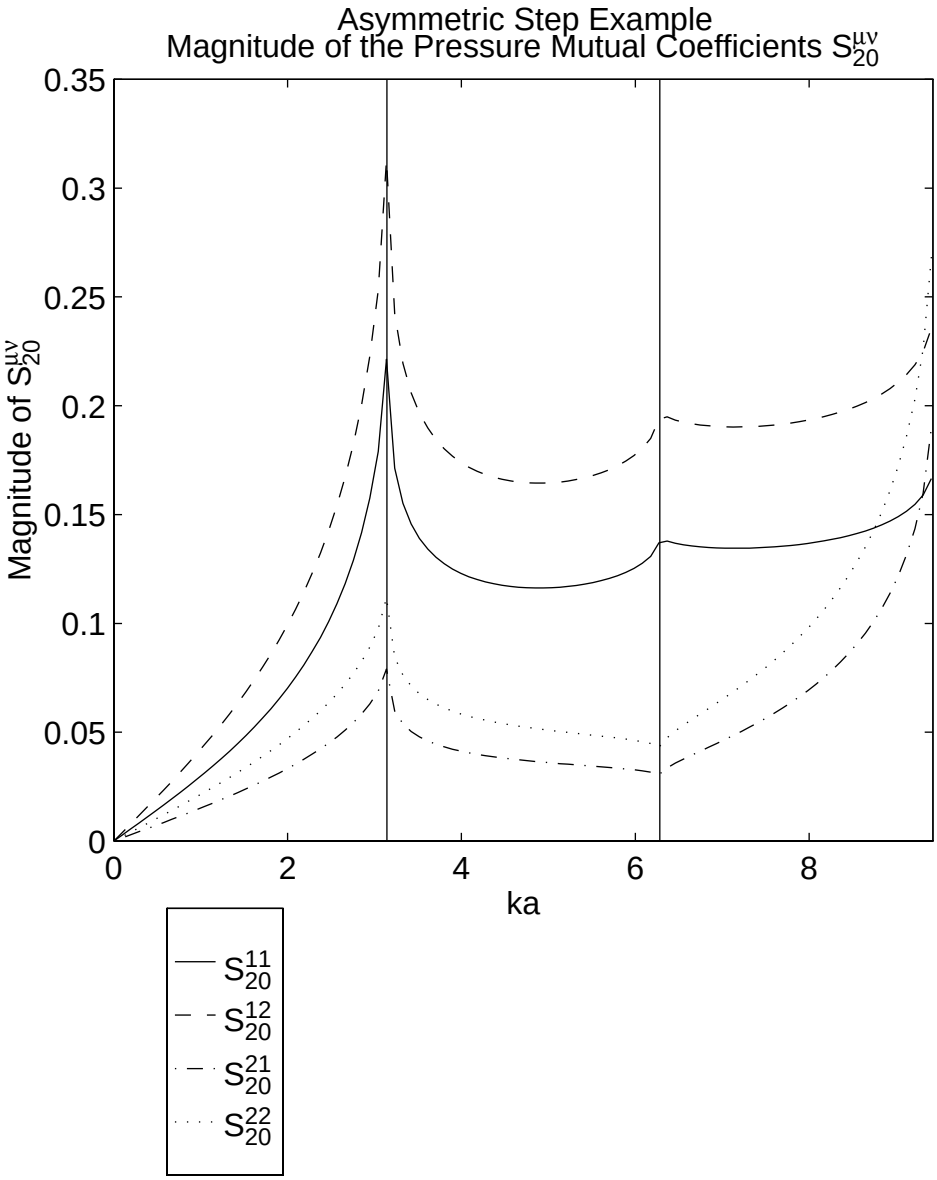

Fig. 3.12. Magnitude of the pressure mutual reflection and transmission coefficients for incident mode 0 in region ν to mode 2 in region μ, $S^{\mu\nu}_{20}$, with $a_1/a_2 = 2$ and $\epsilon = 0$.

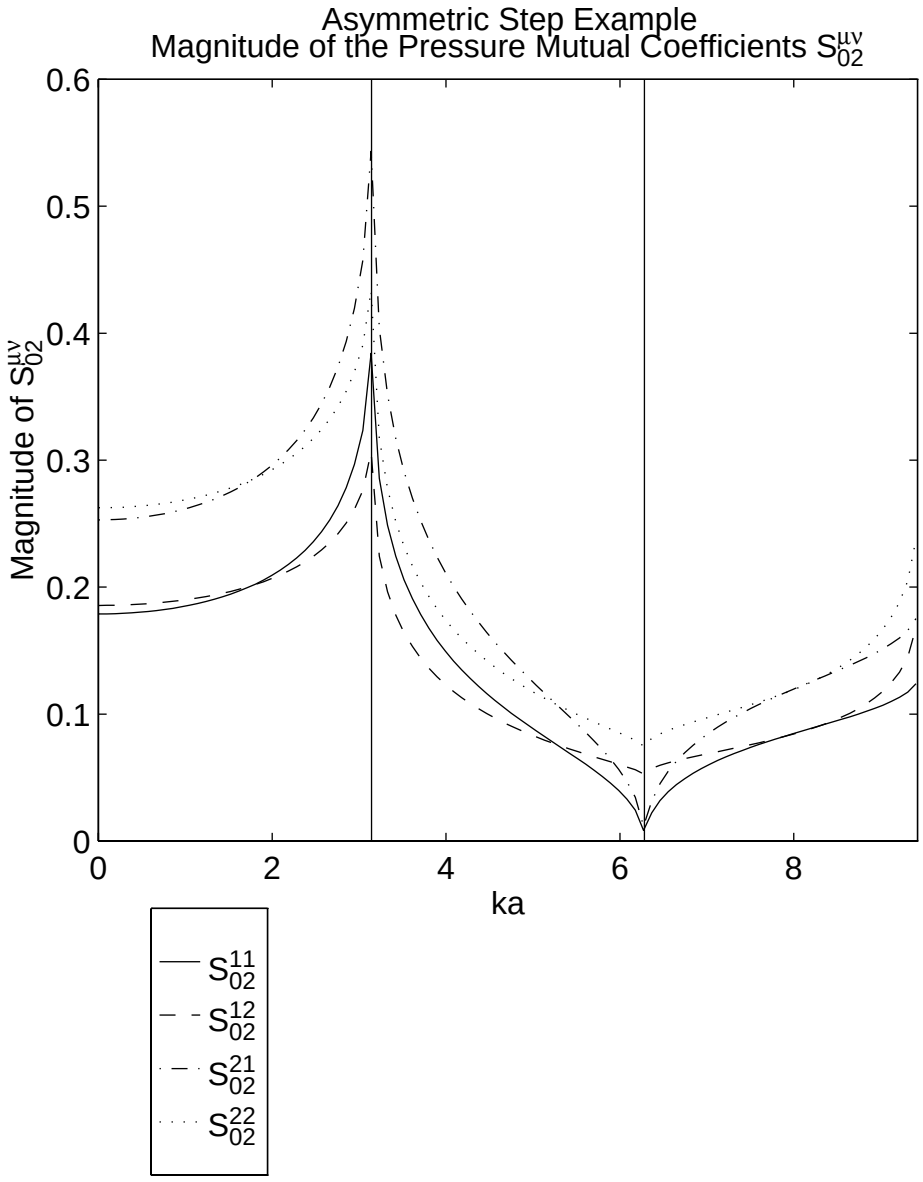

Fig. 3.13. Magnitude of the pressure mutual reflection and transmission coefficients for incident mode 2 in region ν to mode 0 in region μ, $S_{02}^{\mu\nu}$, with $a_1/a_2 = 2$ and $\epsilon = 0$.

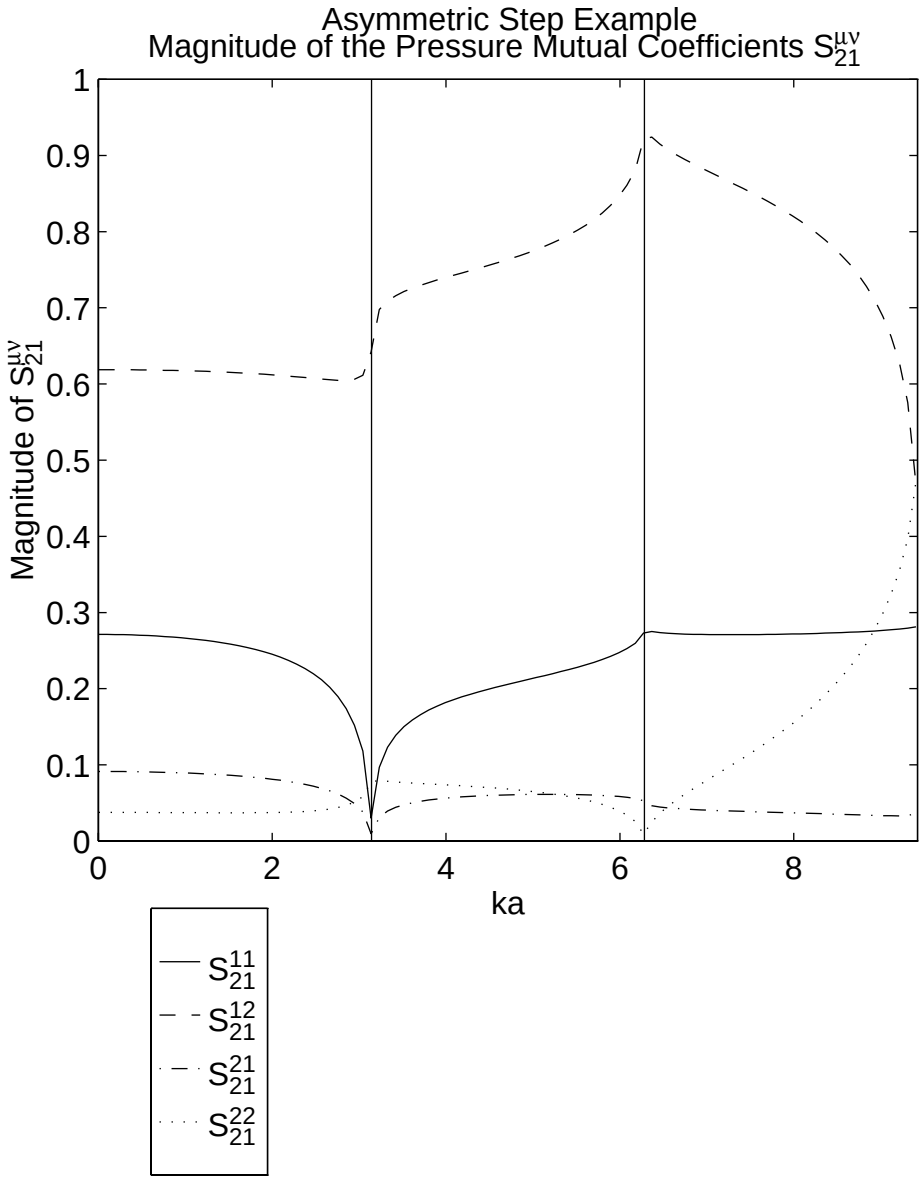

Fig. 3.14. Magnitude of the pressure mutual reflection and transmission coefficients for incident mode 1 in region ν to mode 2 in region μ, $S_{21}^{\mu\nu}$, with $a_1/a_2 = 2$ and $\epsilon = 0$.

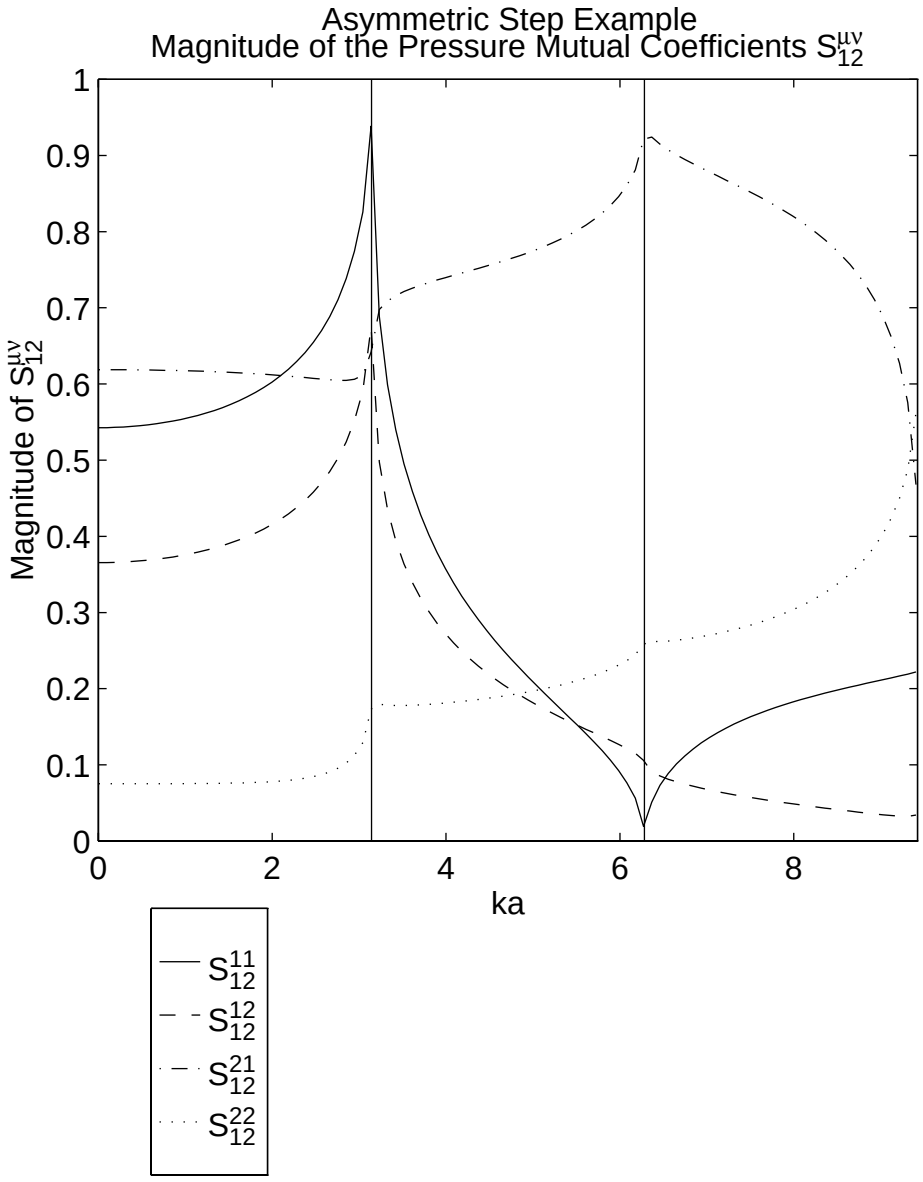

Fig. 3.15. Magnitude of the mutual pressure reflection and transmission coefficients for incident mode 2 in region ν to mode 1 in region μ, $S_{12}^{\mu\nu}$, with $a_1/a_2 = 2$ and $\epsilon = 0$.

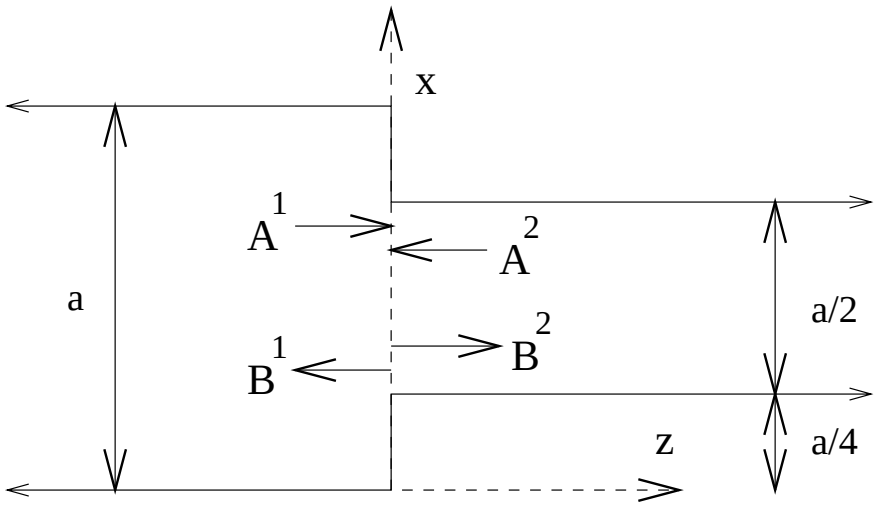

Fig. 3.16. Geometry of the Symmetric Stepped Duct in Example 3.4.2.

3.4.2 The Symmetric Stepped Duct

As a second example, consider a duct as shown in figure 3.16. This duct is symmetric as the discontinuity is about the center line of the duct. To simplify the calculation, only a discontinuity in the x direction is considered. Since there is no y discontinuity, all the y dependence and terms in the problem will drop out. Because of the symmetry of the problem, there is also no coupling between even and odd numbered modes.

Figure 3.17 shows the magnitude of the pressure self reflection coefficients of a symmetric constriction. The magnitude of the plane wave self reflection coefficient approaches the expected 1/3 at low frequencies. The plane wave coefficient increases with frequency, reaching unity at the cut-off frequency of the second horizontal mode. The magnitude of the self reflection coefficient of the first mode is unity for all frequencies

between the cut-off frequencies of the first mode and the second mode. The magnitude of self reflection coefficient of the second mode is unity at its cut-off frequency, but quickly drops above it.

Figure 3.18 shows the phase of the pressure self reflection coefficients of a symmetric constriction. The phase of plane wave coefficient is about π for all frequencies. Since the magnitude is unity at the cutoff frequency of the first mode, the constriction looks like a rigid wall to the plane wave mode, just like for the asymmetric duct. The phase of the first mode reflection coefficient is zero at its cut-off frequency so the constriction looks like a rigid wall at that frequency. The phase for the first mode coefficient is π at the cutoff of the second mode, so at that frequency the constriction looks like a pressure release surface. The phase of second mode coefficient is zero at the cut-off frequency of the second mode, so the constriction looks like a rigid wall to the second mode at the cut-off frequency.

Figure 3.19 shows the magnitude of the pressure self reflection coefficients of a symmetric expansion. The magnitude of the plane wave reflection coefficient approaches the expected 1/3 at low frequencies. The magnitude of plane wave coefficient increases with frequency, reaching unity at the cut-off frequency of the second horizontal mode. The magnitude of the first mode reflection coefficient approaches unity at the cut-off frequency of the first and second modes. The magnitude of reflection coefficient of the second mode is small for all frequencies.

Figure 3.20 shows the phase of the pressure self reflection coefficients of a symmetric expansion. The phase of plane wave coefficient starts at π and approaches zero at the cut-off frequency of the second mode. So the expansion looks like a rigid wall

at the cut-off frequency of the second mode. The phase of the first mode coefficient is zero at its cut-off frequency so the expansion looks like a rigid wall at that frequency. The phase for the first mode coefficient is π at the cutoff of the second mode, so at that frequency the expansion looks like a pressure release surface. The phase of second mode approaches $\pi/2$ at the cut-off frequency of the second mode.

Figure 3.22 shows the magnitude of the pressure self transmission coefficients from region 2 to region 1. The plane wave mode has high transmission until the cut-off frequency of the second mode. The first mode is well transmitted at its cut-off frequency but not at all at the cut-off frequency of the second mode. The second mode transmits well at its cut-off frequency, but the transmission drops at higher frequencies.

Figure 3.21 shows the magnitude of the pressure self transmission coefficients from region 1 to region 2. Again, the plane wave mode is well transmitted until the cut-off frequency of the second mode. The first mode is not transmitted at its cut-off frequency, but has very high transmission at the cut-off frequency of the second mode. Since the magnitude of first mode self reflection coefficient in region 1 was unity between the cut-off of the first and second modes, the change in the transmission coefficient is indicative of the change in phase of the reflection coefficient. At the cut-off frequency of the second mode the plane wave and second mode do not transmit well.

Figure 3.23 shows the mutual coupling coefficients from plane wave mode to the second mode. The plot shows that there is very significant coupling for reflected and transmitted second modes for a plane wave incident from region 1, but little coupling for a plane wave incident from region 2.

Figure 3.24 shows the mutual coupling coefficients from the second mode to the plane wave mode. The plot shows that at the cut-off frequency of the second mode there is significant coupling for reflected and transmitted modes for a mode incident from region 2. At higher frequencies there is significant coupling for modes incident in region 1.

Some simple conclusions about the symmetric step can be made from observation of the plots. First, at the cut-off frequency of the first mode, a constriction looks like a pressure release surface for the plane wave mode and rigid wall to the first mode and the second mode. At that same frequency the expansion looks like a rigid wall to the plane wave mode and a pressure release surface to the first mode. Again, there is significant modal coupling above the cut-off frequency of the first mode, with coupling coefficients greater than unity at some frequencies.

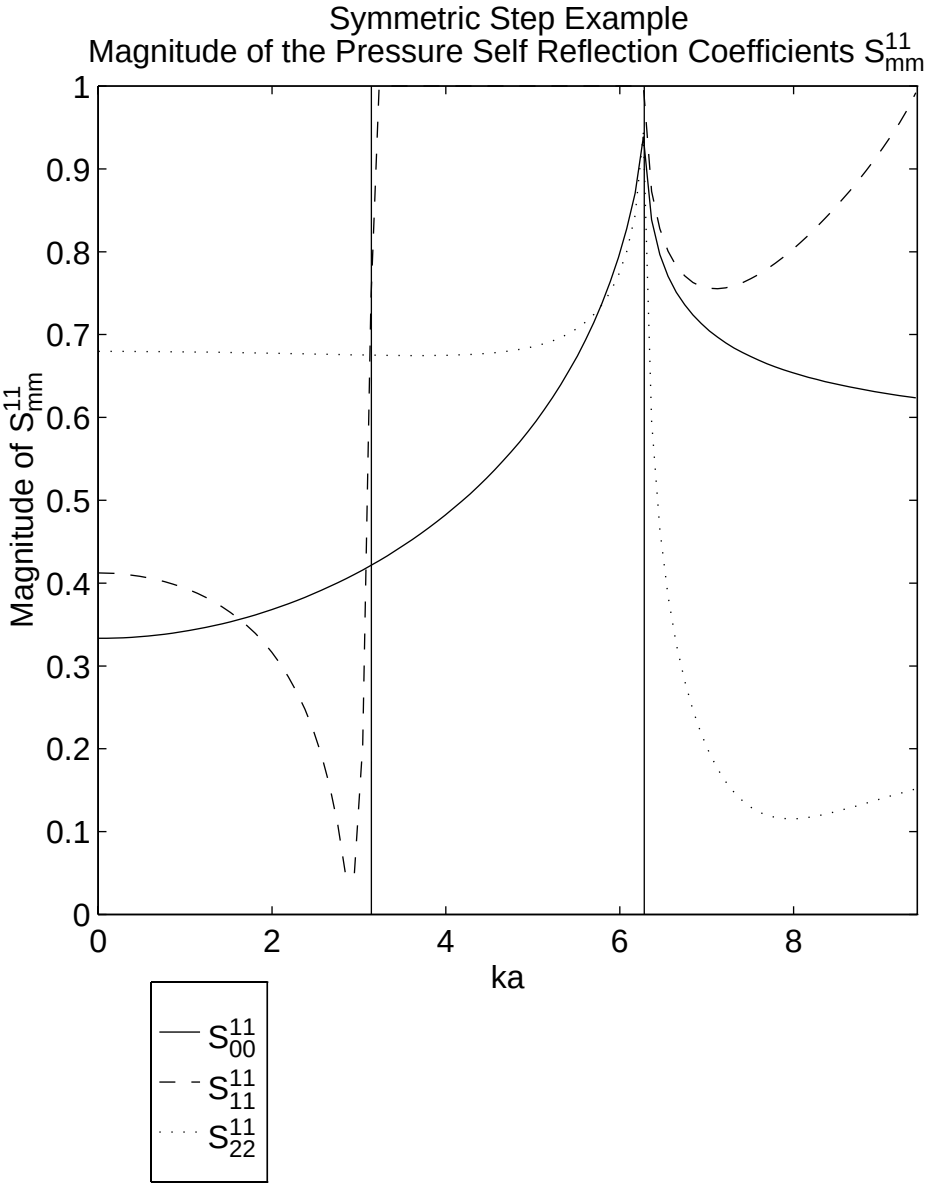

Fig. 3.17. Magnitude of the pressure self reflection coefficients in region 1, S^{11}_{mm}, for incident modes $m = 0, 1, 2$ with $a_1/a_2 = 2$ and $\epsilon = (a_1 - a_2)/4$.

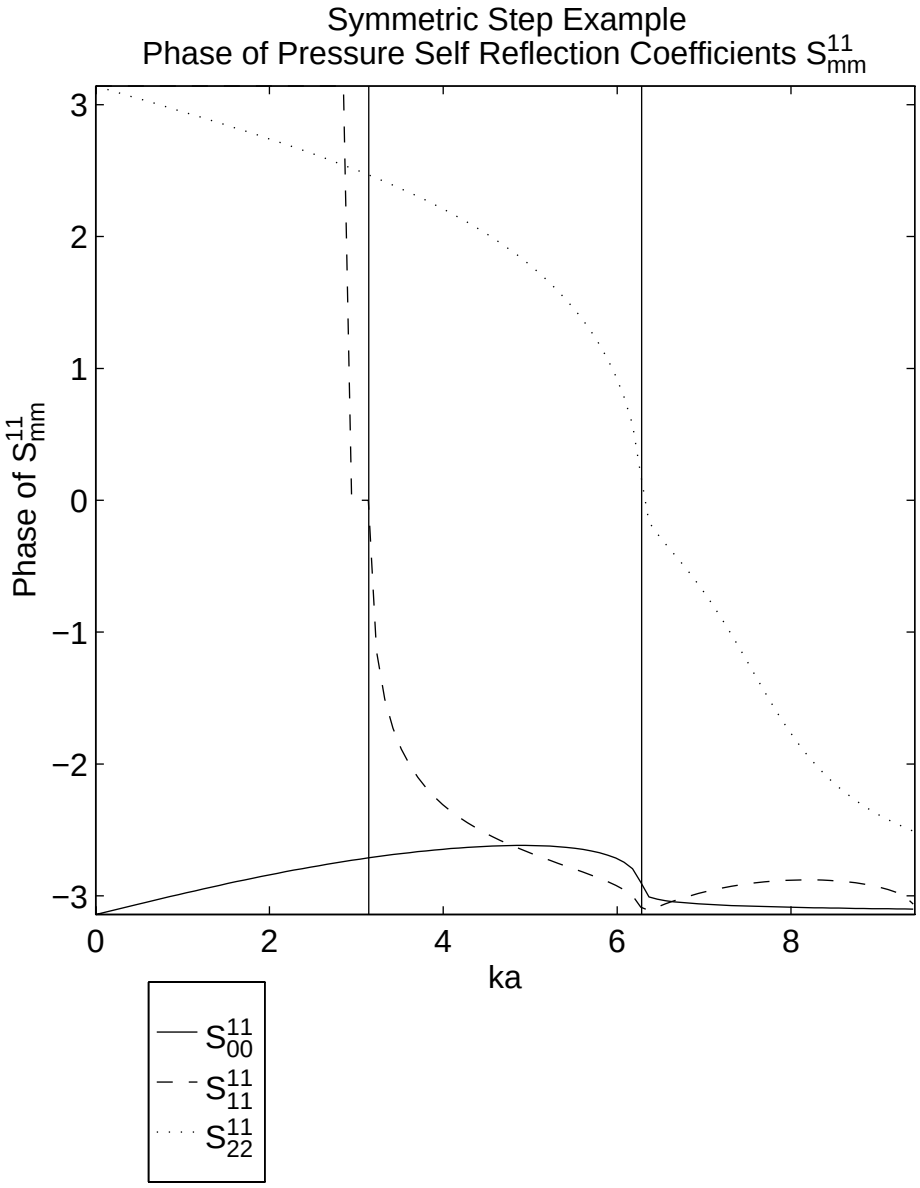

Fig. 3.18. Phase of the pressure self reflection coefficients in region 1, S^{11}_{mm}, for incident modes $m = 0, 1, 2$ with $a_1/a_2 = 2$ and $\epsilon = (a_1 - a_2)/4$.

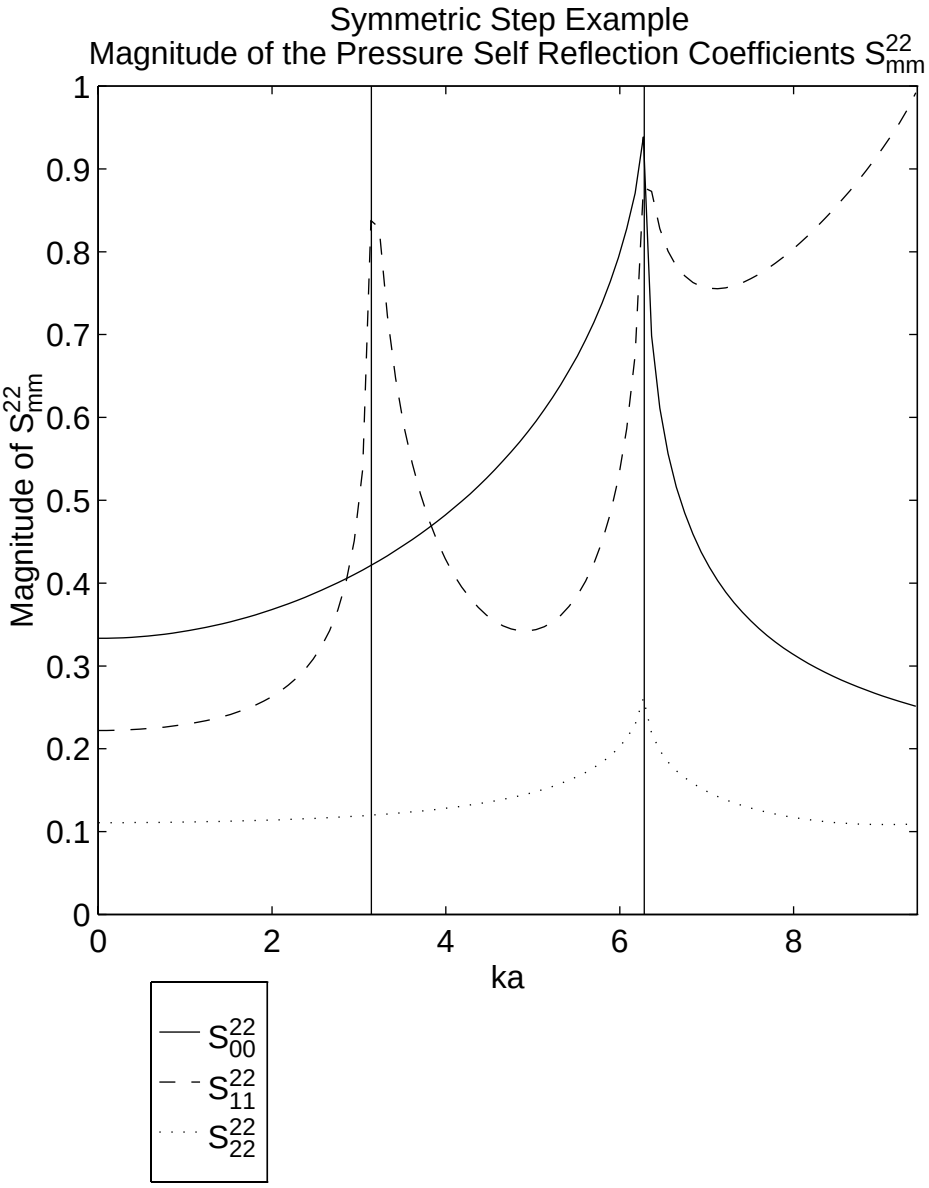

Fig. 3.19. Magnitude of the pressure self reflection coefficients in region 2, S^{22}_{mm}, for incident modes $m = 0, 1, 2$ with $a_1/a_2 = 2$ and $\epsilon = (a_1 - a_2)/4$.

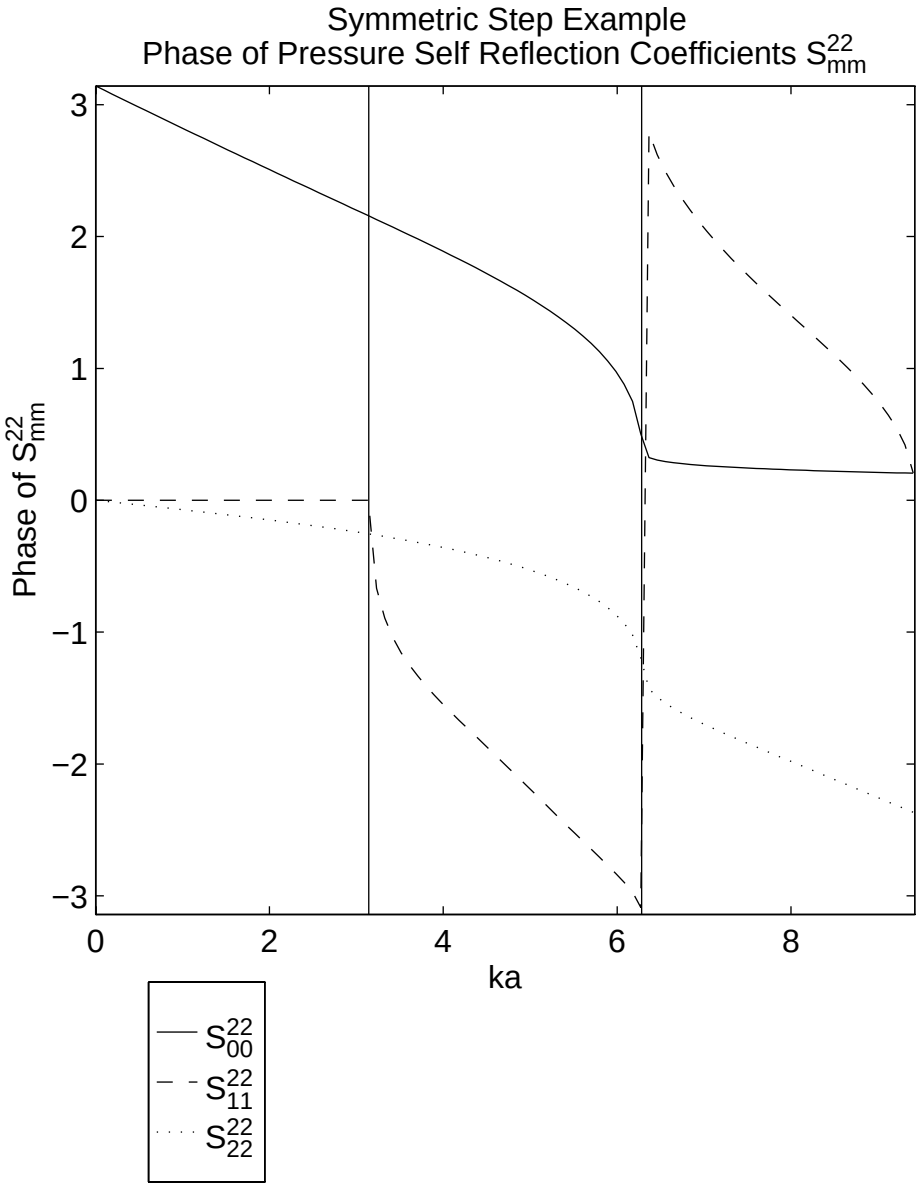

Fig. 3.20. Phase of the pressure self reflection coefficients in region 2, S^{22}_{mm}, for incident modes $m = 0, 1, 2$ with $a_1/a_2 = 2$ and $\epsilon = (a_1 - a_2)/4$.

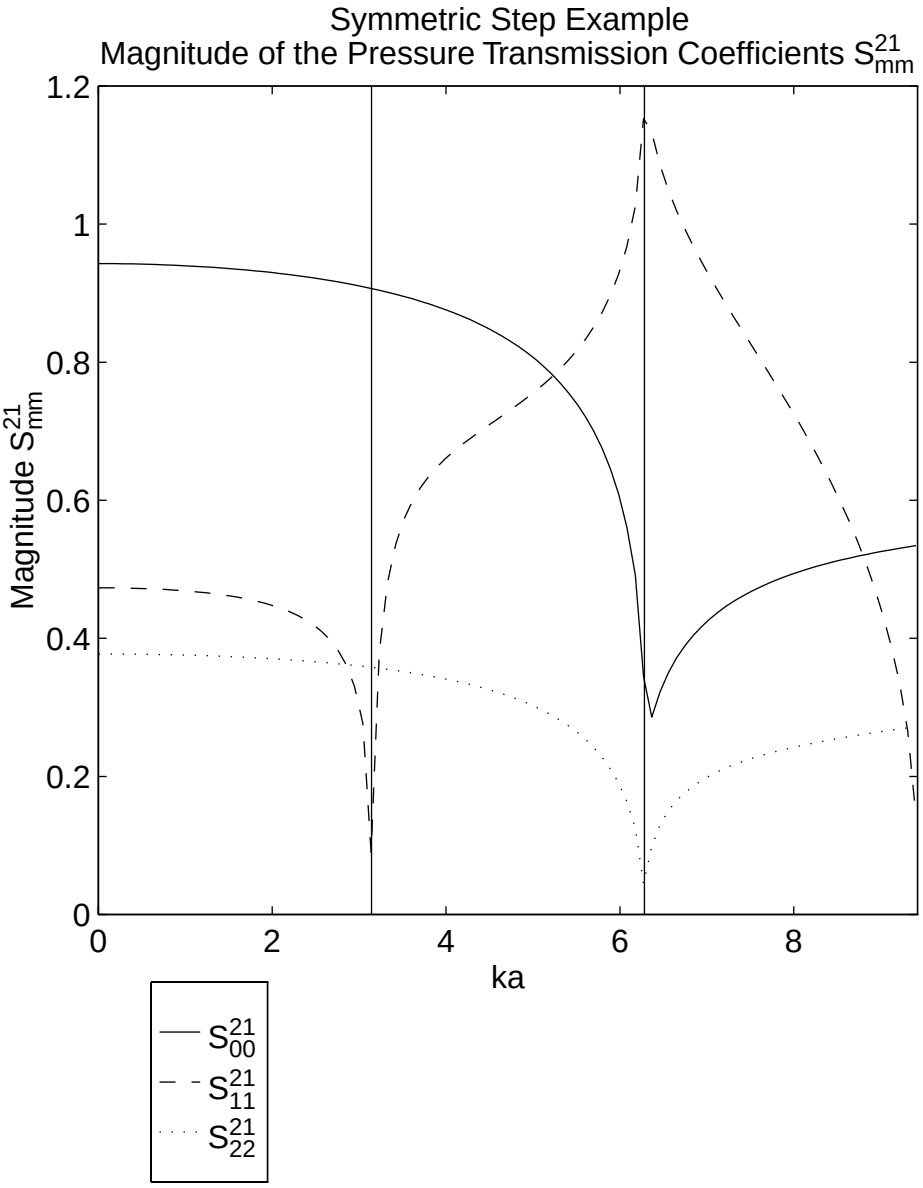

Fig. 3.21. Magnitude of the pressure self transmission coefficient of region 1 to region 2, S^{21}_{mm}, for incident modes $m = 0, 1, 2$, with $a_1/a_2 = 2$ and $\epsilon = (a_1 - a_2)/4$.

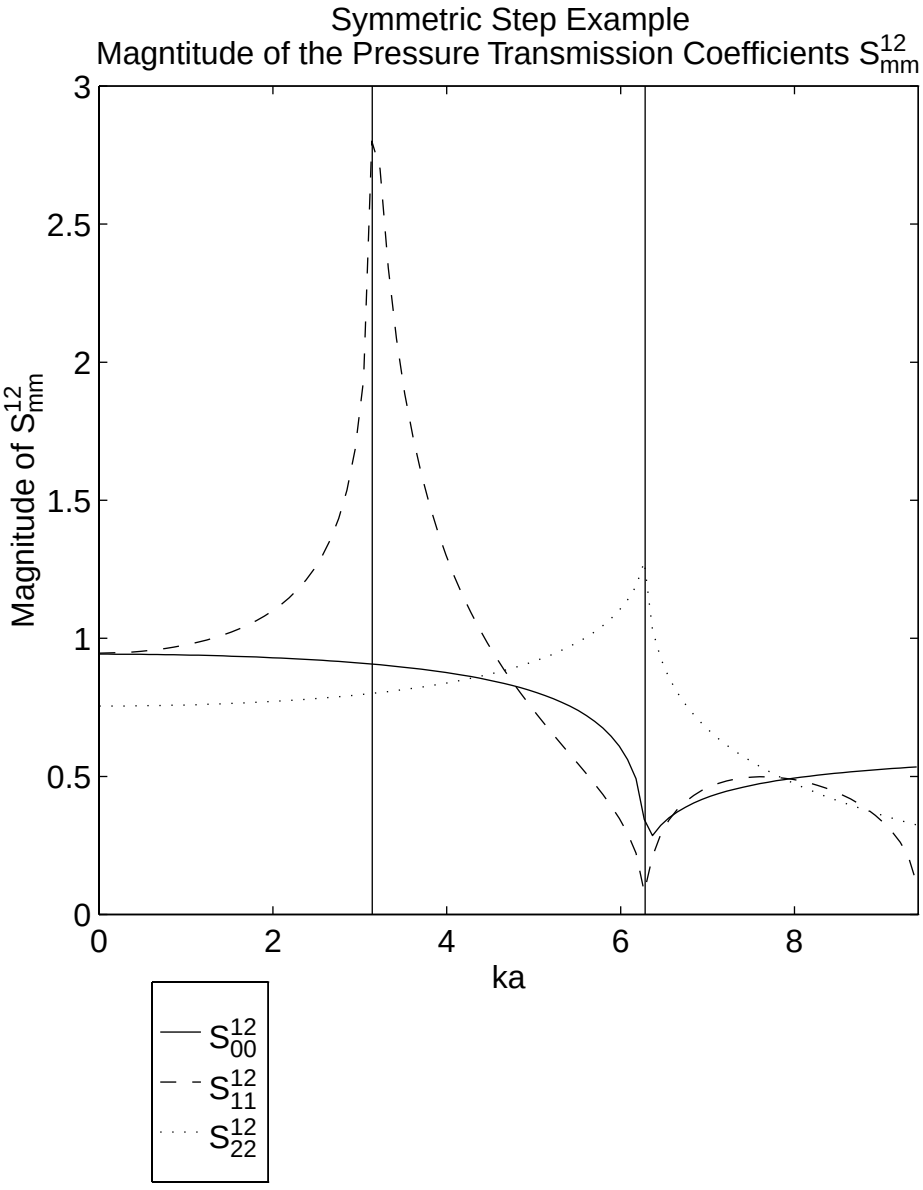

Fig. 3.22. Magnitude of the pressure self transmission coefficient of region 2 to region 1, S^{12}_{mm}, for incident modes $m = 0, 1, 2$, with $a_1/a_2 = 2$ and $\epsilon = (a_1 - a_2)/4$.

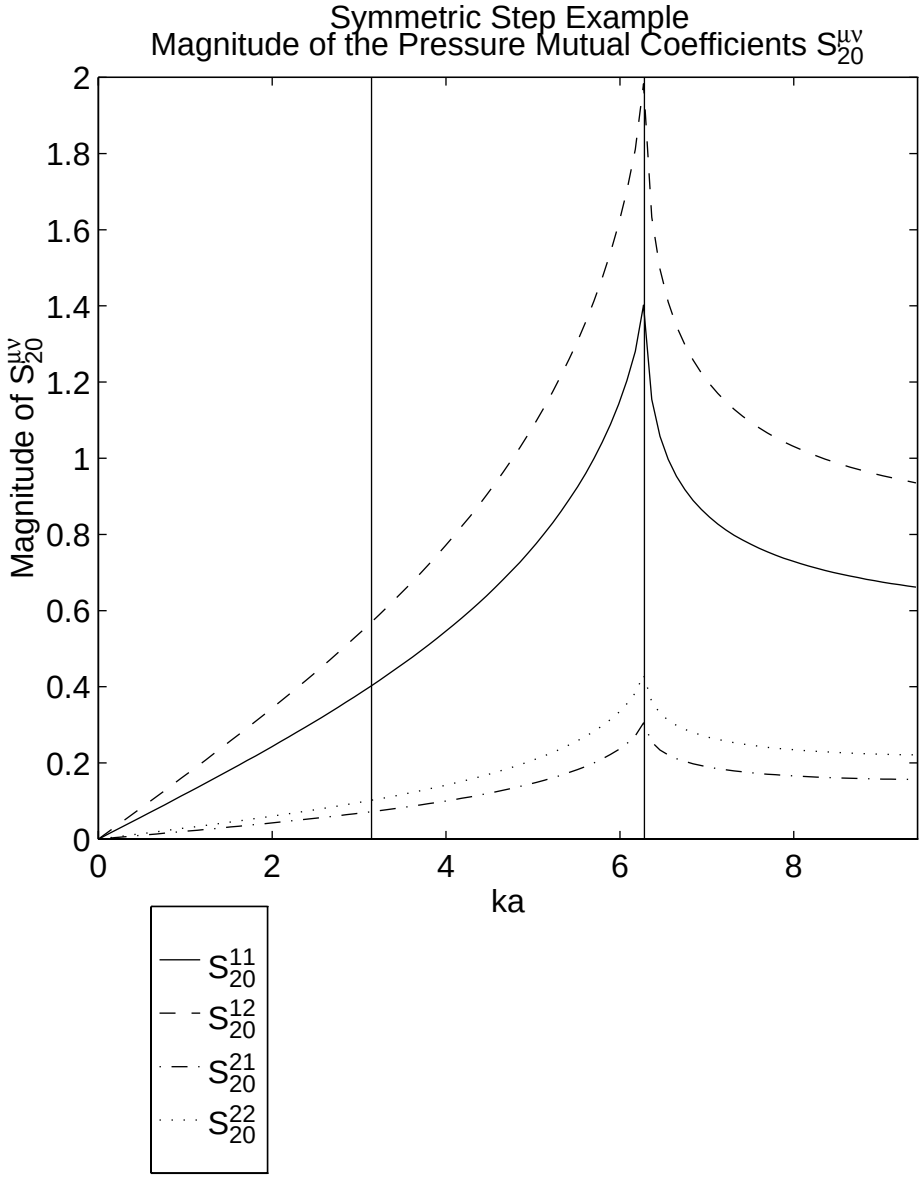

Fig. 3.23. Magnitude of the pressure mutual reflection and transmission coefficients for incident mode 0 in region ν to mode 2 in region μ, $S_{20}^{\mu\nu}$, with $a_1/a_2 = 2$ and $\epsilon = (a_1 - a_2)/4$.

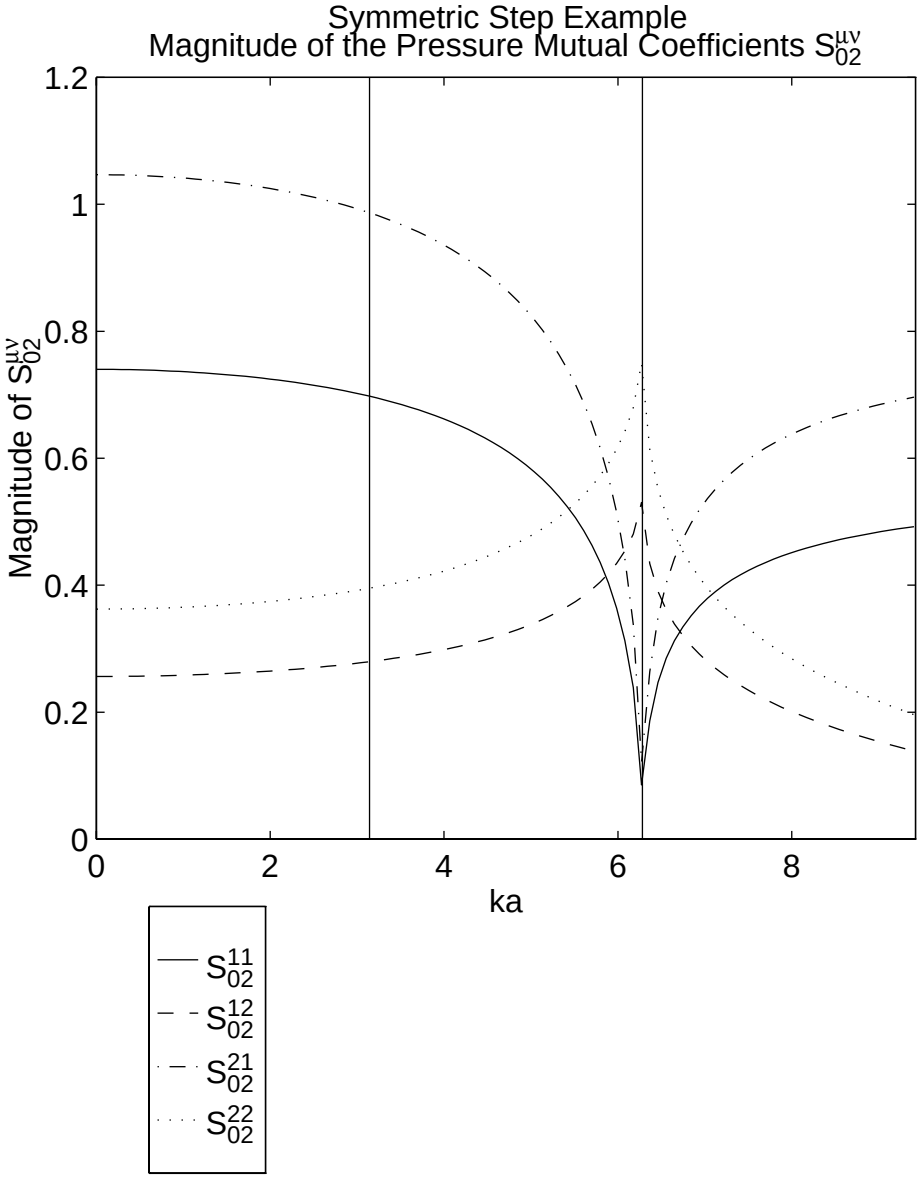

Fig. 3.24. Magnitude of the pressure mutual reflection and transmission coefficients for incident mode 2 in region ν to mode 0 in region μ, $S_{02}^{\mu\nu}$, with $a_1/a_2 = 2$ and $\epsilon = (a_1 - a_2)/4$.

Chapter 4

Modal Scattering at Junctions

Just as the step discontinuity was an important part of acoustical networks and filters, so is the junction. A junction is a general region to which two or more ducts are connected. A duct bend can be described as a sort of junction with two ports. Expansion and constriction chambers could also be described as junctions with two ports. This chapter will derive a basic theory for determining reflection and transmission between the different ports of a junction.

4.1 General Junction Theory

Consider a multi-port junction as shown in figure 4.1. Each port is a duct, each with its own propagating modes. When a given mode in one duct is incident upon the junction, part of the mode is reflected back into that same mode in that duct, part is reflected back into other modes in that duct, and part is transmitted into various modes in other ducts.

If the Green's function for the junction region is known, an integral relation between the pressure and the velocity at the duct-junction interface can be developed. The pressure and velocity can be written in terms of the modes and hence an integral relation between the modes can be established.

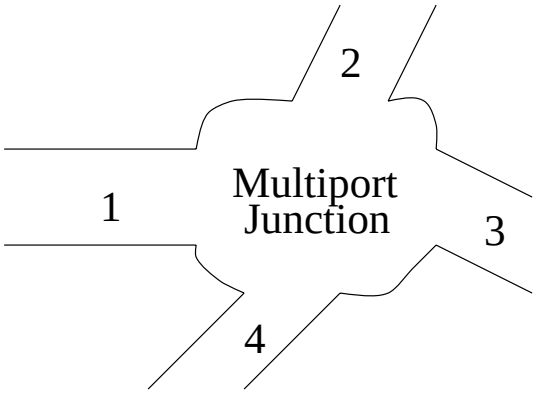

Fig. 4.1. Geometry of a Multi-port Junction

In particular, consider an N port junction in which a Green's function G_J for the junction region is known. In addition assume that on the surface of the interior $\partial G_J/\partial n = 0$. The pressure at some position $\vec{x}$ inside or on the interior surface of the junction is given by

$$p(\vec{x}) = jk\rho c \iint_{\mathcal{S}_0} G_J(\vec{x}|\vec{x_0})\vec{u}(\vec{x_0}) \cdot \vec{n} d\mathcal{S}_0 \tag{4.1}$$

where $\vec{n}$ is the surface normal and $\mathcal{S}_0$ is the interior surface of the junction.

If the walls of the junction are rigid the velocity at the junction surface is only nonzero at the other ports and the pressure at the lth duct/junction interface is given by

$$p^l(\vec{x}_l) = jk\rho c \sum_i \iint_{\mathcal{S}_i} G_J(\vec{x}_l|\vec{x}_i)\vec{u}(\vec{x}_i) \cdot \vec{n} d\mathcal{S}_i \tag{4.2}$$

where $\mathcal{S}_i$ is the area of the ith duct.

The pressure in each duct can be expanded into a modal series of the form

$$p^l(x_l, y_l, v_l) = \sum_M (A^l_M e^{-\gamma^l_M z_l} + B^l_M e^{\gamma^l_M z_l}) \psi^l_M(x_l, y_l) \tag{4.3}$$

where x_l, y_l, and z_l are locally defined coordinates such that the interface between the duct and junction is defined as $z_l = 0$ and the direction of $+z_l$ is towards the junction.

Given p^l as above, the normal velocity u^l_z can be found, using Euler's equation, to be

$$u^l_z = \sum_M Y^l_M (A^l_M e^{-\gamma^l_M z_l} - B^l_M e^{\gamma^l_M z_l}) \psi^l_M(x_l, y_l) \tag{4.4}$$

where Y^l_M is the characteristic modal admittance of the Mth mode in the lth port.

Using equations 4.3 and 4.4 in equation 4.2 results in the relation

$$\begin{aligned} \sum_M (A^l_M + B^l_M) \psi^l_M(x_l, y_l) &= jk\rho c \sum_i \sum_M Y^i_M (A^i_M - B^i_M) \\ &\quad \times \iint_{\mathcal{S}_i} G_J(x_l, y_l | x_i, y_i) \Big|_{\substack{z_l=0 \\ z_i=0}} \psi^i_M(x_i, y_i) dx_i dy_i. \end{aligned} \tag{4.5}$$

Multiplying equation 4.5 by ψ^l_R and integrating over S_l yields

$$A^l_R + B^l_R = \sum_i \sum_M Y^i_M (A^i_M - B^i_M) Z^{li}_{RM} \tag{4.6}$$

where

$$Z^{li}_{RM} = jk\rho c \iint_{\mathcal{S}_l} \iint_{\mathcal{S}_i} G_J(x_l, y_l | x_i, y_i) \Big|_{\substack{z_l=0 \\ z_i=0}}$$

$$\times\psi_R^l(x_l, y_l)\psi_M^i(x_i, y_i)dx_i dy_i dx_l dy_l. \tag{4.7}$$

Z_{RM}^{li} is the mutual modal impedance between port i mode M and port l mode R.

Since impedance is the ratio of pressure to velocity, the reason for identifying Z_{RM}^{li} as a modal impedance is because the left hand side of equation 4.6 is the amplitude of the pressure of the Rth mode in the lth port while the right hand size is the sum of Z_{RM}^{li} times the velocity of the Mth mode in the ith port.

Equation 4.6 has Y_M^i multiplying Z_{RM}^{li}. Since Y_M^i is the characteristic modal admittance of the Mth mode in port i, the multiplication is normalization of the mutual modal impedance by the characteristic modal impedance of that port. Thus, it makes sense to define the normalized modal impedance η_{RM}^{li} as

$$\eta_{RM}^{li} = Y_M^i Z_{RM}^{li}. \tag{4.8}$$

In matrix form equation 4.6 becomes

$$\bar{A}^l + \bar{B}^l = \bar{\eta}^{li}(\bar{A}^i - \bar{B}^i). \tag{4.9}$$

The reflected waves $\bar{B}^l$ can be rewritten in terms of the incident waves and scattering parameters in the form

$$\bar{B}^l = \sum_q \bar{S}^{lq}\bar{A}^q \tag{4.10}$$

and equation 4.9 becomes

$$\bar{A}^l + \sum_q \bar{S}^{lq}\bar{A}^q = \bar{\eta}^{li}(\bar{A}^i - \sum_q \bar{S}^{iq}\bar{A}^q). \tag{4.11}$$

Defining the super matrices

$$\bar{A} = \begin{bmatrix} \bar{A}^0 \\ \bar{A}^1 \\ \vdots \end{bmatrix} \quad \bar{Y} = \begin{bmatrix} \bar{Y}^0 \\ \bar{Y}^1 \\ \vdots \end{bmatrix} \quad \bar{S} = \begin{bmatrix} \bar{S}^{00} & \bar{S}^{01} & \dots \\ \bar{S}^{10} & \bar{S}^{11} & \dots \\ \vdots & \vdots & \ddots \end{bmatrix} \quad \bar{\eta} = \begin{bmatrix} \bar{\eta}^{00} & \bar{\eta}^{01} & \dots \\ \bar{\eta}^{10} & \bar{\eta}^{11} & \dots \\ \vdots & \vdots & \ddots \end{bmatrix} \tag{4.12}$$

equation 4.11 can be reduced to

$$(\bar{I} + \bar{S})\bar{A} = \bar{\eta}(\bar{I} - \bar{S})\bar{A} \tag{4.13}$$

from which the scattering matrix $\bar{S}$ is found to be

$$\bar{S} = (\bar{\eta} + \bar{I})^{-1}(\bar{\eta} - \bar{I}). \tag{4.14}$$

This form of the equation for the scattering matrix is the same as the normalized form of the plane wave reflection coefficient at a planar change of impedance.

4.2 Examples

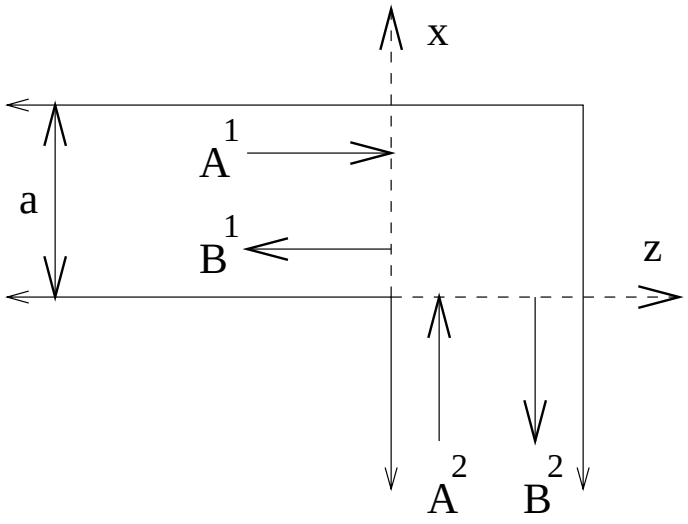

Fig. 4.2. Geometry of a Right Angle Duct Bend

4.2.1 A Right Angle Bend

Consider a right angle (90^o) bend in a duct as show in figure 4.2. For this problem there is no discontinuity in the y direction, hence there will be no scattering in the y direction. Then there is no y dependence in the problem and the y components and summations can be eliminated from the problem. Also, since most of the summations have been reduced to single summations, standard summation notation will be used.

This problem is essentially a two port junction, with the junction being a square of side a. The Green's function for the junction is

$$G_J(x,z|x_0,z_0) = \sum_{n_x}\sum_{n_z} \frac{\cos(\frac{n_x\pi}{a}x)\cos(\frac{n_z\pi}{a}z)\cos(\frac{n_x\pi}{a}x_0)\cos(\frac{n_z\pi}{a}z_0)}{a^2\Lambda_{n_x}\Lambda_{n_y}[(\frac{n_x\pi}{a}^2)+(\frac{n_z\pi}{a}^2)-k^2]}. \tag{4.15}$$

Since the junction is only two ports, it is probably easier to understand the problem by discussing the reflection and transmission coefficients rather than the scattering coefficients. The scattering parameters from a port to itself will be called the reflection coefficient R and the scattering parameter from a port to the other port will be called the transmission coefficient T.

The locally defined coordinates are

$$x_1 = x, \quad z_1 = z, \quad x_2 = z, \quad z_2 = x. \tag{4.16}$$

To apply equation 4.14, $\bar{\eta}$ must be computed, which means Z^{il}_{RM} must be computed. By symmetry $Z^{12} = Z^{21}$ and $Z^{11} = Z^{22}$ so only two terms need actually be computed. Using equation 4.15, the equation for Z^{11}_{rm} becomes

$$\begin{aligned} Z^{11}_{rm} &= jk\rho c \int_{x=0}^{a} \int_{x_0=0}^{a} \sum_{n_x} \sum_{n_z} \frac{\cos(\frac{n_x\pi}{a}x)\cos(\frac{n_x\pi}{a}x_0)\cos(\frac{m\pi}{a}x)\cos(\frac{r\pi}{a}x_0)}{a^3\Lambda_{n_x}\Lambda_{n_z}\sqrt{\Lambda_m\Lambda_r}[(\frac{n_x\pi}{a})^2+(\frac{n_z\pi}{a})^2-k^2]} \\ &= jk\rho c\ \delta_{mr} \sum_{n_z} \frac{1}{a\Lambda_{n_z}[(\frac{m\pi}{a})^2+(\frac{n_z\pi}{a})^2-k^2]} \\ &= -\frac{jk\rho c}{k_m}\delta_{rm}\cot(k_m a). \end{aligned} \tag{4.17}$$

The infinite sum over n_z was evaluated by partial fraction expansion and manipulation of the digamma function as shown in Appendix A.

Using equation 4.15, Z^{12}_{rm} becomes

$$Z^{12}_{rm} = jk\rho c \int_{z=0}^{a} \int_{x_0=0}^{a} \sum_{n_x} \sum_{n_z} \frac{\cos(\frac{n_x\pi}{a}x)\cos(\frac{n_x\pi}{a}z_0)\cos(\frac{m\pi}{a}x)\cos(\frac{r\pi}{a}z_0)}{a^3\Lambda_{n_x}\Lambda_{n_z}\sqrt{\Lambda_m\Lambda_r}[(\frac{n_x\pi}{a})^2+(\frac{n_z\pi}{a})^2-k^2]}$$

$$= \quad jk\rho c \, \frac{1}{a\sqrt{\Lambda_m \Lambda_r}[(\frac{m\pi}{a})^2 + (\frac{r\pi}{a})^2 - k^2]}. \tag{4.18}$$

Given the impedance matrix $\bar{Z}$ and hence the normalized impedance matrix $\bar{\eta}$, the reflection and transmission coefficients can now be calculated from equation 4.14

Figures 4.3 to 4.8 are the magnitude of the pressure reflection and transmission coefficients of a right angle bend. They match the theoretical results of Shepherd and Cabelli [59] who used a finite element technique instead of a modal technique. Also shown in figures 4.3 to 4.7 are the experimental measurements of Shepherd and Cabelli which match the theory very well.

Figure 4.3 shows the magnitude of the pressure reflection coefficients for an incident plane wave. At low frequencies $|R_{00}|$ approaches zero as expected. Also as expected, $|R_{20}|$ and $|R_{10}|$ are zero since there is no coupling at low frequencies. As frequency increases all the reflection coefficients are rising. However, remember that until the frequency is above the cut-off of a given mode, it is evanescent and even if part of the plane wave is reflected into it, it cannot propagate. At the cut-off frequency of the first mode the junction region has a resonance and the self reflection coefficient approaches unity because the impedance of the junction is very high. The coupling coefficients go to zero. Again when the frequency reaches the cut-off frequency of the second mode there is a junction region resonance and the plane wave reflection coefficient goes to unity. While it appears that $|R_{00}|$ is always larger than the coupling coefficients above the cut-off frequency of the first mode, there is a significant part of the plane wave coupled into

the other modes. The theoretical results match the experimental measurements of Shepherd and Cabelli quite well, with most of the theoretical values within the error of the measurements.

In figure 4.4 are shown the magnitudes of the pressure reflection coefficients for an incident first mode. At the cut-off frequency of the first mode the magnitude of the first mode self reflection coefficient $|R_{11}|$ is unity, and there is no coupling into the other modes. Unlike the plane wave mode, the coupling coefficient $|R_{01}|$ is larger than the self reflection coefficient $|R_{11}|$ in the region of ka =5, showing that there is significant modal coupling at higher frequencies. Again the theoretical results are within the error of the measurements.

In figure 4.5 are shown the magnitudes of the pressure self and mutual reflection coefficients for an incident second mode. Close to the cut-off frequency of the third mode the coupling between the second and first mode is greater than the self reflection of the second mode. The measurements do not match the theory quite as well as for the lower order mode reflection coefficients. This is to be expected as measurements of the second mode are more difficult than for the lower modes.

Figure 4.6 shows the magnitude of the pressure transmission coefficients for an incident plane wave. At low frequencies $|T_{00}|$ approaches unity as expected. At the cut-off frequency of the first mode, the plane wave is not transmitted (as expected since $|R_{00}| = 1$) but the transmission coefficient $|T_{10}|$ is quite large, showing that much of the plane wave is transmitted to the first mode. This is also expected as at the cut-off frequency of the first mode, the trace wavenumber of the incident plane wave mode matches the trace wavenumber of a transmitted first mode. At the cut-off frequency of

the second mode $|T_{20}|$ gets large while $|T_{01}|$ and $|T_{00}|$ are small. Again the plane wave is converted into the mode which is just above its cut-off frequency because the trace wavenumbers match. The theoretical results are within the error of the measurements.

Figure 4.7 shows the magnitudes of the pressure transmission coefficients for an incident first mode. At the cut-off frequency of the first mode there is no transmission - as expected because $|R_{11}| = 1$ at that frequency. At the cut-off frequency of the second mode the $|T_{12}|$ is large again indicating significant modal coupling. Most of the theoretical results are within the error of the measurements.

Figure 4.8 shows the magnitudes of the pressure transmission coefficients for an incident second mode. The results are as expected, there is no self transmission at the cut-off frequency of the second mode mode and good coupling to the first mode which matches the trace wavenumber of the incident second mode. No experimental measurements were available for comparison.

As a result of the above plots, some simple conclusions can be made. First, at the cut-off frequency of a mode, the self reflection coefficient is unity while the self transmission coefficient is zero. This is because of the resonances of the junction region. Perhaps more importantly, the coupling between a mode and the next higher mode is very large when the frequency is just above the cut-off frequency of the higher mode. This is because of trace wavenumber matching of the incident mode and transmitted mode. The plane wave mode will couple greatly into whichever mode is just above its cut-off frequency. It is quite clear that a right angle bend will significantly change the modal structure of the propagating wave at all but very low frequencies.

The theoretical results match the experimental results of Shepherd and Cabelli quite well. The theory is verified and can be used with confidence to determine the scattering parameters of other types of junctions.

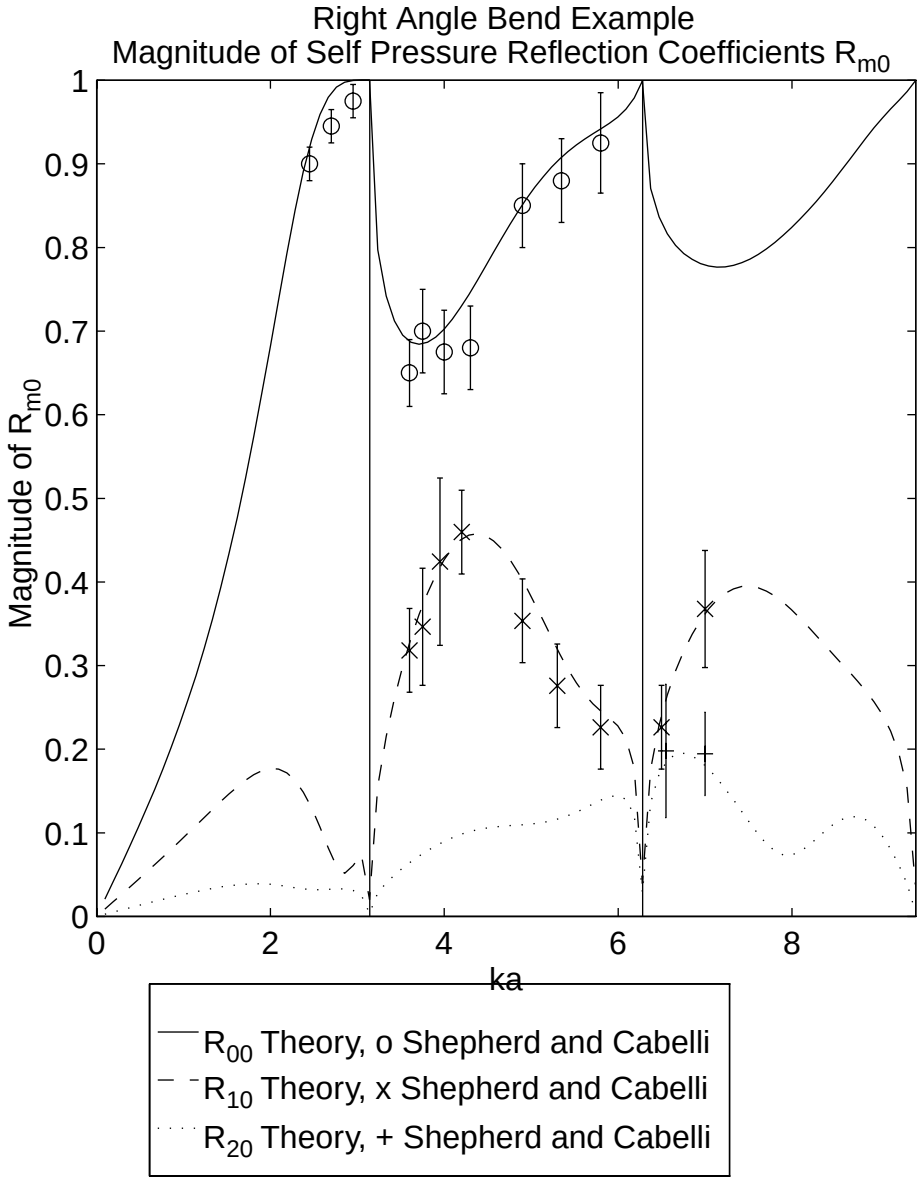

Fig. 4.3. Magnitude of the pressure reflection coefficients of a right angle bend, R_{m0}, for incident mode 0, into reflected modes $m = 0, 1, 2$.

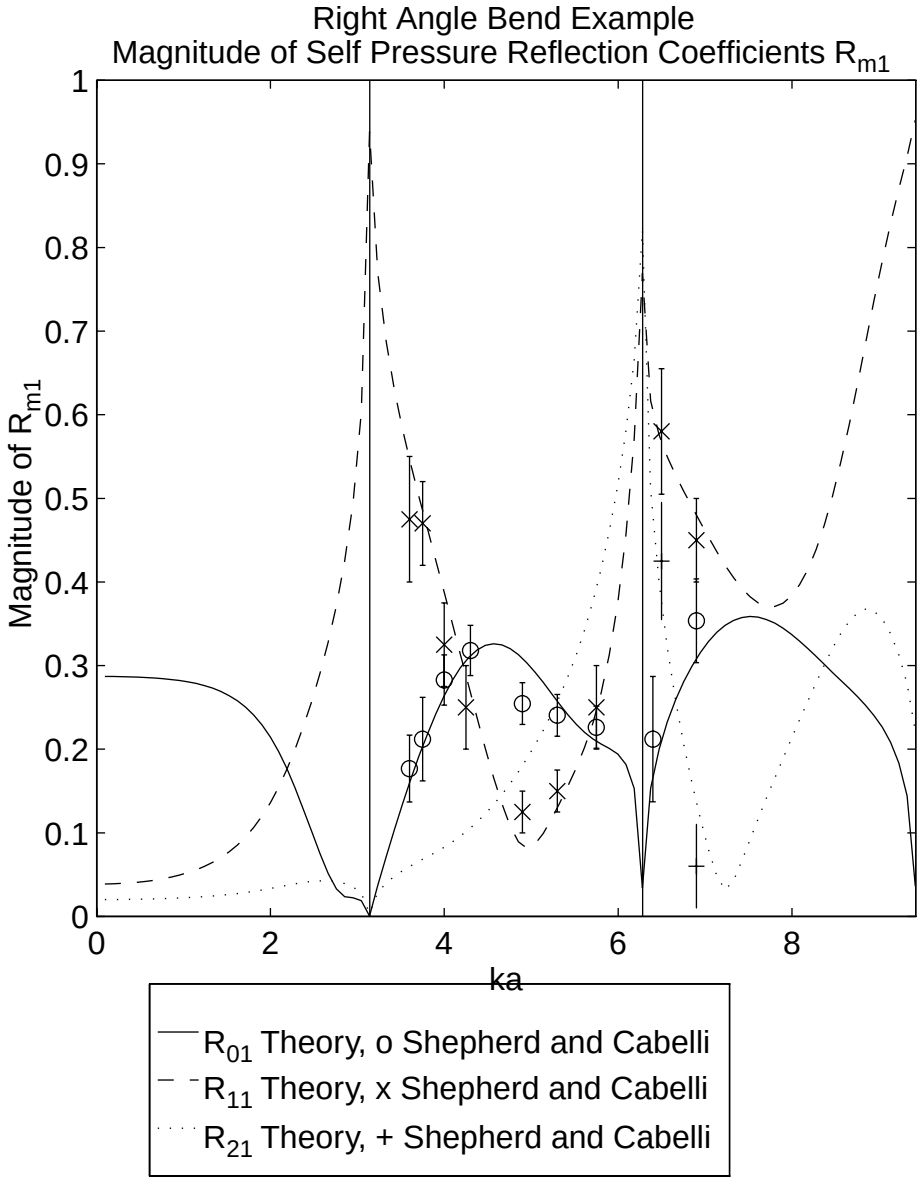

Fig. 4.4. Magnitude of the pressure reflection coefficients of a right angle bend, R_{m1}, for incident mode 1, into reflected modes $m = 0, 1, 2$.

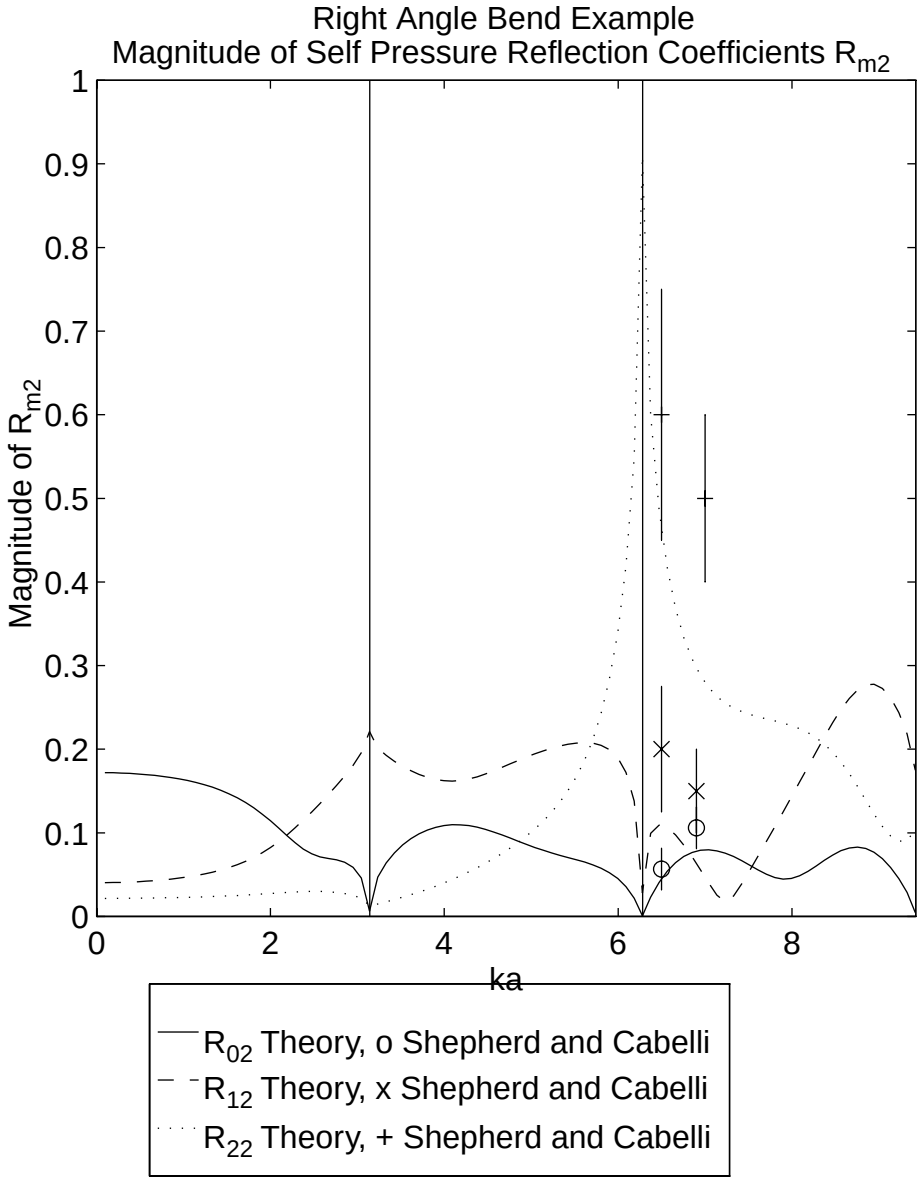

Fig. 4.5. Magnitude of the pressure reflection coefficients of a right angle bend, R_{m2}, for incident mode 2, into reflected modes $m = 0, 1, 2$.

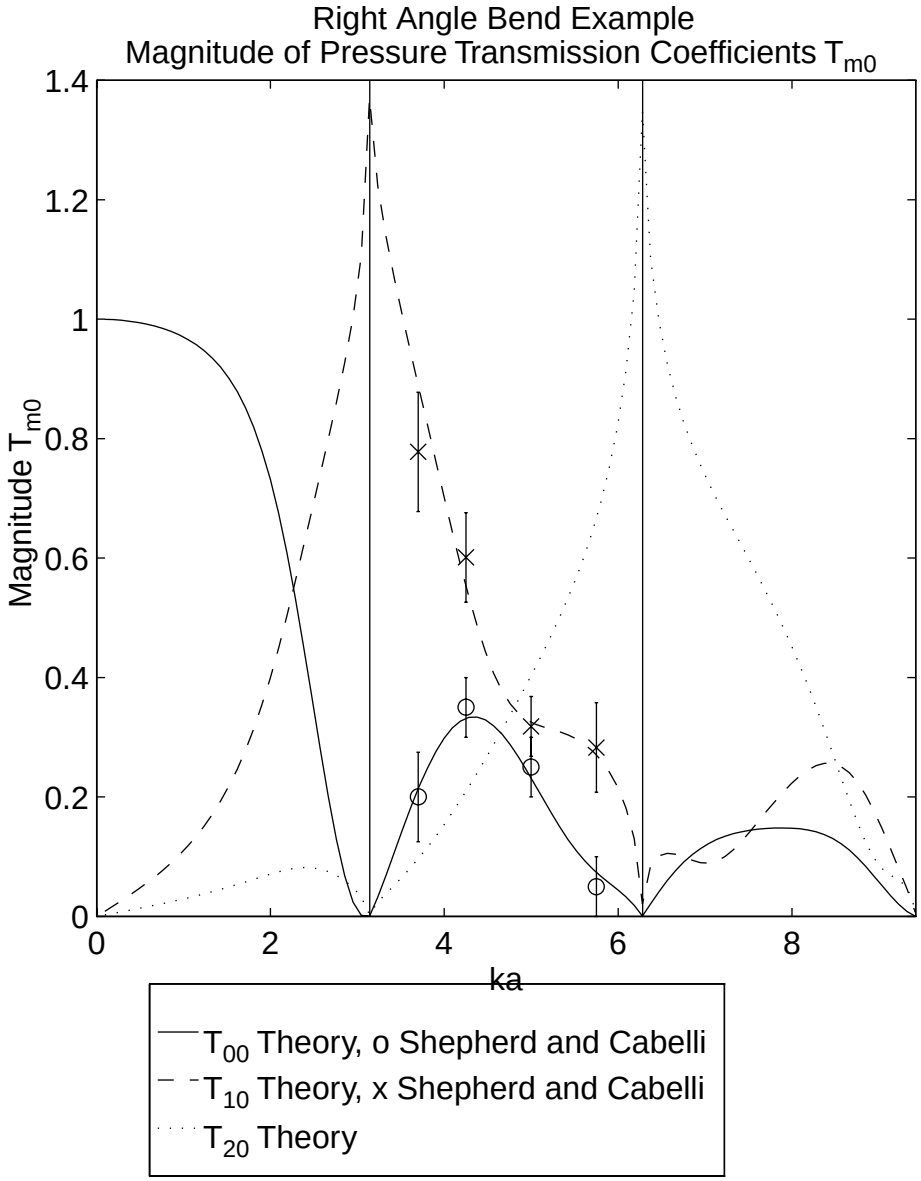

Fig. 4.6. Magnitude of the pressure transmission coefficients of a right angle bend, T_{m0}, for incident mode 0, into transmitted modes $m = 0, 1, 2$.

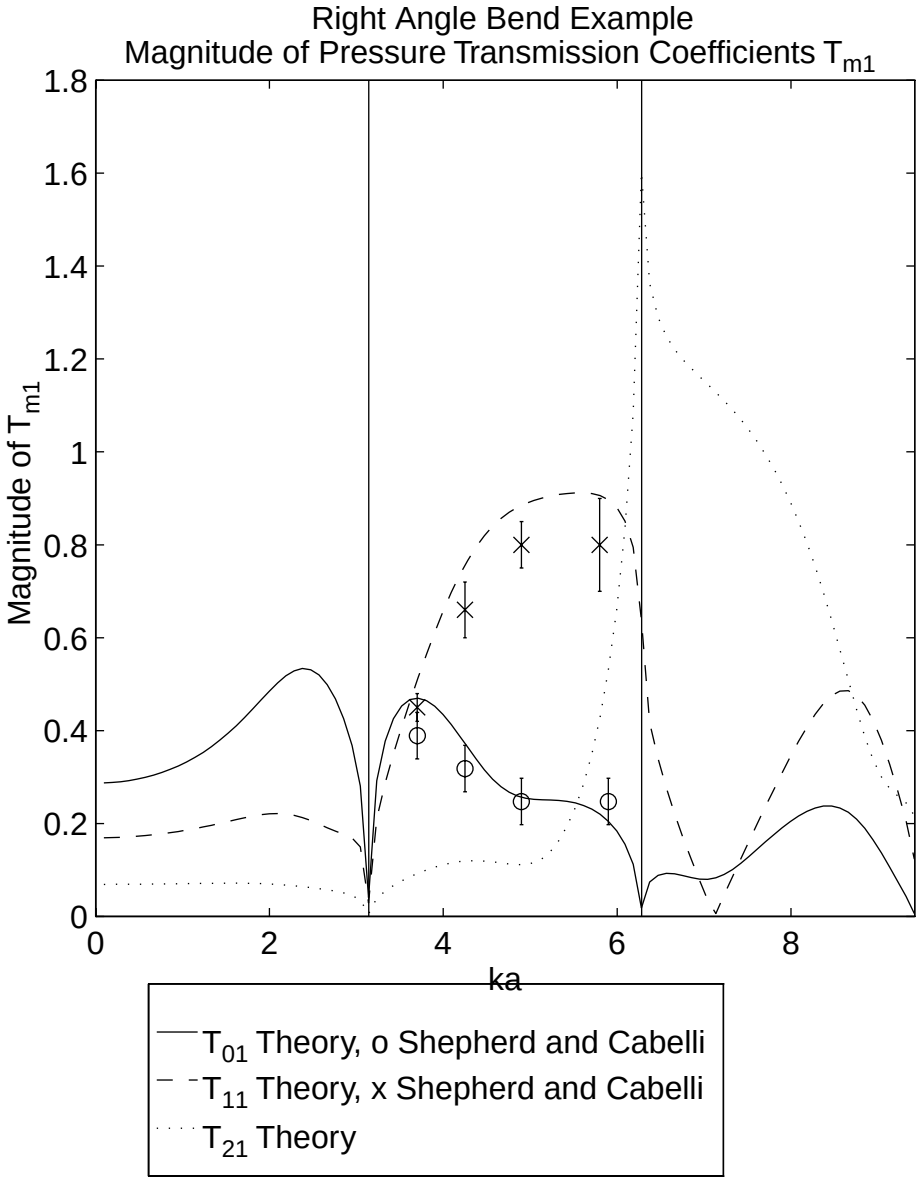

Fig. 4.7. Magnitude of the pressure transmission coefficients of a right angle bend, T_{m1}, for incident mode 1, into transmitted modes $m = 0, 1, 2$.

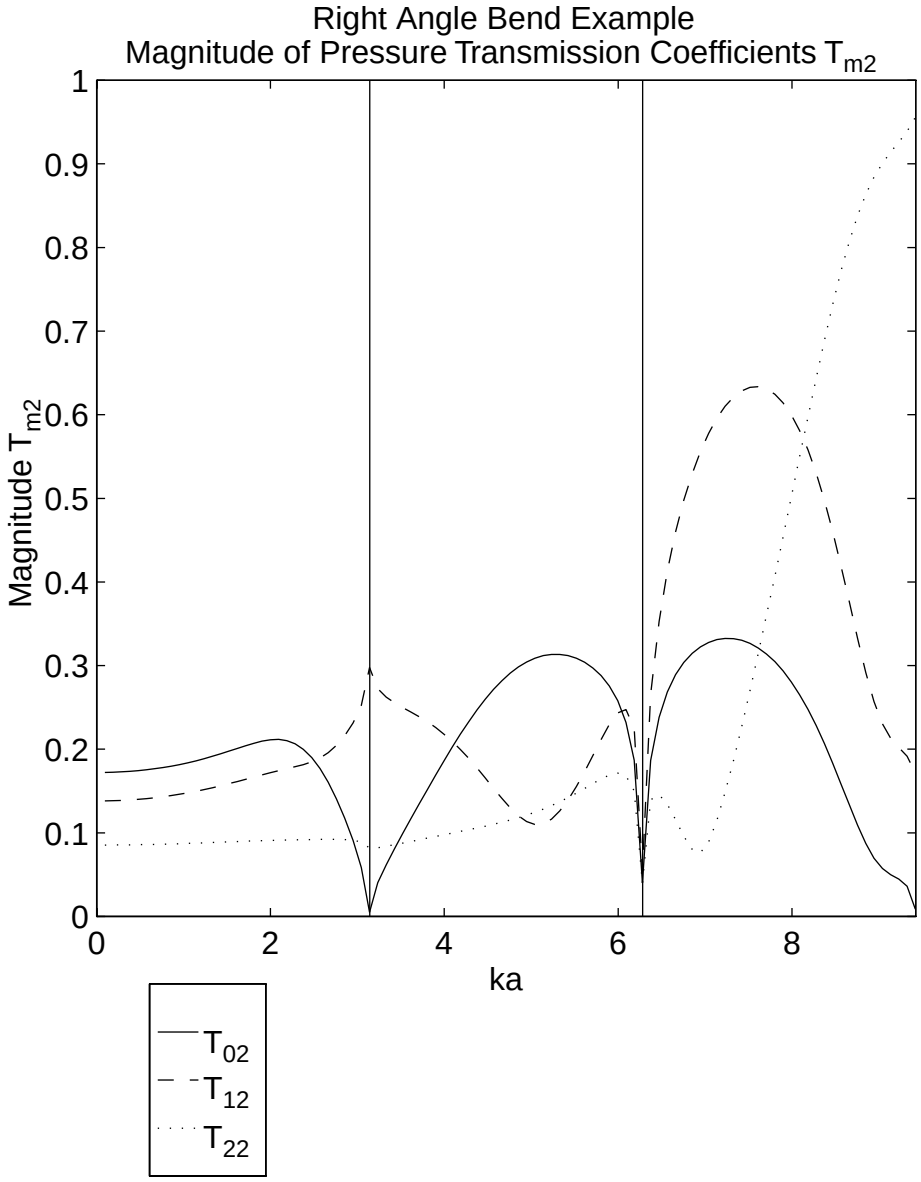

Fig. 4.8. Magnitude of the pressure transmission coefficients of a right angle bend, T_{m2}, for incident mode 2, into transmitted modes $m = 0, 1, 2$.

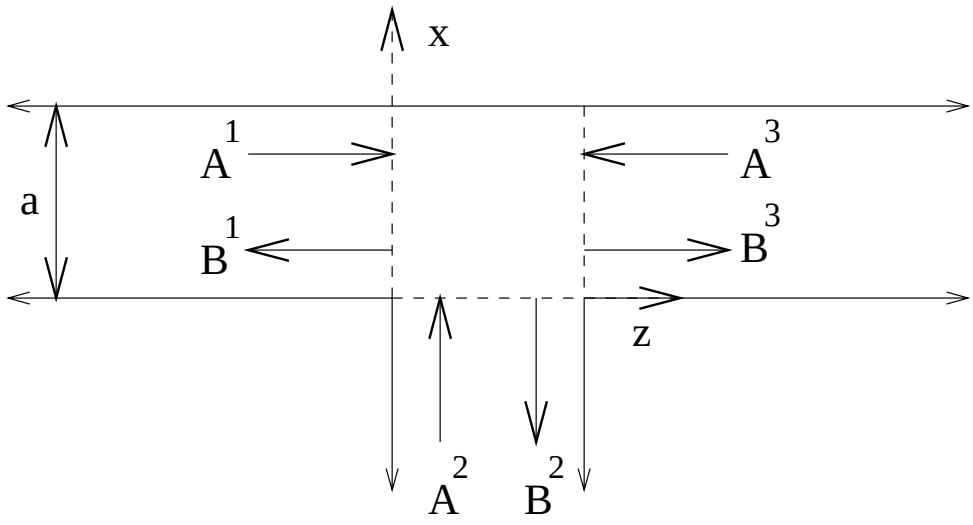

Fig. 4.9. Geometry of a T Junction

4.2.2 A T Junction

Consider the T junction as shown in 4.9. As in the previous example, there is no y discontinuity thus y can be eliminated from the problem. The Green's function G_J is the same as the previous problem. In fact, the problem is so similar to the previous example, that Z^{11} and Z^{12} are the same. By symmetry it is easy to see that $Z^{12} = Z^{21} = Z^{23} = Z^{32}$, $Z^{33} = Z^{11}$ and $Z^{13} = Z^{31}$.

For this problem the local coordinates are

$$x_1 = x, \quad z_1 = z, \quad x_2 = z, \quad z_2 = x, \quad x_3 = x, \quad z_3 = (a - z). \tag{4.19}$$

Z_{rm}^{13} is given by

$$
\begin{aligned}
Z_{rm}^{13} &= jk\rho c \int_{x=0}^{a}\int_{x_0=0}^{a} \sum_{n_x}\sum_{n_z} \frac{\cos(\frac{n_x\pi}{a}x)\cos(\frac{n_x\pi}{a}x_0)\cos(\frac{n_z\pi}{a}a)\cos(\frac{m\pi}{a}x)\cos(\frac{r\pi}{a}x_0)}{a^3\Lambda_{n_x}\Lambda_{n_z}\sqrt{\Lambda_m\Lambda_r}[(\frac{n_x\pi}{a})^2+(\frac{n_z\pi}{a})^2-k^2]} \\
&= jk\rho c\ \delta_{rm}\sum_{n_z}\frac{(-1)^{n_z}}{a\Lambda_{n_z}[(\frac{m\pi}{a})^2+(\frac{n_z\pi}{a})^2-k^2]} \\
&= \frac{jk\rho c\ \ \delta_{rm}}{2k_m}[\cot(\frac{k_m a}{2})+\tan(\frac{k_m a}{2})]. \qquad (4.20)
\end{aligned}
$$

Again in equation 4.20 the infinite summation was evalued by use of digamma functions as shown in appendix A.

Figures 4.10 through 4.24 are the magnitudes of the reflection and transmission coefficients for a T junction.

Figure 4.10 shows the magnitudes of pressure reflection coefficients for a plane wave incident at one end of a T junction. At low frequencies the reflection coefficient approaches the expected 1/3. As frequency rises the coefficient drops a bit but then quickly rises to unity at the cut-off frequency of the first mode. At that frequency there is no reflected coupling into other modes. This is because of a resonance of the junction region. As the frequency goes up, the self reflection coefficient quickly drops and the coupling coefficient between the plane wave and the first mode become larger. At the cut-off frequency of the second mode the self reflection coefficient is zero. The self reflection coefficient then rises to unity again at the cut-off frequency of the third mode. At frequencies between the cut-off of the first and second mode the coupling from the plane wave mode to the first mode is larger than the self reflection coefficient alone.

Figure 4.11 shows the magnitudes of the pressure reflection coefficients for a plane wave incident from the side branch of the T. At low frequencies the reflection coefficient approaches 1/3 and rises smoothly to unity at the cut-off frequency of the first mode. There is not significant coupling between modes until close to the cut-off of the second mode where significant coupling between the plane wave and first mode exists.

Figure 4.12 shows the magnitudes of the pressure transmission coefficient for the plane wave mode from the side branch to the end. As expected, the low frequency limit is 2/3. The self transmission coefficient drops to zero at the cut-off frequency of the first mode. The coupling coefficient from the plane wave to the first mode is quite high near the cut-off frequency but drops at the cut-off frequency. It is expected to be high near the cut-off frequency from trace wavenumber matching, but the reason for the drop at the cut-off frequency is unknown. At the cut-off frequency of the second mode the coupling between the plane wave and the second mode is very high again (because of trace wavenumber matching) while the self reflection coefficient is zero.

Figure 4.13 shows the magnitudes of the pressure transmission coefficients for the plane wave from one end to the side branch of the T. At low frequencies the value of the self transmission coefficient approaches the expected 2/3. At the cut-off frequency of the first mode the plane mode is well coupled into the first mode while the self transmission coefficient is zero. At the cut-off frequency of the second mode the plane wave mode is well coupled into the second mode while the self transmission coefficient is zero. Again the coupling to the higher order modes is expected because of trace wavenumber matching at the cut-off frequencies of the modes. Clearly modal coupling is important.

Figure 4.14 shows the magnitudes of the pressure transmission coefficient for the plane mode between the two ends of the T. The plane wave coefficient starts at 2/3 rises a little and drops sharply to zero at the cut-off frequency of the first mode. This is because of the cavity resonance which causes a high impedance to be seen to the incoming wave. It then sharply rises with increasing frequency reaching unity at the cut-off frequency of the second mode. The mutual coupling coefficients are both quite small compared to the self coupling coefficients.

Figure 4.15 shows magnitudes of the pressure reflection coefficients for the first mode incident at one end of the T. At the cut-off frequency for the mode, the reflection coefficient approaches unity. It wavers a bit and drops toward zero at the cut-off frequency of the second mode. There is not significant coupling between modes until the cut-off frequency of the second mode, where the coupling from the first mode to the second mode is significant.

In figure 4.16 is shown the magnitudes of the pressure reflection coefficients for the first mode incident at the side branch of the T. The self reflection coefficient is large at the cut-off frequency of the first mode and stays pretty high for all frequencies.

Figure 4.17 shows the magnitudes of the pressure transmission coefficients for the first mode from the side branch to the end. At the cut-off frequency of the first mode the transmission coefficients are all zero since the reflection coefficient is unity. There is significant coupling to the second mode near the cut-off frequency of the second mode.

Figure 4.18 shows the magnitudes of the pressure transmission coefficients for the first mode from the end to the side branch of the T. At the cut-off frequency of the first

mode the transmission coefficients are all zero. Above the cut-off frequency of the second mode the coupling coefficient between the first and second mode is very high.

Figure 4.19 shows the magnitudes of the pressure transmission coefficient for the first mode between the two ends. There is little coupling between modes but the transmission coefficient is small for frequencies near the cut-off frequency of the first mode. The transmission coefficient approaches unity at the cut-off frequency of the second mode.

Figure 4.20 shows the magnitudes of the pressure reflection coefficients for the second mode incident at one end of the T. At the cut-off frequency of the second mode, the self reflection coefficient approaches unity. There is little modal coupling.

Figure 4.21 shows the magnitudes of the pressure reflection coefficients for the second mode incident at the side branch of the T. The self reflection coefficient approaches unity at the cut-off frequency. Near the cut-off frequency of the third mode the mutual reflection coefficient into the first mode is larger than the self reflection coefficient.

Figure 4.22 shows the magnitudes of the pressure transmission coefficients for the second mode from the side branch to one end. The transmission coefficients are quite complicated but there is not significant modal coupling.

Figure 4.23 shows the magnitudes of the pressure transmission coefficients for the second mode from one end to the side branch of the T. Like the coefficient from the side to the end, the overall coupling is low.

Figure 4.24 shows the magnitudes of the pressure transmission coefficients for the second mode between the ends. There is little coupling between modes, but the self transmission coefficient is high.

From the above plots one can conclude that in general the side branch does not contribute heavily to modal coupling for transmission between the ends of the T, but it does affect the self transmission of the modes between the ends of the T. There is very significant coupling from the mode incident on the side branch to a another mode in the ends just above its cut-off frequency because of trace wavenumber matching (just as with the right angle bend). The modal coupling coefficient is often higher in magnitude of than the self transmission coefficient and self reflection coefficient. Clearly modal coupling with the side branch is very important.

In addition, one can see that, $|S_{00}^{21}|$, the magnitude of the coupling from the side branch plane wave mode to the plane wave mode in the T ends, drops to zero at the cut-off frequency and is quite small at higher frequencies. This is important because it says that a speaker mounted in the side of a duct is far less efficient at producing plane wave modes at high frequencies - something of practical concern in active noise control systems.

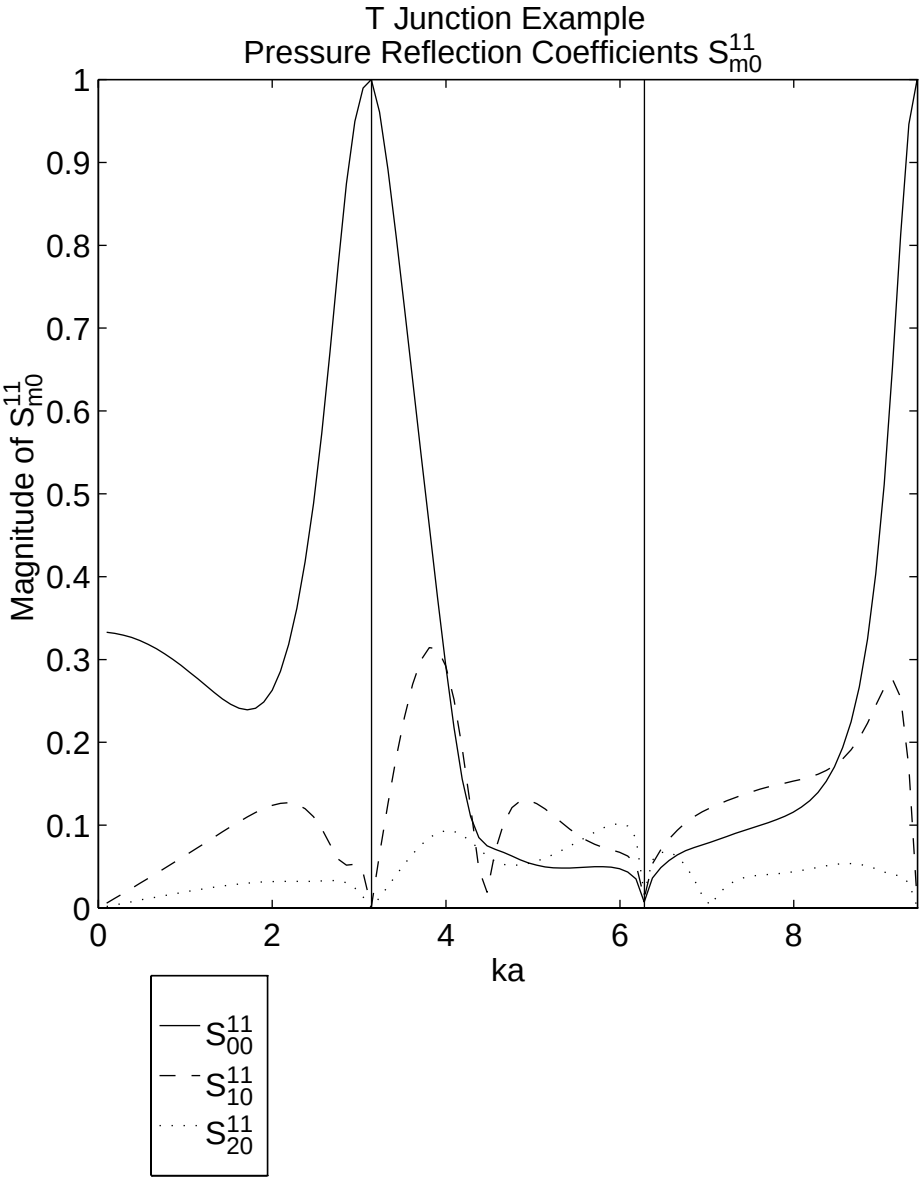

Fig. 4.10. Magnitude of the pressure reflection coefficients of one end of a T junction, S^{11}_{m0}, for incident mode 0 into reflected modes $m = 0, 1, 2$.

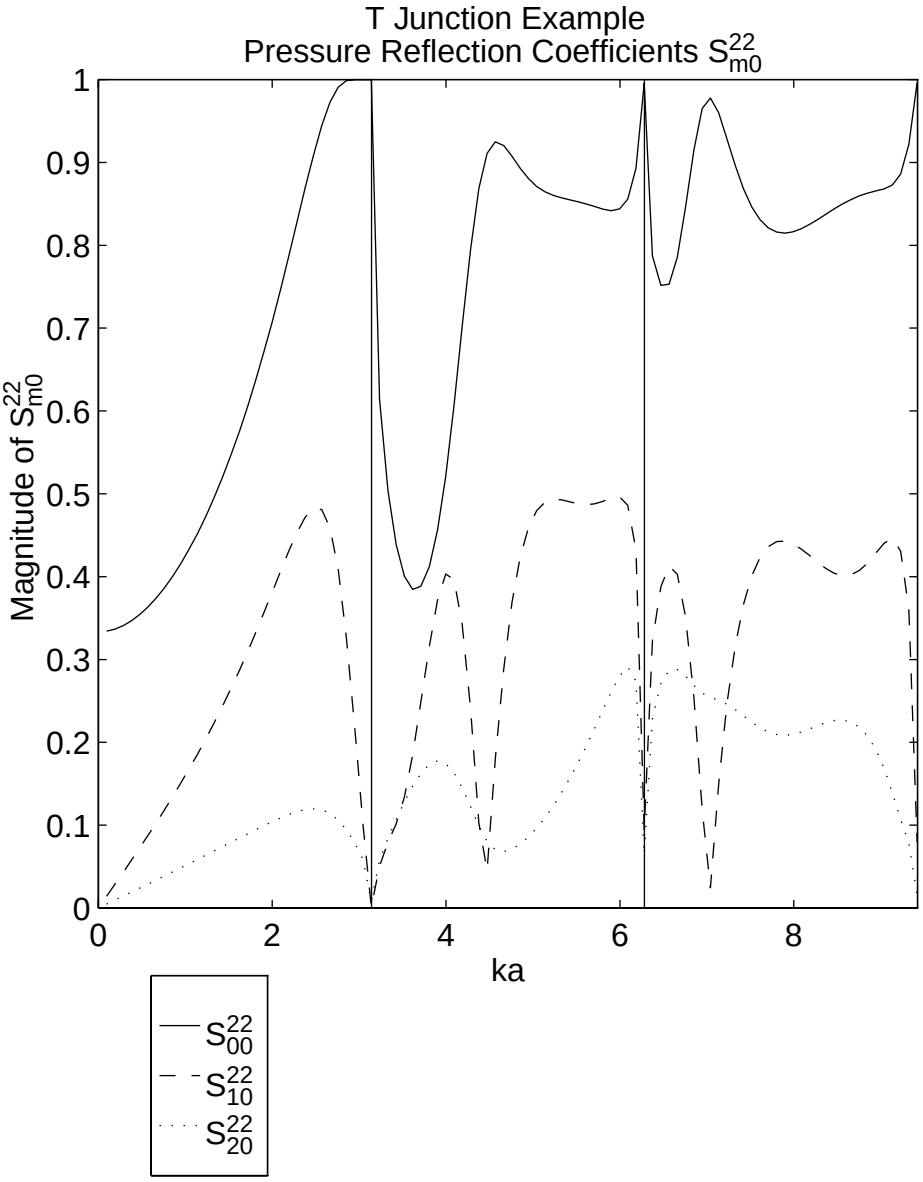

Fig. 4.11. Magnitude of the pressure reflection coefficients of the side branch of a T junction, S^{22}_{m0}, for incident mode 0 into reflected modes $m = 0, 1, 2$.

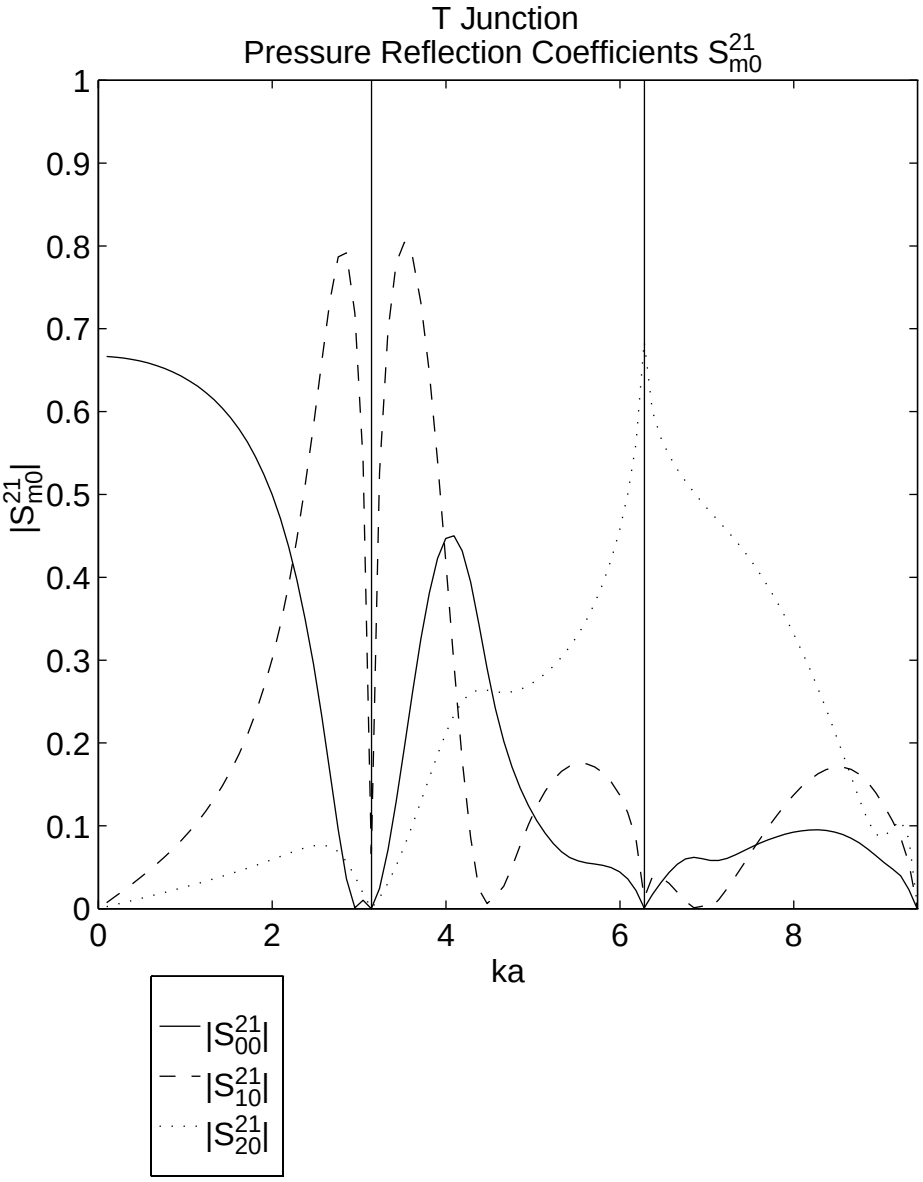

Fig. 4.12. Magnitude of the pressure transmission coefficients S^{21}_{m0}, from mode 0 in one end of a T to modes $m = 0, 1, 2$ in the side branch.

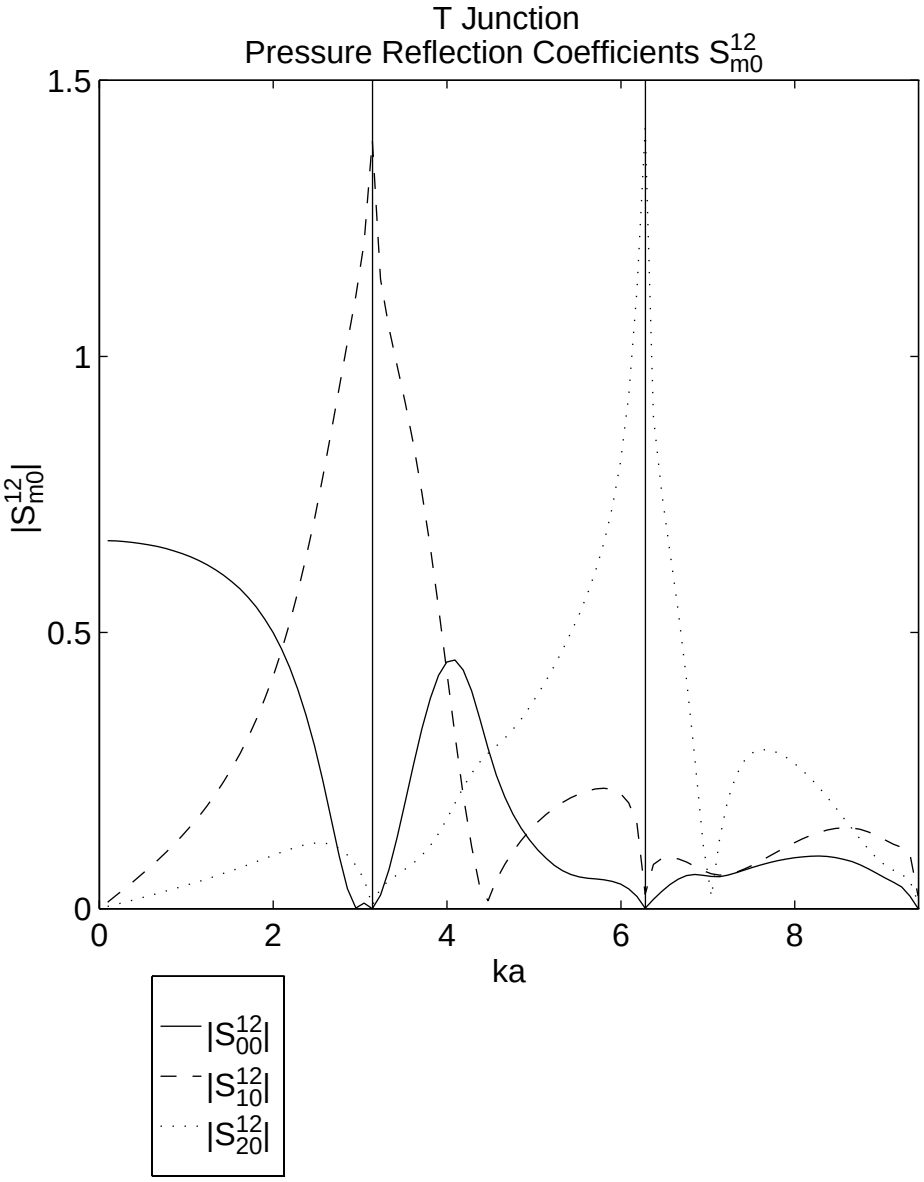

Fig. 4.13. Magnitude of the pressure transmission coefficients S^{12}_{m0}, from mode 0 in the side branch of a T to modes $m = 0, 1, 2$ in one end.

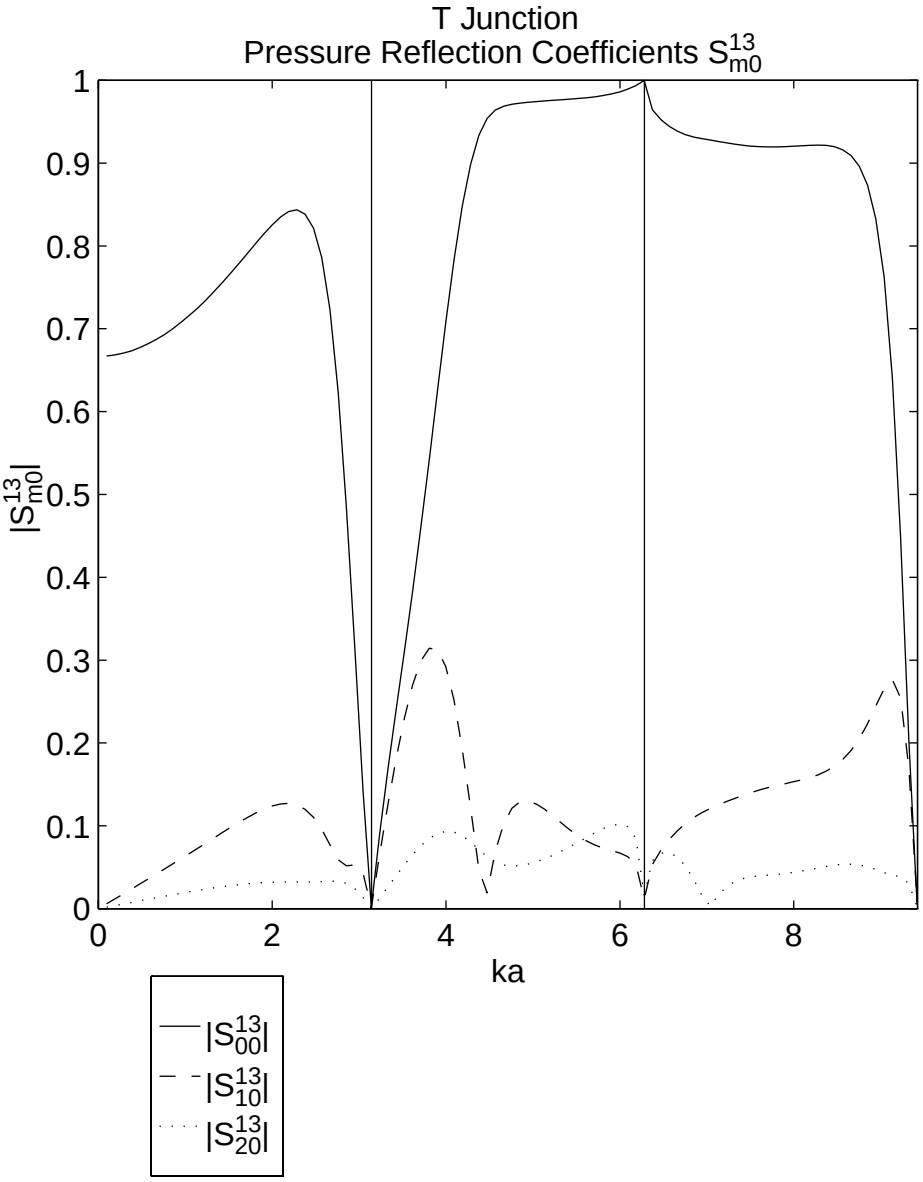

Fig. 4.14. Magnitude of the pressure transmission coefficients S^{13}_{m0}, from mode 0 in one end of a T to modes $m = 0, 1, 2$ in the other end.

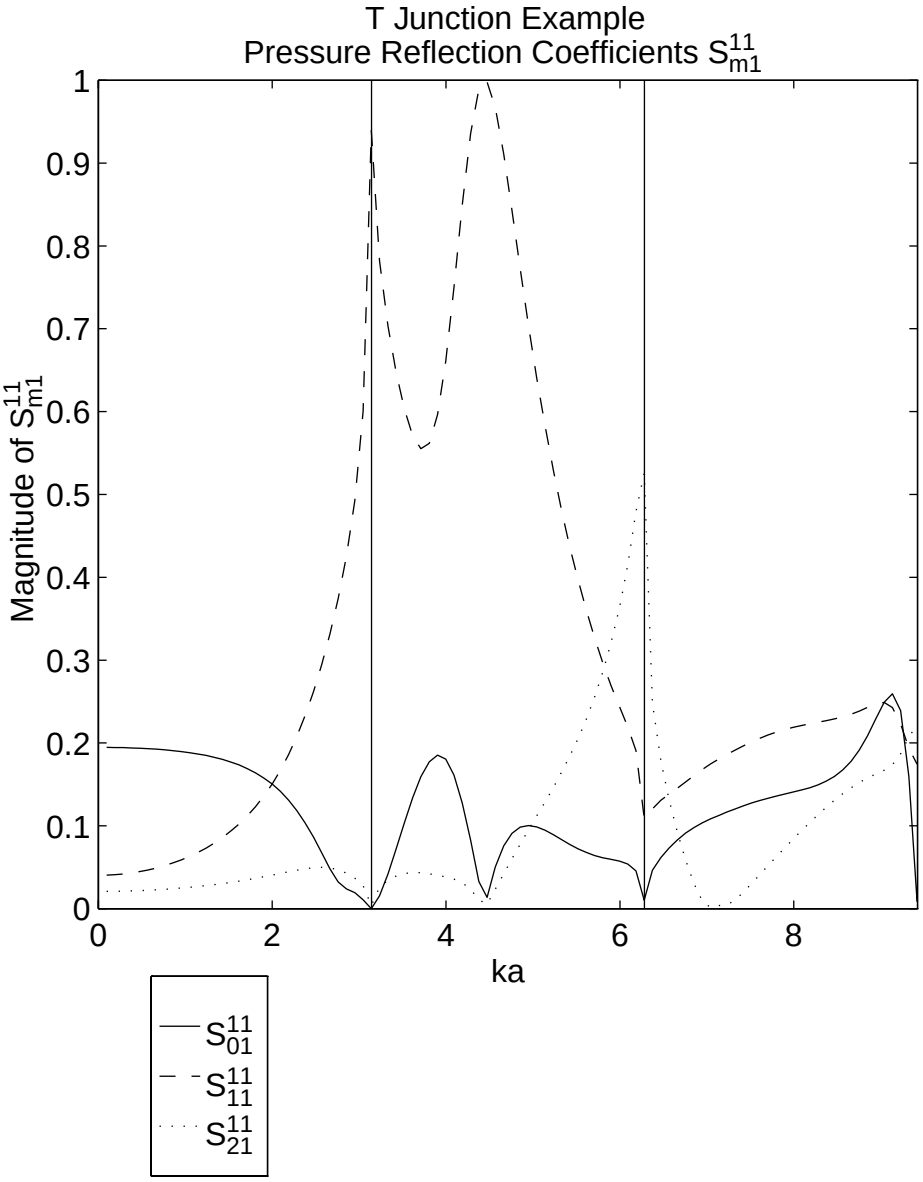

Fig. 4.15. Magnitude of the pressure reflection coefficients S^{11}_{m1}, end of a T junction for incident mode 1 into reflected modes $m = 0, 1, 2$.

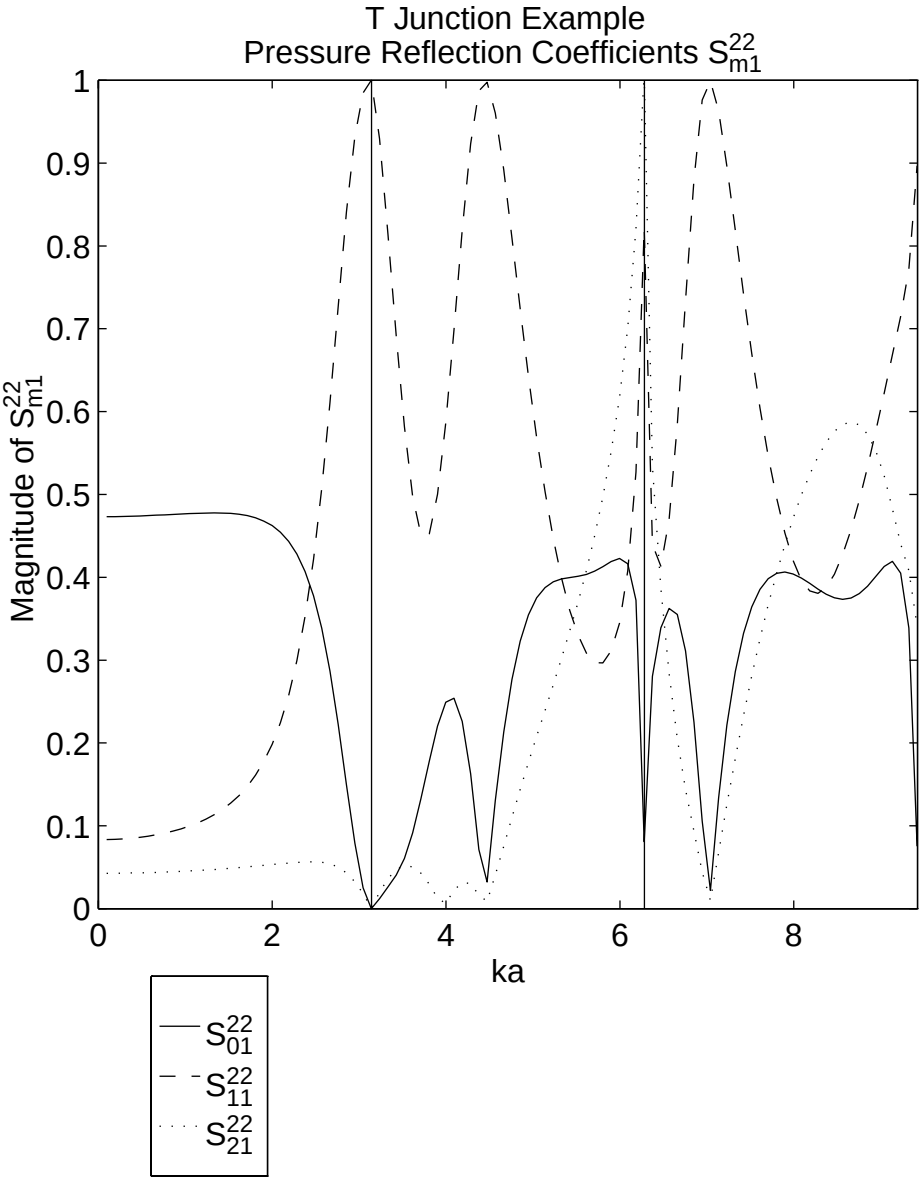

Fig. 4.16. Magnitude of the pressure reflection coefficients S^{22}_{m1}, from the side branch of a T junction for incident mode 1 into reflected modes $m = 0, 1, 2$.

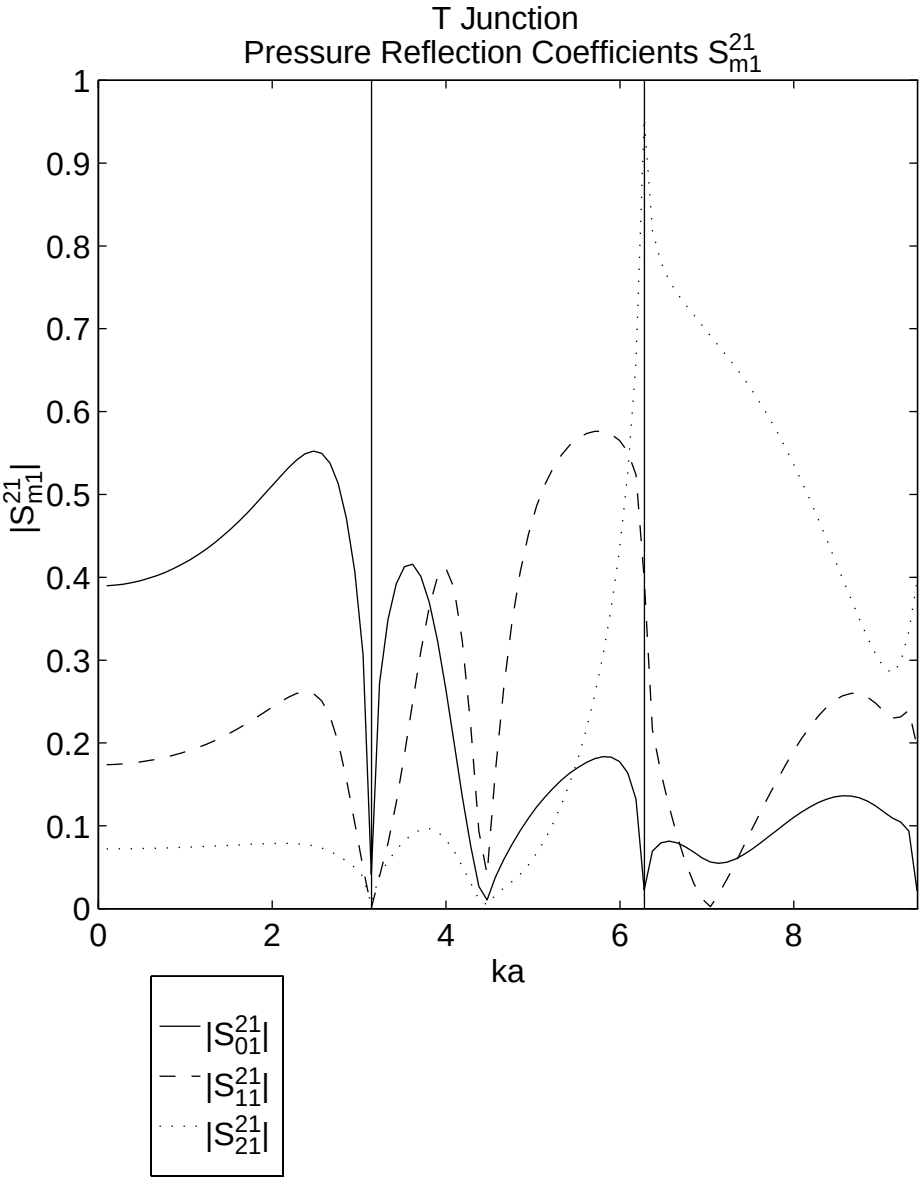

Fig. 4.17. Magnitude of the pressure transmission coefficients S^{21}_{m1}, from mode 1 in one end of a T to modes $m = 0, 1, 2$ in the side branch.

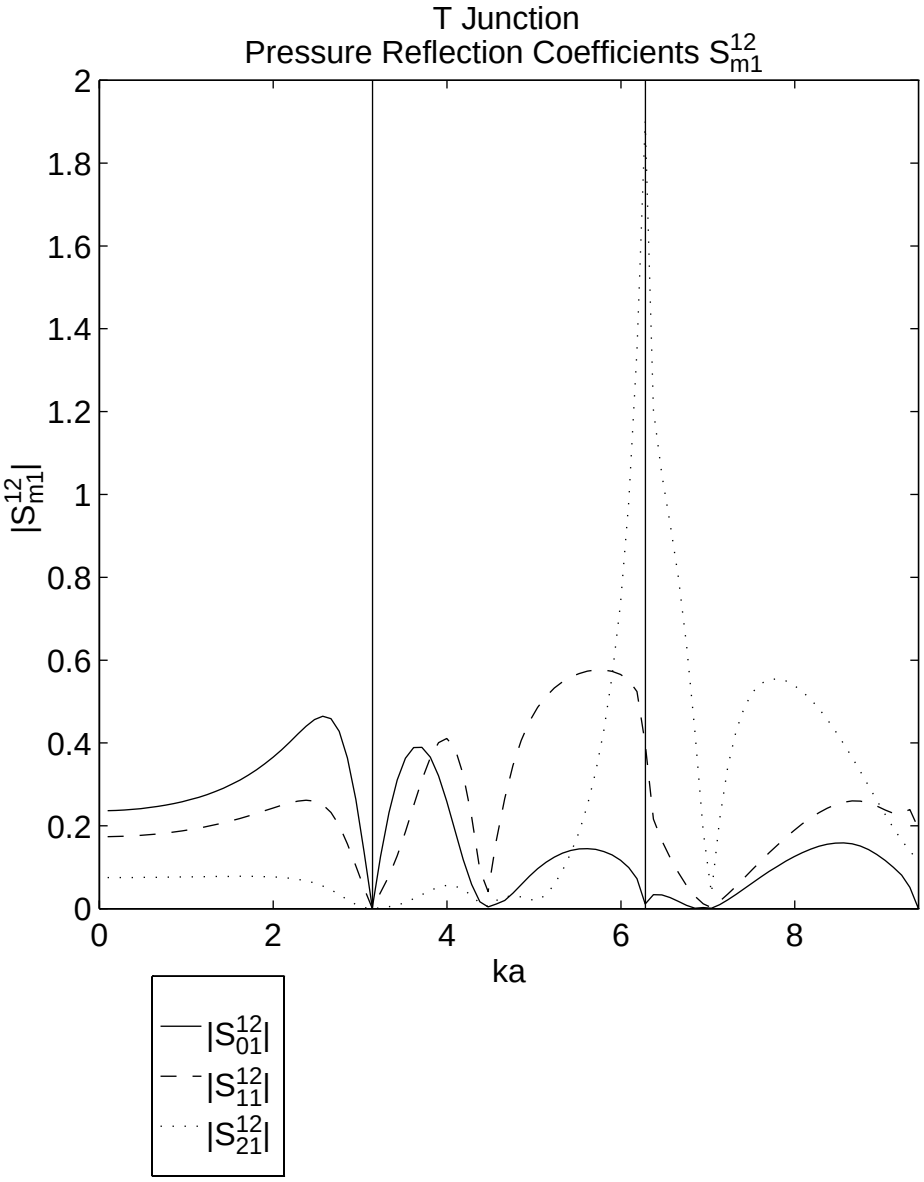

Fig. 4.18. Magnitude of the pressure transmission coefficients S^{12}_{m1}, from mode 1 in the side branch of a T to modes $m = 0, 1, 2$ in one end.

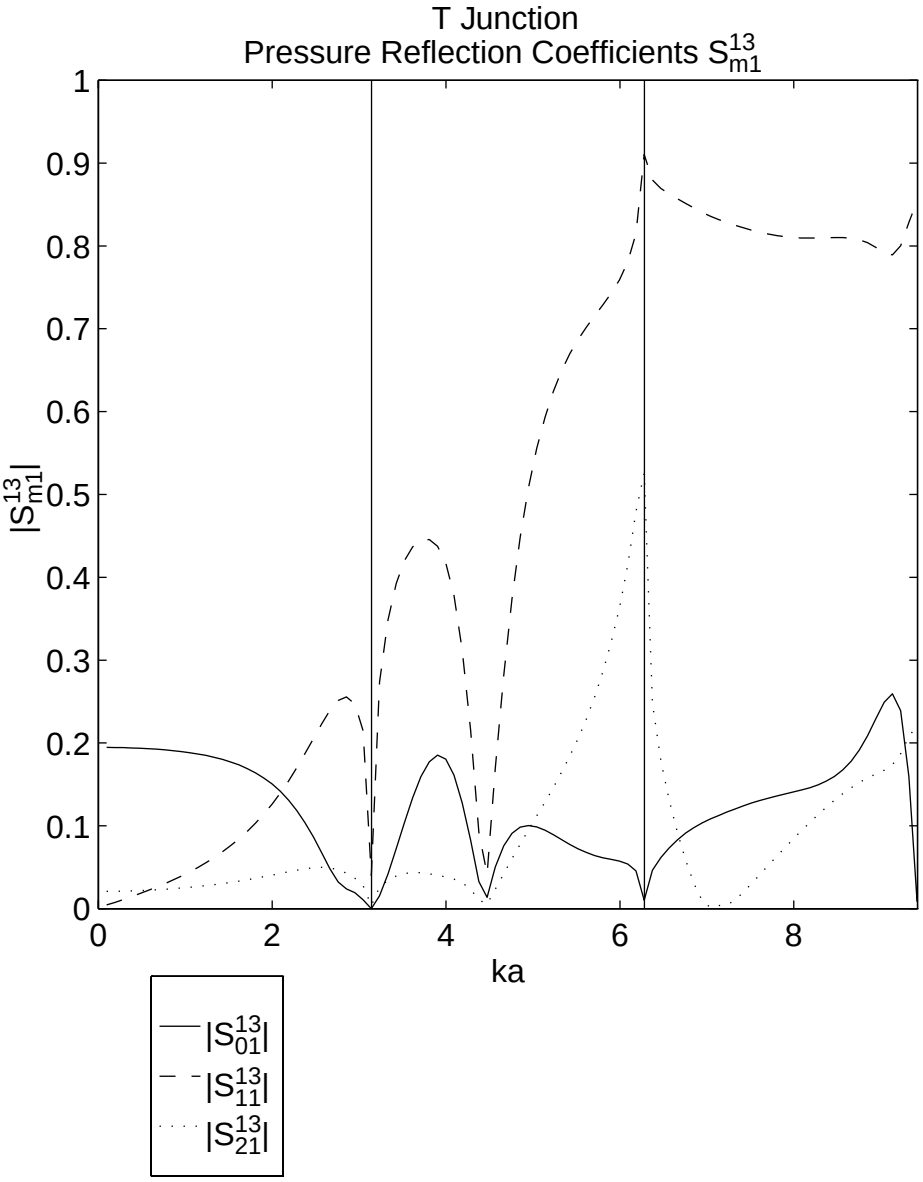

Fig. 4.19. Magnitude of the pressure transmission coefficients S^{13}_{m1}, from mode 1 in one end of a T to modes $m = 0, 1, 2$ in the other end.

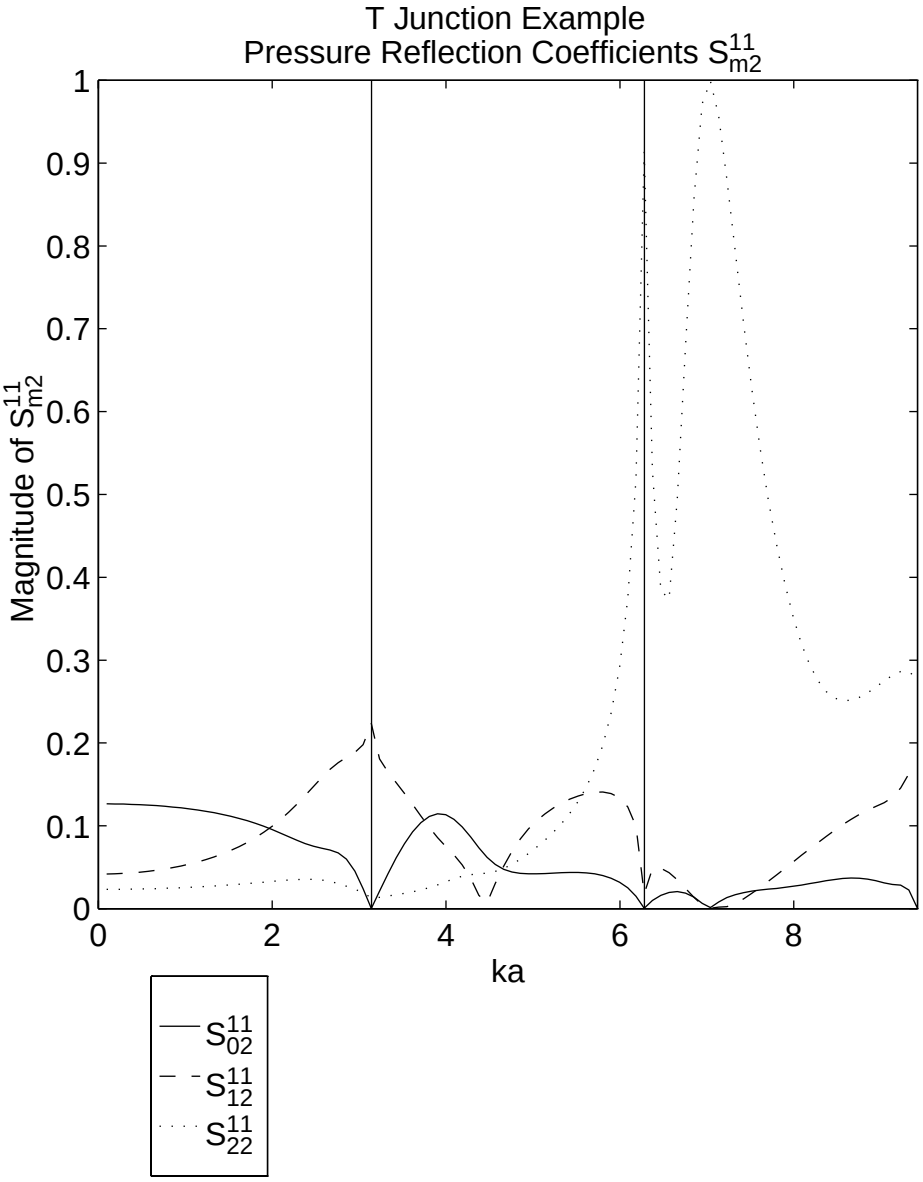

Fig. 4.20. Magnitude of the pressure reflection coefficients, S^{11}_{m2}, from of one end of a T junction for incident mode 2 into reflected modes $m = 0, 1, 2$.

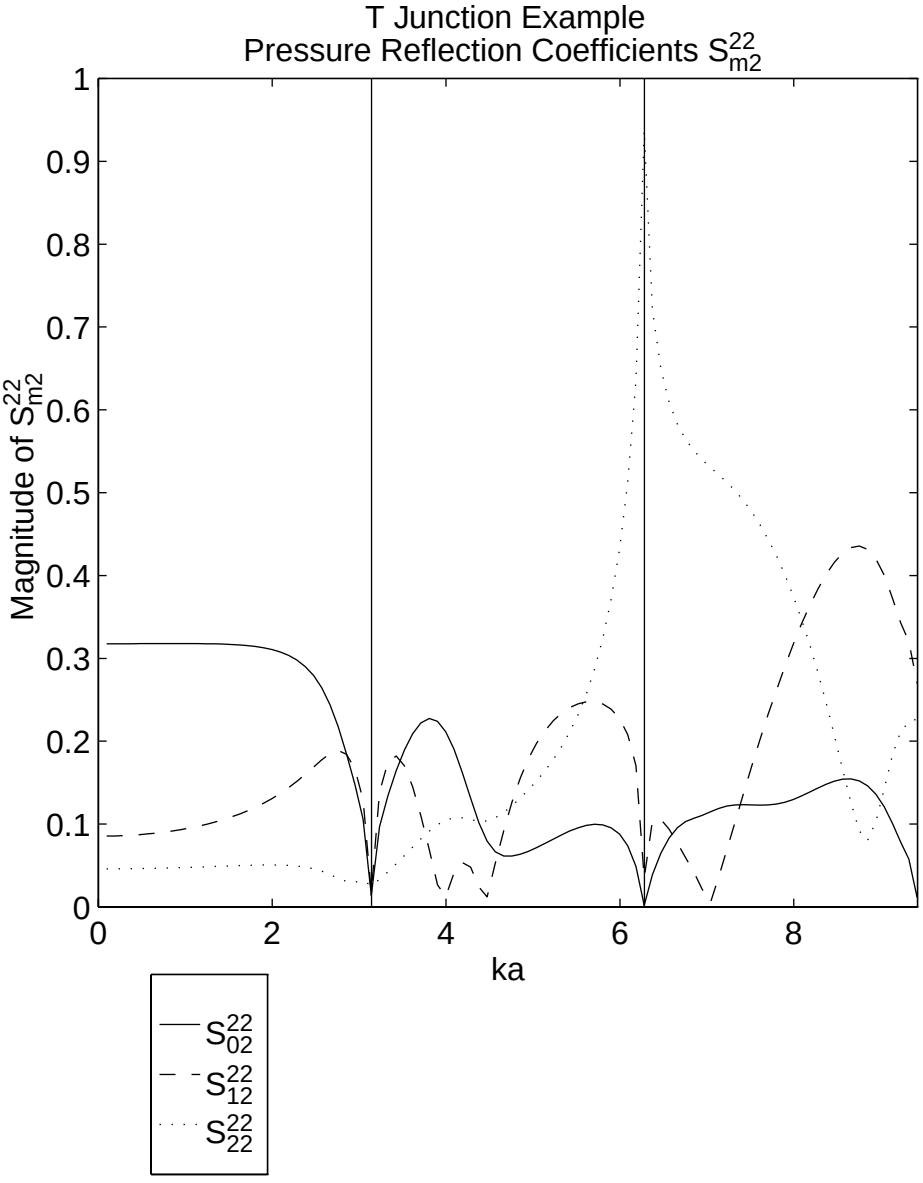

Fig. 4.21. Magnitude of the pressure reflection coefficients S^{22}_{m2}.
, of the side branch of a T junction for incident mode 2 into reflected modes $m = 0, 1, 2$.

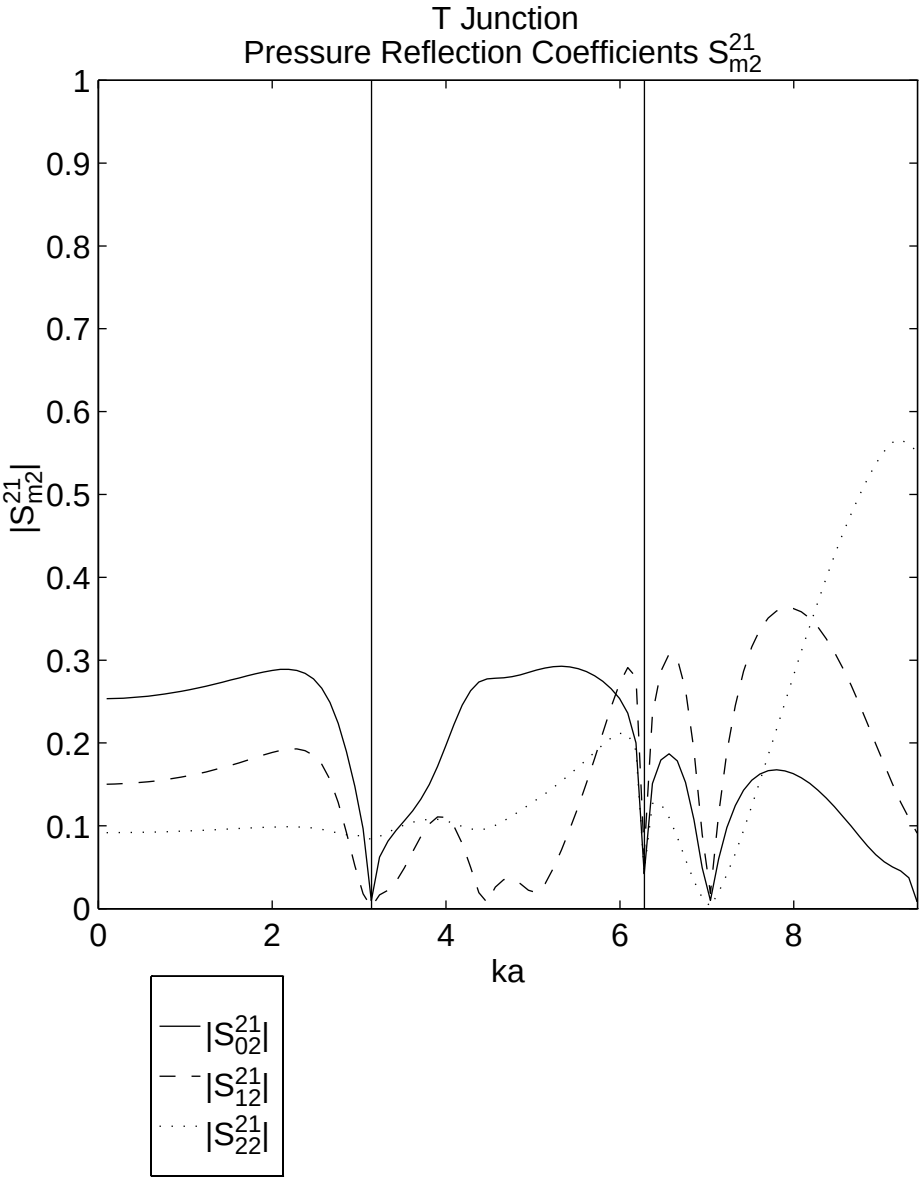

Fig. 4.22. Magnitude of the pressure transmission coefficients S^{21}_{m2}, from mode 2 in one end of a T to modes $m = 0, 1, 2$ in the side branch.

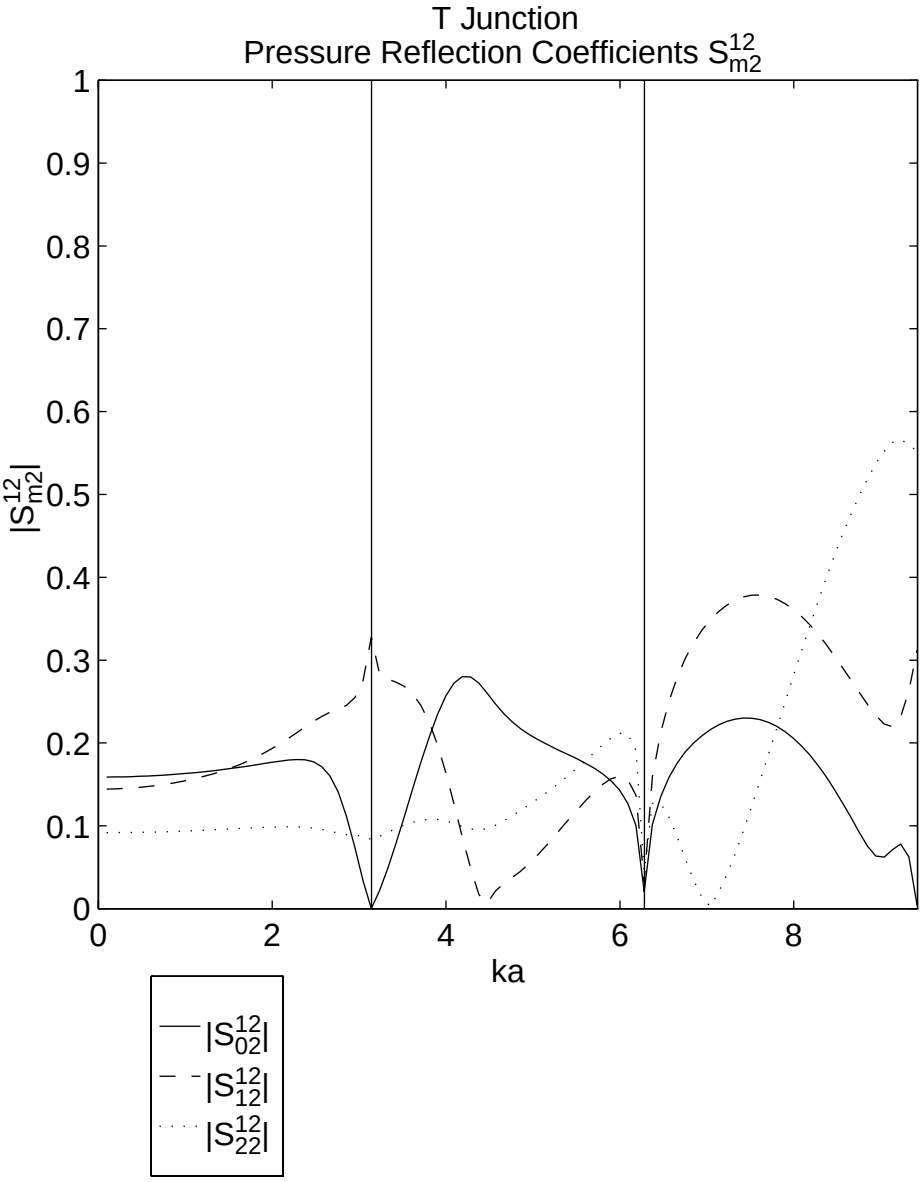

Fig. 4.23. Magnitude of the pressure transmission coefficients S^{12}_{m2}, from mode 2 in the side branch of a T to modes $m = 0, 1, 2$ in one end.

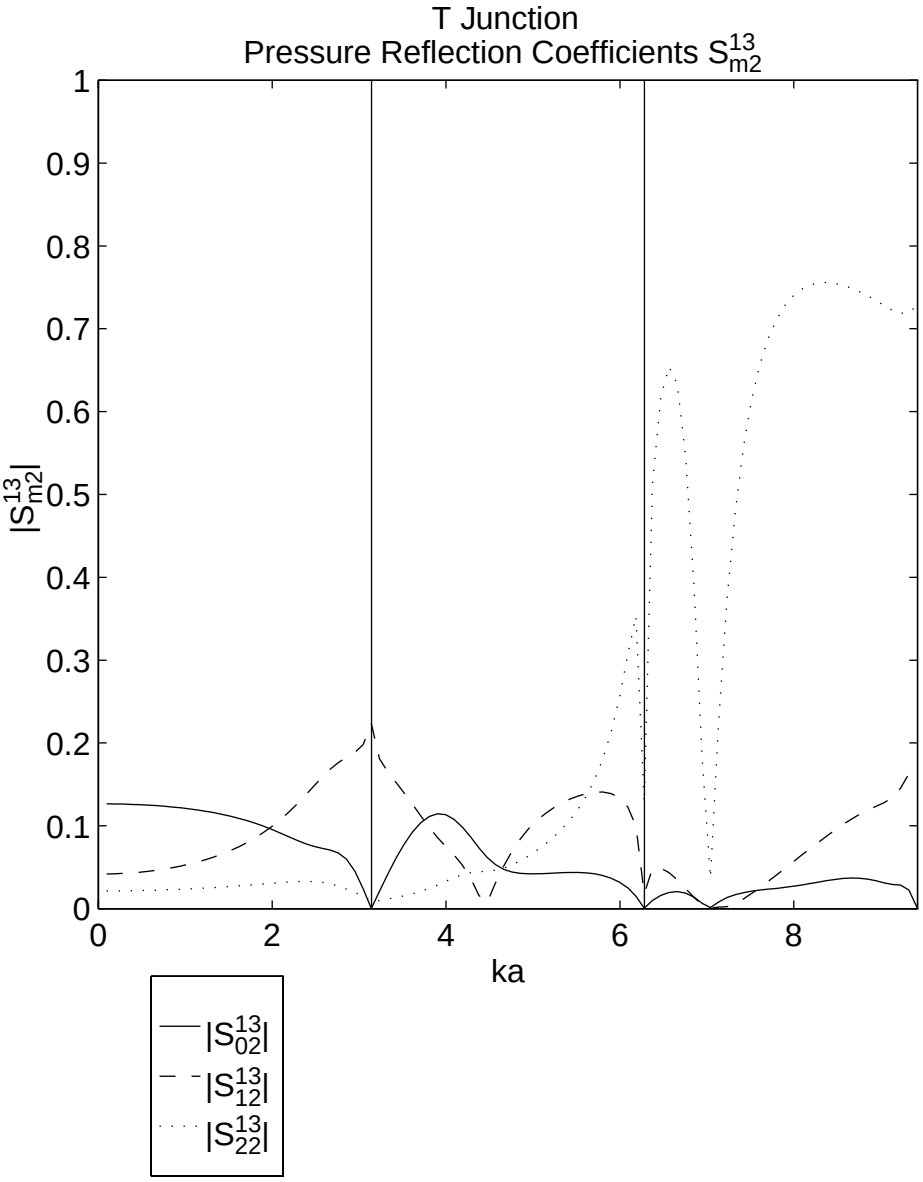

Fig. 4.24. Magnitude of the pressure transmission coefficients S^{13}_{m2}, from mode 2 in one end of a T to modes $m = 0, 1, 2$ in the other end.

Chapter 5

Modal Scattering and Radiation at an Infinite Baffle

This chapter will develop expressions for the reflection coefficients at the end of a baffled duct and discuss the characteristics of the radiated pressure.

5.1 General Derivation of Radiation Impedance

Calculating the reflection coefficients at the end of a finite rectangular waveguide is a difficult, but important problem. Once the reflection coefficients are known, the velocity at the end of the duct is known, and the radiation from the duct can be computed. With a known velocity distribution, radiation from the end of a rectangular duct is very similar to radiation from a baffled rectangular plate. Since the radiation characteristics of baffled plates are known, the radiation characteristics of the baffled duct are known as well.

There are two basic approaches to determining the radiation of a vibrating region: use of the Kirchoff-Helmholtz integral theorem (direct integration of the differential equation) and wavenumber transform techniques. The solution that follows uses the Kirchoff-Helmholtz integral theorem in the form of the Rayleigh integral.

To solve the duct radiation problem, assume a semi-infinite duct terminating in an infinite baffle at the plane $z = 0$ as shown in figure 5.1. In the duct (for $z < 0$) the pressure and velocity in the z direction can be expressed as modal expansions. Using

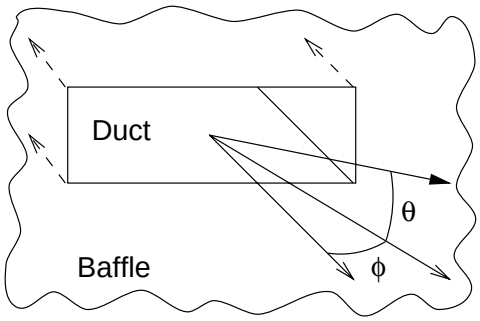

Fig. 5.1. Geometry used in calculating reflection and radiation from a baffled duct.

the notation in chapter 2

$$p(x,y,z) = \sum_M (A_M e^{-\gamma_M z} + B_M e^{\gamma_M z})\psi_M(x,y) \tag{5.1}$$

and

$$u_z(x,y,z) = \sum_M Y_M (A_M e^{-\gamma_M z} - B_M e^{\gamma_M z})\psi_M(x,y). \tag{5.2}$$

Since there is no field incident on the duct junction from the free space side, B_M must be directly related to A_M and can be written as

$$B_M = \sum_N R_{MN} A_N. \tag{5.3}$$

Using equation 5.3, equations 5.1 and 5.2 can be rewritten as

$$p(x,y,z) = \sum_M (A_M e^{-\gamma_M} + \sum_N R_{MN} A_N e^{\gamma_M z})\psi_M(x,y) \tag{5.4}$$

and

$$u_z(x,y,z) = \sum_M Y_M(A_M e^{-\gamma_M z} - \sum_N R_{MN} A_N e^{\gamma_M z})\psi_M(x,y). \tag{5.5}$$

For a baffled duct, the velocity on the baffle is zero and the pressure can be determined by using the Rayleigh integral as described in chapter 2. Using the Green's function for a baffled radiator, and given the normal velocity u_z at $z = 0$, the pressure outside the duct will be

$$p(x,y,z) = \frac{jk\rho c}{2\pi} \iint_{\mathcal{S}} u_z(x_0,y_0)\frac{e^{-jkr}}{r} d\mathcal{S} \tag{5.6}$$

where $r = \sqrt{(x-x_0)^2 + (y-y_0)^2 + z^2}$ and $\mathcal{S}$ is the area of the duct.

At the baffle, the pressure p and normal velocity u_z are continuous across the interface. Inserting equations 5.4 and 5.5 into equation 5.6 yields

$$\begin{aligned} \sum_M (A_M + \sum_N R_{MN} A_N)\psi_M(x,y) &= \frac{jk\rho c}{2\pi} \sum_M Y_M (A_M - \sum_N R_{MN} A_N) \\ &\quad \times \int_0^a \int_0^b \psi_M(x_0,y_0)\frac{e^{-jkr}}{r} dx_0 dy_0 \end{aligned} \tag{5.7}$$

where

$$r = \sqrt{(x-x_0)^2 + (y-y_0)^2}. \tag{5.8}$$

Multiplying equation 5.7 by ψ_R and integrating across the duct cross section will eliminate the sum on the left hand side of the equation because of orthogonality of the

modes. Equation 5.7 then reduces to

$$(A_R + \sum_N R_{RN} A_N) = \sum_M Z_{rRM} Y_M (A_M - \sum_N R_{MN} A_N) \tag{5.9}$$

where the complex mutual modal radiation impedance Z_{rRM} is

$$Z_{rRM} = \frac{jk\rho c}{2\pi} \iint_S \iint_S \psi_R(x,y)\psi_M(x_0,y_0)\frac{e^{-jkr}}{r} dx_0 dy_0 dx dy. \tag{5.10}$$

Appendix B has a derivation of an alternate form of Z_{rRM} which requires only two integrations instead of four.

Notice that equation 5.9 has Z_{rRM} multiplied by Y_M. Since Y_M is the characteristic modal admittance, multiplication by Y_M is normalization to the characteristic modal impedance. Thus, it makes sense to define the normalized mutual modal radiation impedance ζ_{RM} as

$$\zeta_{RM} = Z_{rRM} Y_M. \tag{5.11}$$

Because of reciprocity the Green's function is symmetric with respect to $\vec{x}$ and $\vec{x_0}$ and so $Z_{rRM} = Z_{rMR}$. However, $\zeta_{RM} \neq \zeta_{MR}$ because $Y_R \neq Y_M$.

It is also interesting to note that Z_{rRM} can also be identified as a scaled modal coefficient in a modal decomposition of e^{-jkr}/r. The integral in equation 5.10 is the same one required when doing a modal decomposition of the infinite baffle Green's function.

5.2 Development of Matrix Equations

Using the matrices developed in chapter 2 and defining two new ones, one can eliminate A_M and A_R from equation 5.9 and solve for the reflection coefficients R_{RM}.

If one defines the matrices

$$\bar{Z}_r = \begin{bmatrix} Z_{r00} & Z_{r01} & \cdots \\ Z_{r10} & Z_{r11} & \cdots \\ \vdots & \vdots & \vdots \end{bmatrix} \quad \bar{\zeta} = \begin{bmatrix} \zeta_{00} & \zeta_{01} & \cdots \\ \zeta_{10} & \zeta_{11} & \cdots \\ \vdots & \vdots & \vdots \end{bmatrix} \tag{5.12}$$

equation 5.9 can be rewritten

$$(\bar{I} + \bar{R})\bar{A} = \bar{Z}_r\bar{Y}(\bar{I} - \bar{R})\bar{A} = \bar{\zeta}(\bar{I} - \bar{R})\bar{A} \tag{5.13}$$

from which $\bar{R}$ is found to be

$$\bar{R} = (\bar{Z}_r\bar{Y} + \bar{I})^{-1}(\bar{Z}_r\bar{Y} - \bar{I}) = (\bar{\zeta} + \bar{I})^{-1}(\bar{\zeta} - \bar{I}). \tag{5.14}$$

Once again it can be seen that in matrix form the equation for the reflection coefficients takes the standard form of an impedance discontinuity.

5.3 Z_{rRM} for a Rectangular Duct

For a rectangular duct equation 5.10 becomes

$$Z_{rRM} = \frac{jk\rho c}{2\pi} \int_0^a \int_0^b \int_0^a \int_0^b \frac{\cos(\frac{r_x\pi}{a}x)}{\sqrt{a\Lambda_{r_x}}} \frac{\cos(\frac{r_y\pi}{b}y)}{\sqrt{b\Lambda_{r_y}}} \frac{\cos(\frac{m_x\pi}{a}x_0)}{\sqrt{a\Lambda_{m_x}}} \frac{\cos(\frac{m_y\pi}{b}y_0)}{\sqrt{b\Lambda_{m_y}}} \frac{e^{-jkr}}{r} dx_0 dy_0 dx dy. \tag{5.15}$$

Equation 5.15 is one of the forms of equation 5.10 to which there is no analytical solution.

The most straightforward (albeit time consuming) way to evaluate Z_{rRM} is to compute the four dimensional integral itself. The transformation shown in Appendix B is not easier to compute numerically. Appendix C discusses the technique used to numerically integrate equation 5.15.

One of the first things to notice is that because of the symmetry of the problem (and hence the Green's function) all the coupling terms between even and odd numbered modes are zero (i.e $Z_{r01}, Z_{r10}, Z_{r12}, Z_{r21}$ are all zero). This means that there is no coupling between even and odd modes.

ζ_{RM} was evaluated for $r_x = 0, 1, 2$, $r_y = 0$, $m_x = 0, 1, 2$, $m_y = 0$ and $a/b = 2.25$. The ratio of a/b corresponds to that of the duct used in the experimental investigations.

Figure 5.2 shows the real part of the normalized self modal radiation impedances ζ_{00}, ζ_{11}, and ζ_{22}. For each mode, the self-resistance is zero at the cut-off frequency of the mode and rises quickly toward unity above the cut-off frequency. A radiation resistance close to unity means that very little energy is reflected back into that mode. It is either reflected back into another mode or is radiated out the end of the duct.

Figure 5.3 shows the imaginary part of the normalized self modal radiation impedances ζ_{00}, ζ_{11}, and ζ_{22}. For each mode, the self reactance is zero at the cut-off frequency, quickly rises to a value near 0.5 close to the cut-off frequency of the next mode and then drops back toward zero at higher frequencies. Below the cut-off frequency the reactance is small, but only values above the cut-off frequency are significant since only modes above their cut-off frequency propagate energy toward the end of the duct. The radiation reactance is a measure of the energy stored in the near field of the end of the duct.

Figure 5.5 shows the real part of the mutual modal radiation impedances ζ_{20} and ζ_{02}. The mutual resistance for the (02) mode is positive below the cut-off frequency and negative above. The mutual resistance for the (20) mode is negative for all frequencies.

Figure 5.5 shows the imaginary part of the mutual modal radiation impedance ζ_{20} and ζ_{02}. The mutual reactance for the (02) mode and the (20) mode are similar, negative below the cut-off frequency and positive above the cut-off frequency of the second mode.

While the physical interpretation of these values is not clear, it is clear that the (02) coupling is different from the (20) coupling. Because the impedances are non-zero it is also clear that both propagating energy and evanescent energy (energy stored in the near field) are being exchanged between the modes. Since the amplitudes of the mutual radiation impedance are not negligible compared to the self radiation impedances, modal coupling at the end of the duct should not be ignored at frequencies near or above the cut-off frequency of the mode.

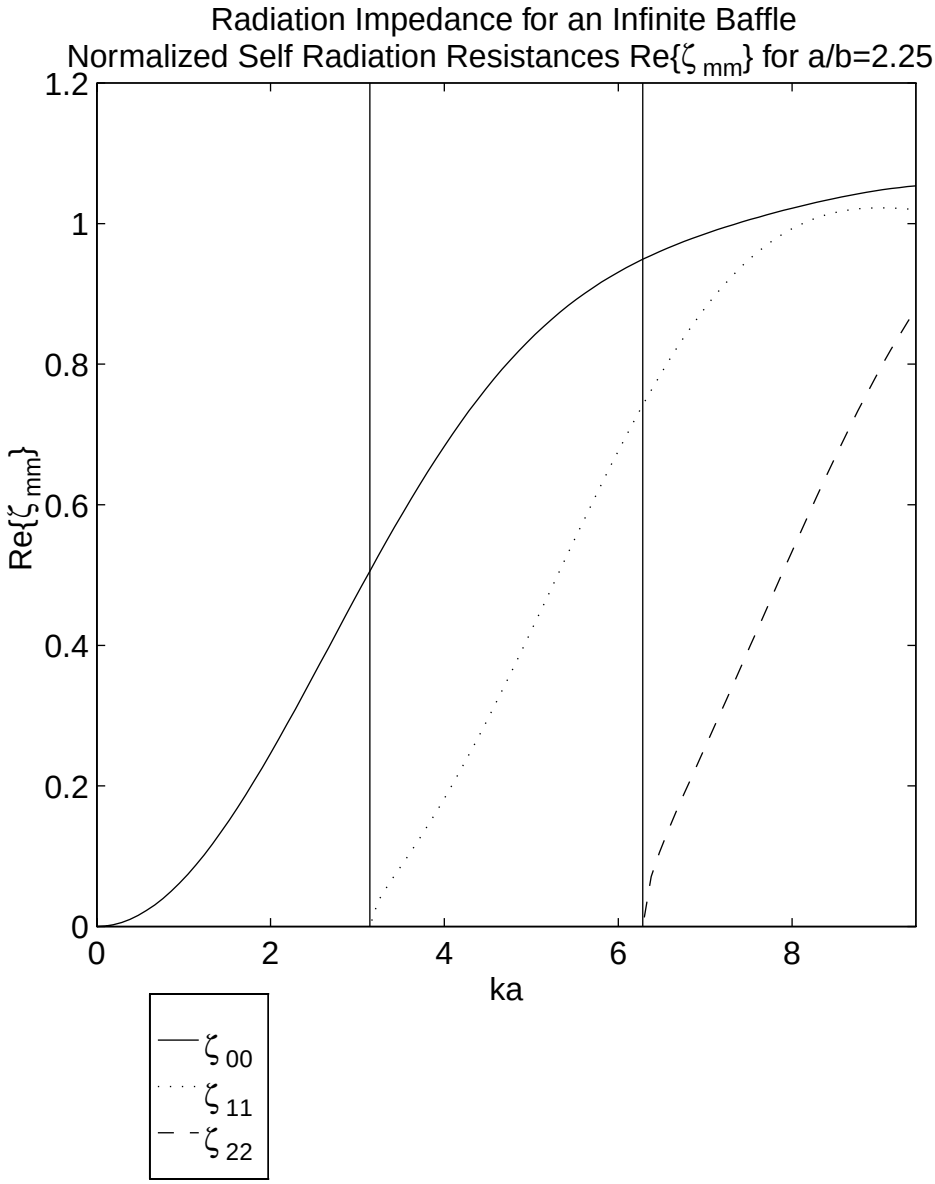

Fig. 5.2. Normalized self radiation resistances of an infinite baffle, $\mathrm{Re}\{\zeta_{mm}\}$, for $m = 0, 1, 2$, with $a/b = 2.25$.

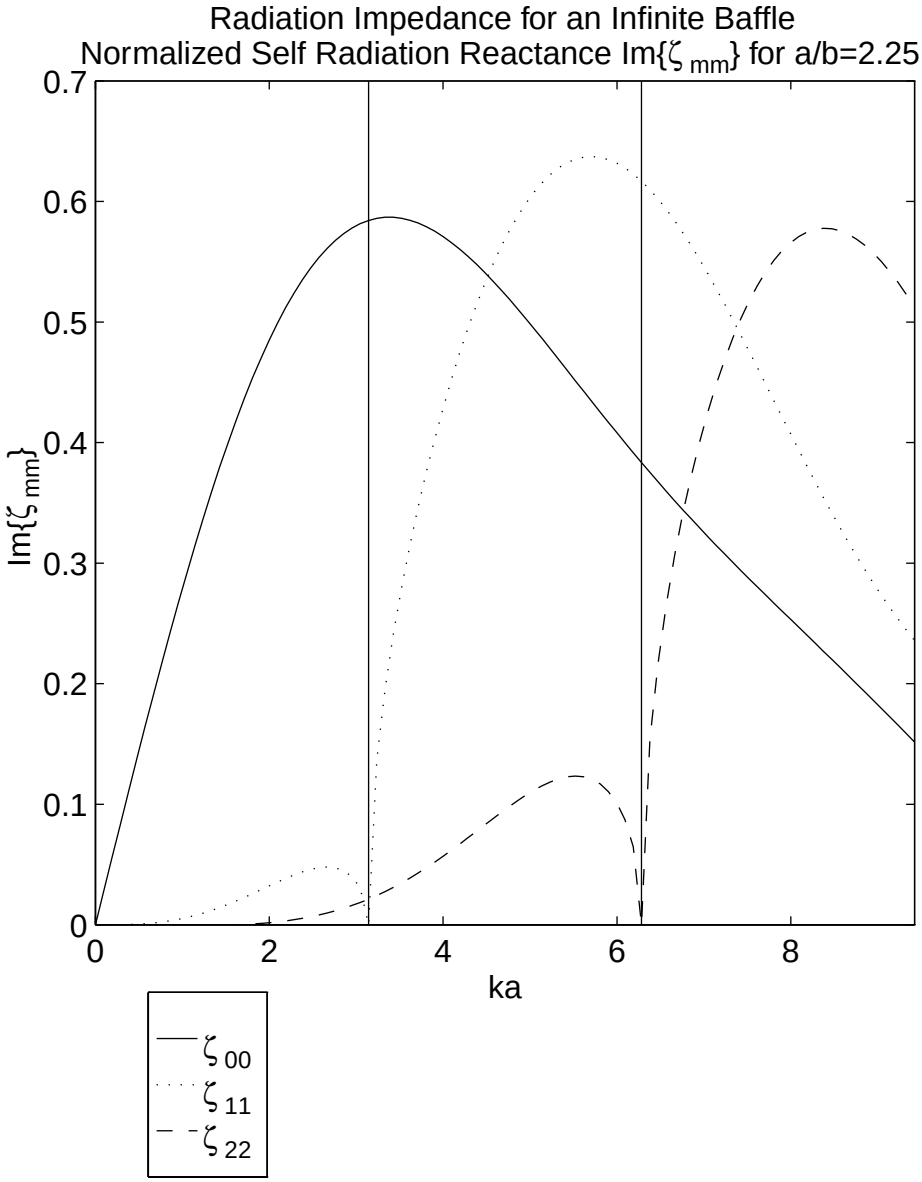

Fig. 5.3. Normalized self radiation reactances of an infinite baffle, $\mathrm{Im}\{\zeta_{mm}\}$, for $m = 0, 1, 2$ with $a/b = 2.25$.

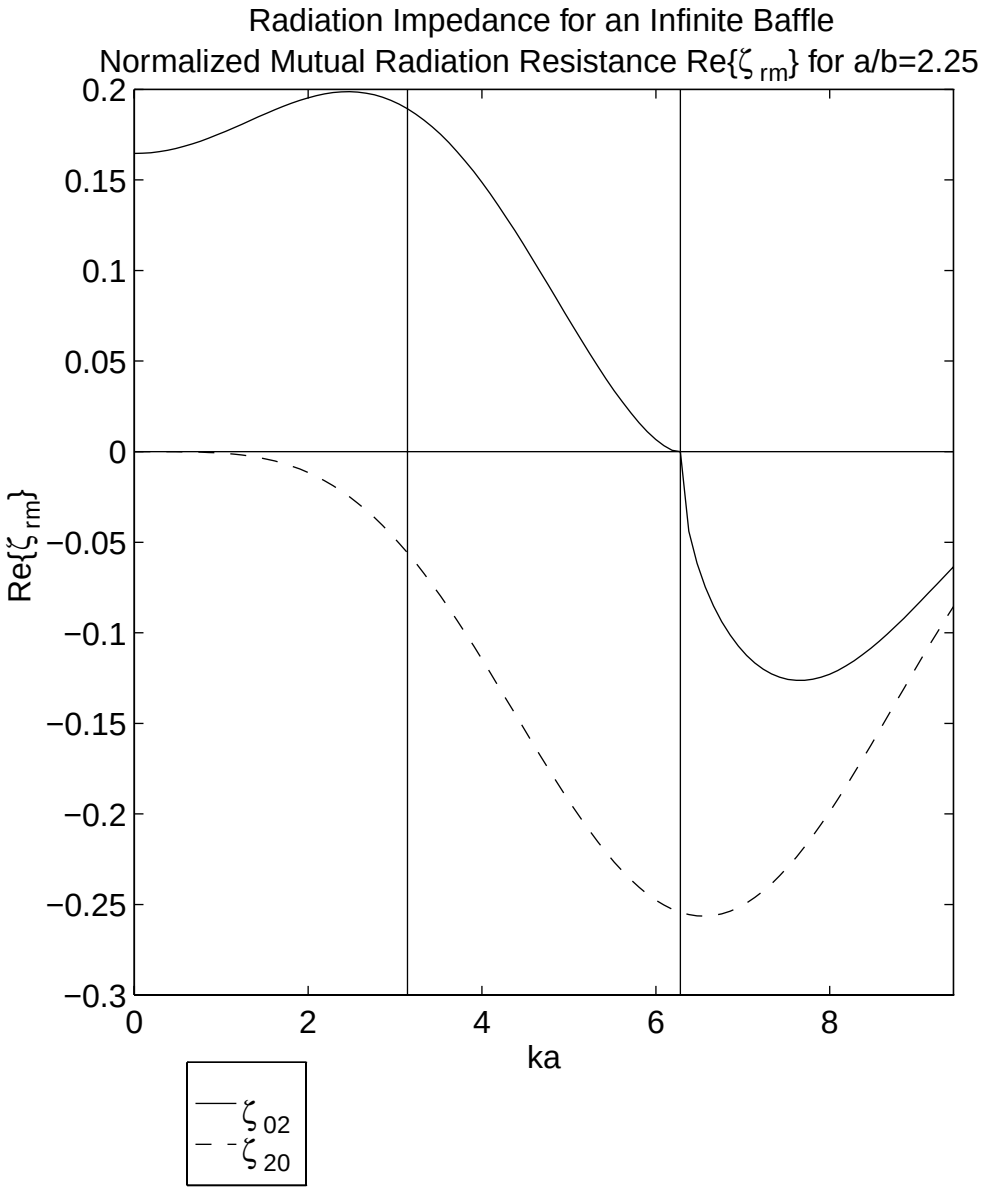

Fig. 5.4. Normalized mutual radiation resistances of an infinite baffle, $\mathrm{Re}\{\zeta_{rm}\}$ and $\mathrm{Im}\{\zeta_{rm}\}$, for $m = 0, 1, 2$ with $a/b = 2.25$.

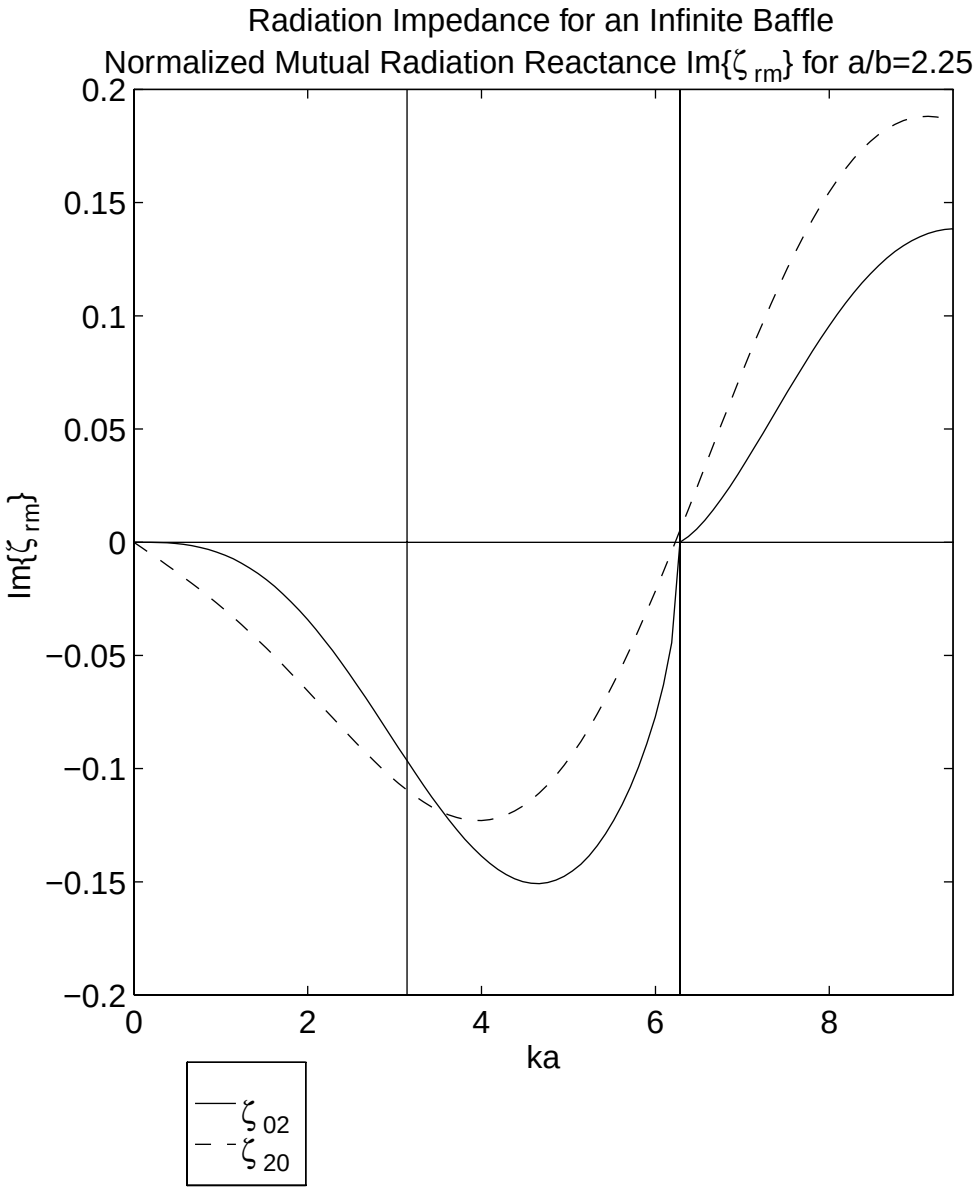

Fig. 5.5. Normalized mutual radiation reactances of an infinite baffle, $\mathrm{Re}\{\zeta_{rm}\}$ and $\mathrm{Im}\{\zeta_{rm}\}$, for $m = 0, 1, 2$ with $a/b = 2.25$.

5.4 Reflection Coefficients

Having computed ζ_{RM}, the reflection coefficients can be easily evaluated from equation 5.14.

Figure 5.6 shows the absolute value of the self modal reflection coefficients for an infinite duct with $a/b = 2.25$. The self reflection coefficients are unity at the cut-off frequency and decay to zero with increasing frequency.

Figure 5.7 shows the phase of the self modal reflection coefficients for an infinite duct with $a/b = 2.25$. The phase of the self reflection coefficients are π at the cut-off frequency of the mode. So, at the cut-off frequency of the mode, the infinite baffle termination looks like a pressure release surface to that mode. The phase of R_{00} decreases to about $\pi/2$ at the cut-off frequency of the first mode and begins to decrease again above the cut-off frequency of the second mode. The phase of the first mode decreases to about $\pi/2$ near the cut-off frequency of the second mode.

Figure 5.8 shows the absolute value of the mutual modal pressure reflection coefficients for an infinite duct with $a/b = 2.25$. The absolute value of R_{00} is plotted for comparison. The first thing to note is that at the cut-off frequency $|R_{02}| = 0$ but $|R_{20}| \neq 0$. This means that the second mode does not couple into the plane wave mode at its cut-off frequency, but the plane wave mode does couple into the second mode. The values of the coefficients below the cut-off frequency are not very important as the higher mode does not propagate. The second thing to note is that $|R_{20}|$ is greater than $|R_{00}|$ above the cutoff frequency, so at higher frequencies more of the plane wave mode is reflected into the second mode than the plane wave mode. Obviously the coupling

effects of the plane wave mode into propagating higher order modes are not negligible in any way.

Figure 5.9 shows the phase of the mutual modal pressure reflection coefficients for an infinite duct with $a/b = 2.25$. The phase of R_{02} and R_{20} differ by $\pi/2$ until the cut-off frequency of the mode when it begins to decrease. Above the cut-off frequency of the second mode the phase of the two is the same.

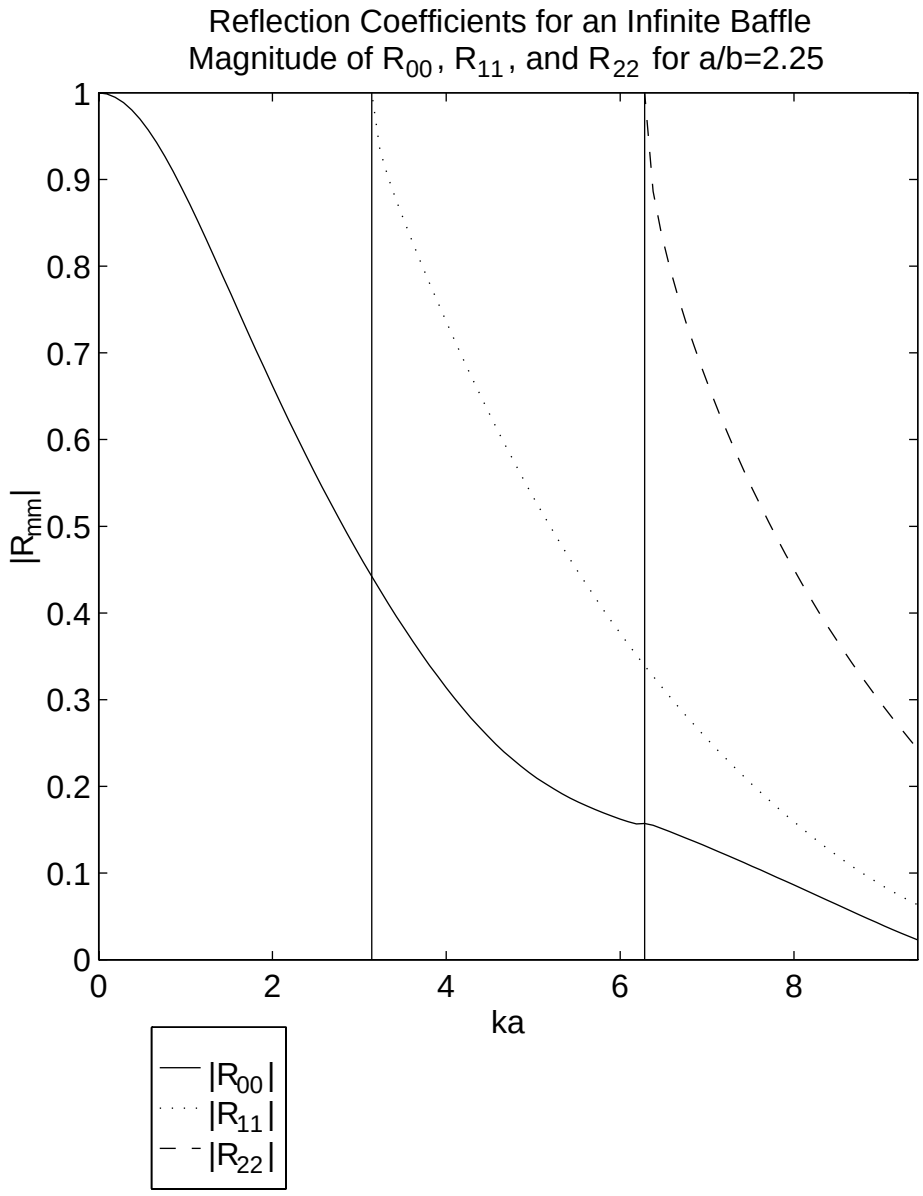

Fig. 5.6. Magnitude of the self pressure reflection coefficients of an infinite baffle, R_{mm}, for $m = 0, 1, 2$ with $a/b = 2.25$.

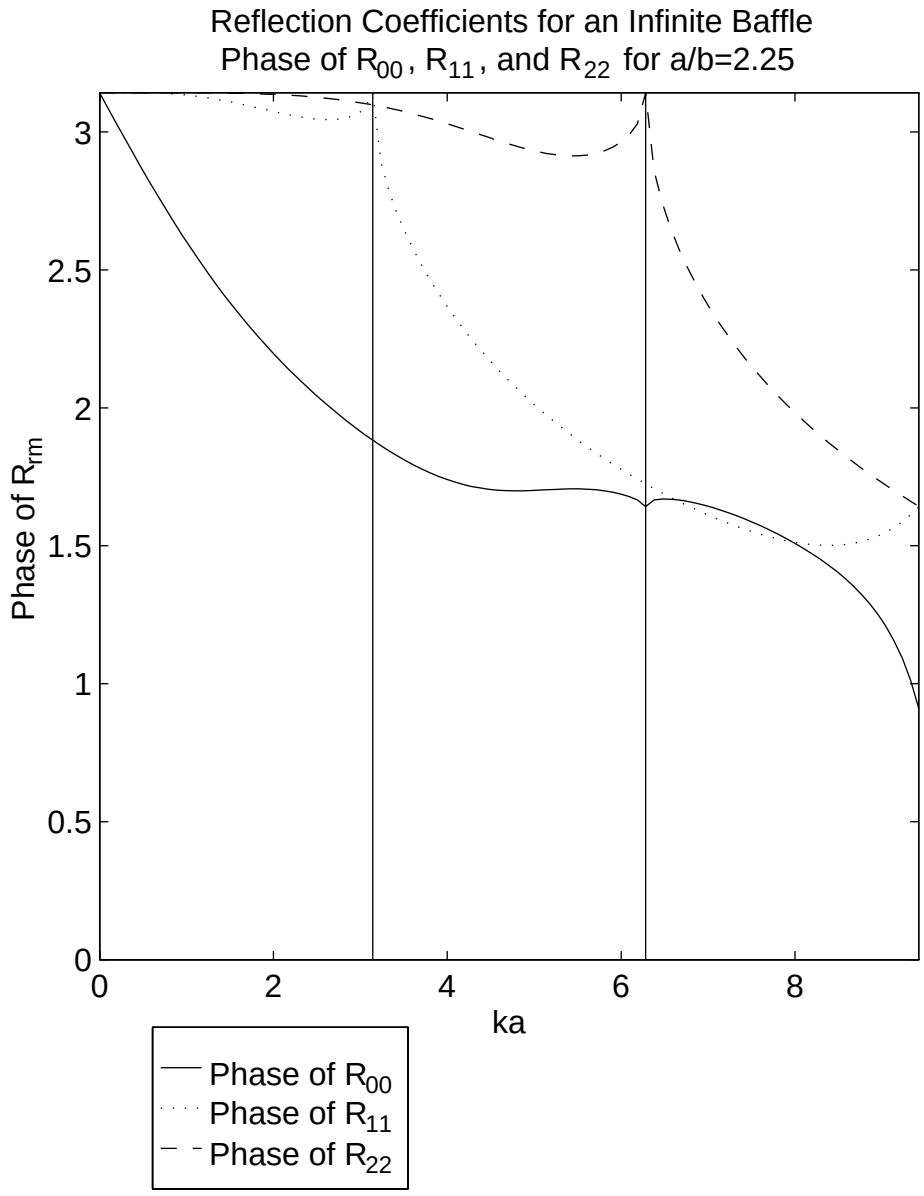

Fig. 5.7. Phase of the self pressure reflection coefficients of an infinite baffle, R_{mm}, for $m = 0, 1, 2$ with $a/b = 2.25$.

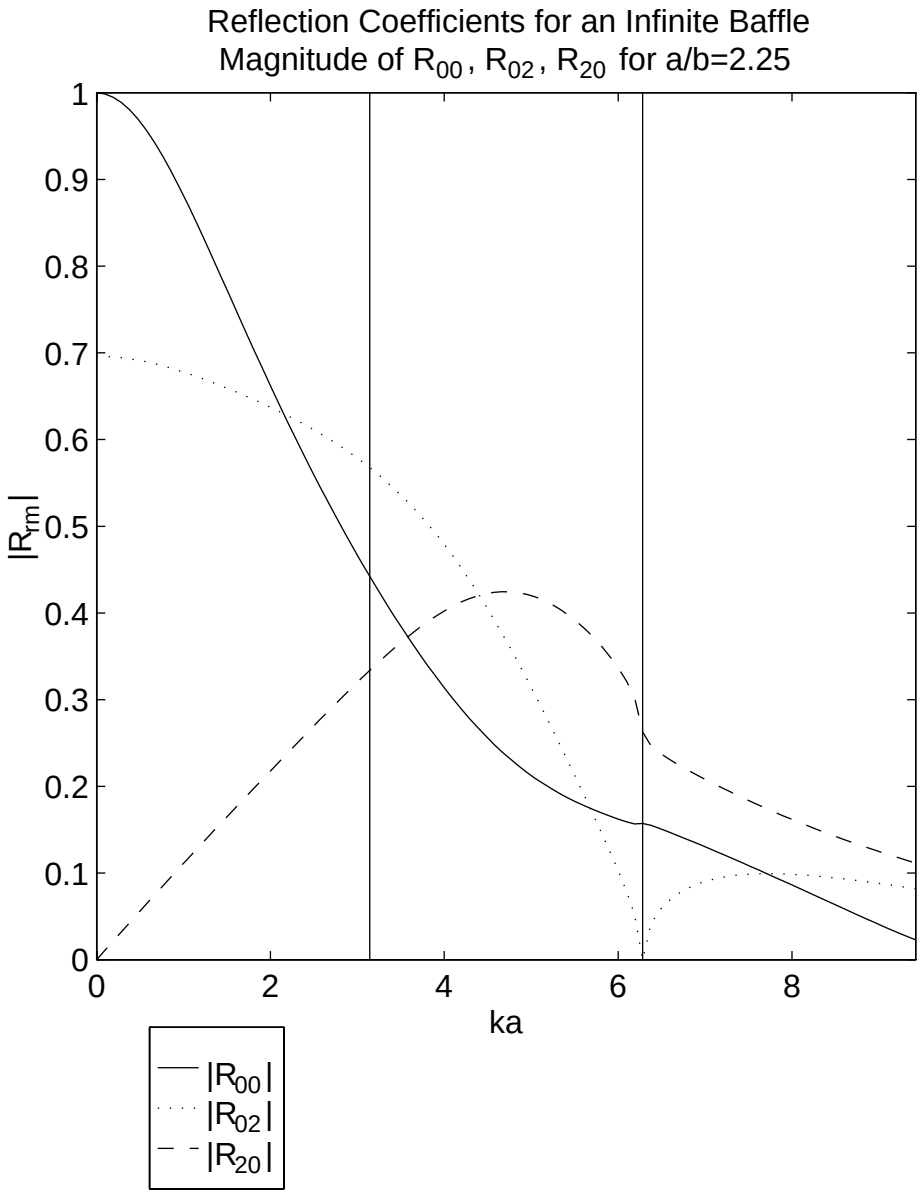

Fig. 5.8. Magnitude of the mutual pressure reflection coefficients R_{02} and R_{20} of an infinite baffle for $m = 0, 1, 2$, with $a/b = 2.25$. $|R_{00}|$ is shown for comparison.

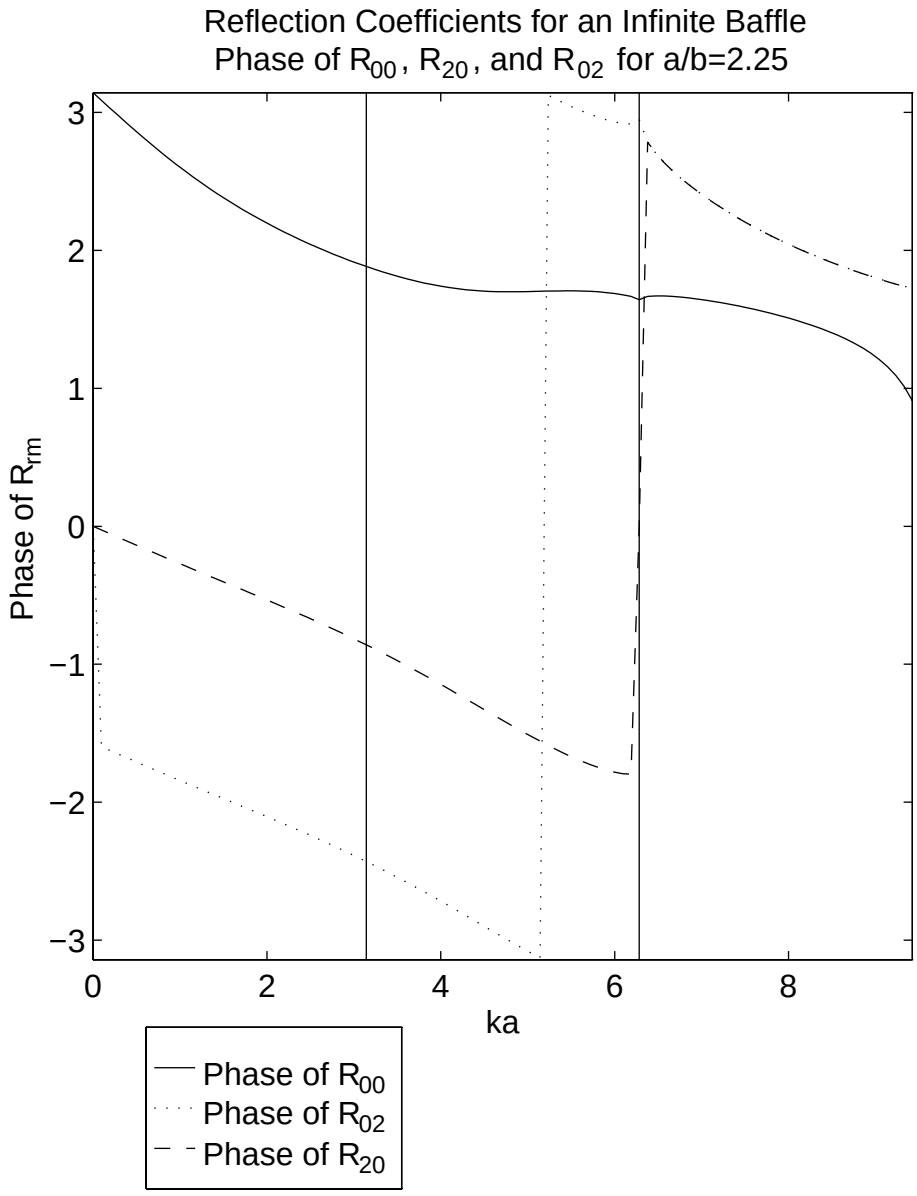

Fig. 5.9. Phase of the mutual reflection coefficients R_{02} and R_{20} of an infinite baffle for $m = 0, 1, 2$, with $a/b = 2.25$. The phase of R_{00} is shown for comparison.

5.5 Radiation

5.5.1 Directivity

Having determined the reflection coefficients R_{RM}, the velocity at the interface is completely determined. Given the velocity distribution, the pressure at any point outside the duct can be determined by use of the Rayleigh integral.

The pressure directivity and the radiated power of each particular mode are very useful in determining the radiation outside the duct given a mode incident at the end of the duct.

The velocity at the end of the duct is

$$u_z = \sum_M Y_M (A_M - \sum_N R_{MN} A_N) \phi_M. \tag{5.16}$$

The pressure outside the duct, for any position $\vec{R}$ is given by the Rayleigh integral

$$p(x,y,z) = \frac{\gamma_M}{2\pi} \sum_M Y_M (A_M - \sum_N R_{MN} A_N) \iint_{\mathcal{S}_0} \psi_M(x_0, y_0) \frac{e^{jkR}}{R} dx_0 dy_0. \tag{5.17}$$

where $R = \sqrt{(x-x_0)^2 + (y-y_0)^2 + z^2}$.

Even if only one mode is incident, there can be many modes reflected, so regardless of the incident wave there is a superposition of many modes. However, to better understand the physics of the problem one can consider the radiation of a single mode.

The pressure will then have the form

$$p_M(x,y,z) = C_M \iint_{\mathcal{S}_0} \psi_M(x_0,y_0)\frac{e^{jkR}}{R}dx_0dy_0. \tag{5.18}$$

where $C_M = jk\rho c/(2\pi)Y_M A_M(1-R_{MM})$ is the total modal amplitude of the mode M.

To determine the directivity pattern and radiated power, the pressure can be evaluated in the far field. The standard far field approximation is

$$R \approx r - x\sin(\theta)\cos(\phi) - y\sin(\theta)\sin(\phi) \tag{5.19}$$

where

$$r = \sqrt{x^2+y^2+z^2}. \tag{5.20}$$

With this approximation equation 5.18 becomes

$$p_M(x,y,z) = C_M\frac{e^{jkr}}{r}\iint_{\mathcal{S}_0} \psi(x_0,y_0)e^{-j(x\alpha+y\beta)}dx_0dy_0 \tag{5.21}$$

where $\alpha = k\sin(\theta)\cos(\phi)$ and $\beta = k\sin(\theta)\sin(\phi)$.

The integral can be recognized as a wavenumber transform of ψ (see appendix B) by replacing α and β with k_x and k_y. The far field equation can be then be written

$$p_M(r,\phi,\theta) = C_M\frac{e^{jkr}}{r}\Psi_M(\alpha,\beta). \tag{5.22}$$

For the purposes of this thesis, the directivity $D_M(\phi, \theta)$ is defined as the ratio of the magnitude of $\Psi_M(\alpha, \beta)$ divided by the maximum value of $\Psi_M(\alpha, \beta)$. With this definition $D_M(\phi, \theta)$ contains the angular dependence of p_M.

Figure 5.10 shows the directivity for the plane wave mode with $ka = 0.5\pi$, 1.5π, 2.5π, and 3.5π. Recall that the first higher order mode cut-off is at $ka = \pi$. Below the cut-off frequency of the first mode the radiation is pretty much omni-directional. Just above the cut-off frequency of the first mode beaming effects are clearly apparent. Above the cut-off frequency of the second mode lobing has begun.

Figure 5.11 shows the directivity for the first horizontal mode with $ka = 0.5\pi$, 1.5π, 2.5π, and 3.5π. In contrast to the plane wave mode, there is no radiation on axis; the radiation is beamed far off to the sides. Below the cut-off frequency for the mode the direction of maximum radiation is at $\pm 90^o$. At higher frequencies the radiation beams narrow and get closer to the axis. Secondary lobes are apparent above cut-off frequency of the third mode.

Figure 5.12 shows the directivity for the second horizontal mode with $ka = 0.5\pi$, 1.5π, 2.5π, 3.5π. Again, below the cut-off frequency of the mode the radiation maximum is at $\pm 90^o$. Again, above cut-off frequency of the mode the beams are directed more toward the main axis.

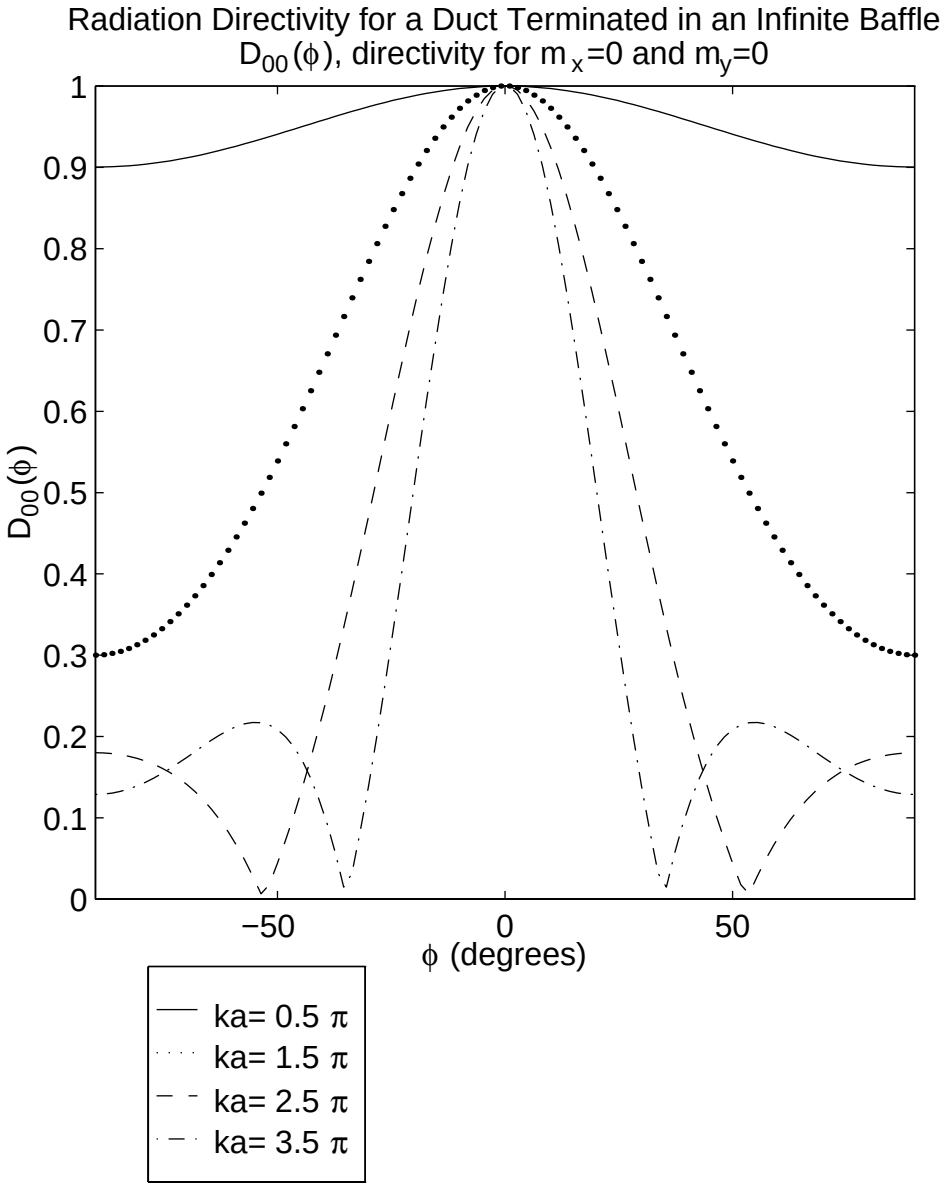

Fig. 5.10. $D_{00}(\phi)$, the directivity of the radiated pressure for a plane wave mode incident at an infinite baffled end with $\theta = 0$ and $a/b = 2.25$

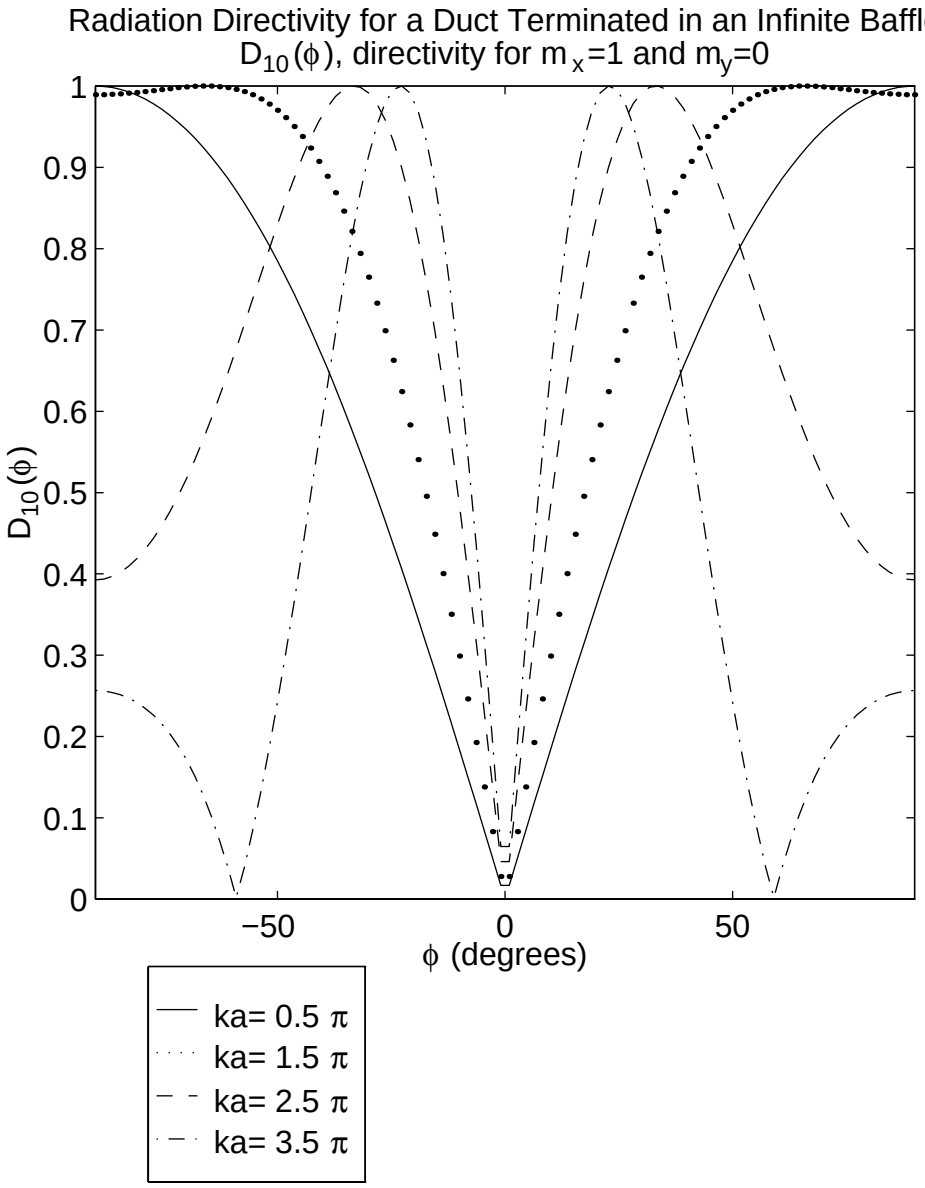

Fig. 5.11. $D_{10}(\phi)$, the directivity of the radiated pressure for the first horizontal mode incident at an infinite baffled end $\theta = 0$ and $a/b = 2.25$

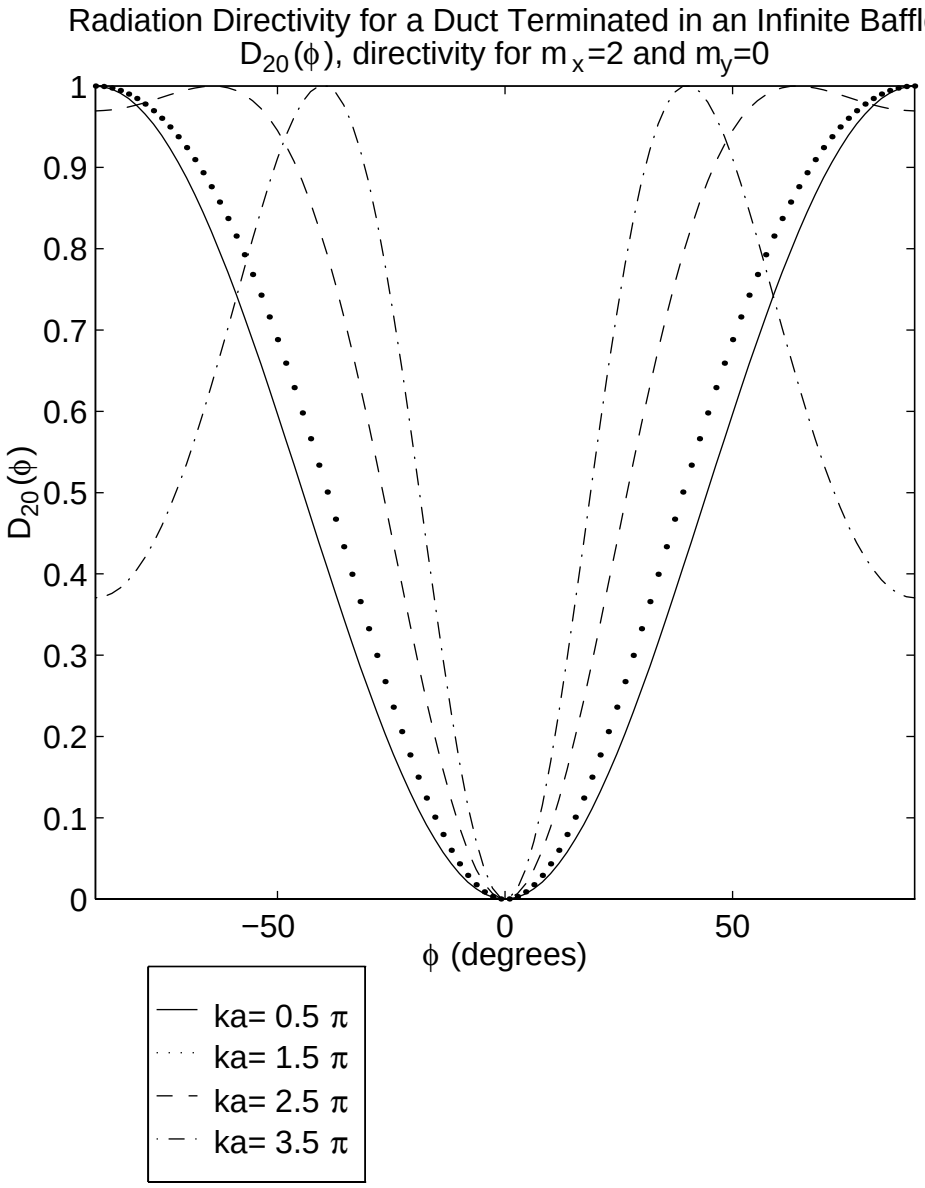

Fig. 5.12. $D_{20}(\phi)$, the directivity of the radiated pressure for the second horizontal mode wave mode incident at an infinite baffled end with $\theta = 0$ and $a/b = 2.25$

5.5.2 Radiated Power

The radiated power can be obtained by several methods. The power could be obtained by integrating the square of the far field pressure. As with radiation from rectangular panels [66], this would lead to more integrals which must be approximated or numerically evaluated. Alternatively, one could use the knowledge of the duct reflection coefficients to compute the radiated power.

The power in a single traveling mode of amplitude A_M is

$$\Pi_M = \frac{k_M}{2k\rho c}|A_M|^2. \tag{5.23}$$

From this the total power traveling toward the duct end is

$$\Pi_+ = \sum_M \frac{k_M}{2k\rho c}|A_M|^2 = \bar{A}^H \bar{Y} \bar{A} \tag{5.24}$$

where ^{H} denotes the hermitian operator which is the complex conjugate transpose.

The total power reflected back from the end of the duct is

$$\Pi_- = \bar{B}^H \bar{Y} \bar{B} = (\bar{R}\bar{A})^H \bar{Y} \bar{R} \bar{A} = \bar{A}^H \bar{R}^H \bar{Y} \bar{R} \bar{A}. \tag{5.25}$$

The difference between the incident and the reflected powers must be the radiated power because there are no losses. Thus the total radiated power is

$$\Pi_{Rad} = \bar{A}^H (\bar{Y} - \bar{R}^H \bar{Y} \bar{R}) \bar{A}. \tag{5.26}$$

Chapter 6

Experimental Results

This chapter will discuss the experimental measurements of the reflection coefficients of a baffled duct.

6.1 Modal Decomposition

In order to measure reflection coefficients, one must first determine the modal amplitudes A_M and B_M in the duct. Experimentally this is done by measuring the pressure at a number of discrete positions and determining A_M and B_M from those measurements.

In chapter 2 it was shown that the pressure could be written

$$p(x,y,z) = \sum_M (A_M e^{-\gamma_M z} + B_M e^{\gamma_M z})\psi_M(x,y). \tag{6.1}$$

Defining the modal pressure as

$$P_M(z) = (A_M e^{-\gamma_M z} + B_M e^{\gamma_M z}) \tag{6.2}$$

equation 6.1 can be rewritten in terms of modal pressures

$$p(x,y,z) = \sum_M P_M(z)\psi_M(x,y). \tag{6.3}$$

This equation shows that the pressure can be broken into a modal component which is $\hat{z}$ dependent and an eigenfunction which is $\hat{x}$ and $\hat{y}$ dependent.

Defining the matrices

$$\bar{p} = \begin{bmatrix} p(x_1, y_1, z_1) & p(x_1, y_1, z_2) & \cdots \\ p(x_2, y_2, z_1) & p(x_2, y_2, z_2) & \cdots \\ \vdots & \vdots & \ddots \end{bmatrix} \tag{6.4}$$

$$\bar{\psi} = \begin{bmatrix} \psi_0(x_1, y_1) & \psi_1(x_1, y_1) & \cdots \\ \psi_0(x_2, y_2) & \psi_1(x_2, y_2) & \cdots \\ \vdots & \vdots & \ddots \end{bmatrix} \tag{6.5}$$

and

$$\bar{P}_M = \begin{bmatrix} P_0(z_1) & P_0(z_2) & \cdots \\ P_1(z_1) & P_1(z_2) & \cdots \\ \vdots & \vdots & \ddots \end{bmatrix} \tag{6.6}$$

a collection of pressure measurements can be written as

$$\bar{p} = \bar{\psi}\bar{P}_M \tag{6.7}$$

and the modal pressure can be found from a collection of pressure measurements by the equation

$$\bar{P}_M = \bar{\psi}^{-1}\bar{p}. \tag{6.8}$$

To be able to uniquely determine $\bar{P}_M$ requires that $\bar{\psi}$ have a generalized inverse which means that, among other things, the columns of $\bar{\psi}$ must be linearly independent. This limits the $\hat{x}$ and $\hat{y}$ positions of the measurements. In addition, to discern $\mathcal{N}$ modes $\bar{p}$ and $\bar{\psi}$ must have at least $\mathcal{N}$ rows. If they have more than $\mathcal{N}$ rows a least squares solution is obtained.

Once the $Pbar_M$ are found A_M and B_M are easily determined.

Defining the matrices

$$\bar{P}_{MZ} = \begin{bmatrix} P_M(z_1) \\ P_M(z_2) \\ \vdots \end{bmatrix} \quad \bar{\phi}_M = \begin{bmatrix} e^{-\gamma_M z_1} & e^{\gamma_M z_1} \\ e^{-\gamma_M z_2} & e^{\gamma_M z_2} \\ \vdots & \vdots \end{bmatrix} \tag{6.9}$$

the P_M and hence A_M and B_M can be found since $\bar{P}_{MZ}$ can be expressed as

$$\bar{P}_{MZ} = \bar{\phi} \begin{bmatrix} A_M \\ B_M \end{bmatrix} \tag{6.10}$$

Then A_M and B_M can be expressed as

$$\begin{bmatrix} A_M \\ B_M \end{bmatrix} = \bar{\phi}_M^{-1} \, \bar{P}_{MZ} \tag{6.11}$$

where $\bar{\phi}_M^{-1}$ is the generalized inverse of $\bar{\phi}_M$.

From equation 6.11 one can see that as a minimum at least measurements at at least 2 different $\hat{z}$ positions and $\mathcal{N}$ different $\hat{x}, \hat{y}$ positions are required to determine A_M and B_M for $\mathcal{N}$ modes.

6.1.1 Probes vs. Arrays

Since pressures must be measured at several positions the use of microphone arrays or microphone probes immediately suggest themselves. Early experimental work relied on movable microphone probes for measurements. However, with the advent of small electret microphones, microphone arrays are now practical for use in modal measurements.

When using a single microphone or microphone probe, the problem of matching the microphones does not exist since there is only one microphone. However, because the microphone must be moved to many positions the technique is very time consuming and fraught with positioning errors.

If an array of microphones is used, positioning problems are either eliminated or reduced; however, microphone calibration and matching must now be considered. Because of the complexity of the electronics and calibration, the use of a full two dimensional array of microphones is also fraught with difficulties.

As a compromise between the microphone probe and two dimensional array, a linear array of microphones could be used. Either a horizontal array which is traversed along the duct length or an axial array which is traversed across the duct width could be used. In either case, there is less positioning error than with the single microphone

probe and a considerable speed up of the measurement process, while there is less calibration and phase matching problems and less electronics complexity than with a full two dimensional array. For these reasons a linear array was used for the measurements in this thesis.

6.1.2 Horizontal vs. Axial Arrays

Once a researcher has decided to use linear arrays, she or he must then choose between a horizontal or axial array configuration. Looking at the phase characteristics of the measurements in both directions will help determine the limitations of both types of measurements.

In the axial direction the pressure varies according to the term $e^{-\gamma_M z}$. The phase in the axial direction is position and frequency dependent. Even small phase errors in the measurements will lead to poor calculations of $\bar{A}$ and $\bar{B}$.

In the horizontal direction the pressure varies according to the term $\psi_M(x)$ which is not frequency dependent and has only a plus or minus phase. Phase errors are less likely to be a problem in the horizontal direction.

The microphones and electronics have small phase differences from channel to channel that are difficult to eliminate. If accurate axial placement is easier than accurate horizontal placement, mounting the microphones in a horizontal array and accurately positioning it axially should provide a better measurement than an axial array since the same microphone is used to sample the axial direction, thus eliminating electronic and microphone phase differences from the axial measurements and only positioning errors exist.

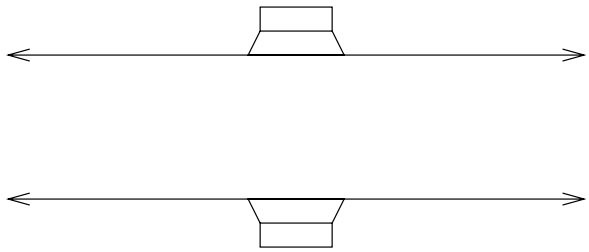

Fig. 6.1. Side mounted speaker configuration

For the duct used in the experimental work of this thesis it was much easier to accurately position the microphones axially than horizontally, so a horizontal array was used.

6.2 Modal Generation

Modal generation is a problem which has already been thoroughly researched [3, 18, 19]. The usual technique is to have a number of sources mounted on the outside walls of the duct as shown in figure 6.1. The problem with this configuration is that the amplitude of the modes generated goes as $\mathrm{sinc}(ka)$ where a is the radius of the speaker. Thus at some frequencies a given mode cannot be generated. In contrast, by placing the sources at the end of the duct as shown in figure 6.2 the modal coupling and generation is not frequency dependent (assuming the mode is not cut-off).

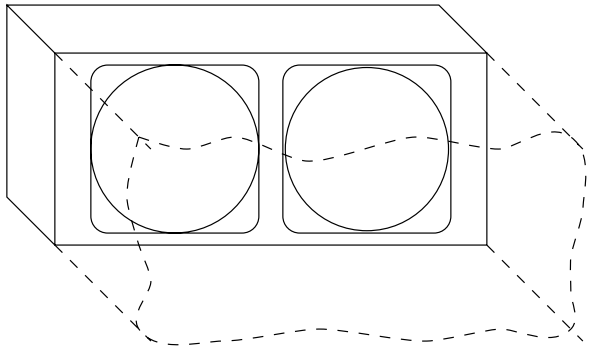

Fig. 6.2. Back mounted speaker configuration

6.3 Experimental Apparatus

The experiments were carried out in a duct 22.8 cm horizontally by 10 cm vertically (about 9 in x 4 in) by 192 cm long as shown in figure 6.3 . The dimensions were chosen so two horizontal modes could propagate before the first vertical mode was above its cut-off frequency. The duct was made of 3/4 inch thick density particle board. Because of the small dimensions of the duct, the walls were very rigid. The walls of the duct were not felt to move at any time during the experiment thus the assumption of rigid walls was made. The cut-off frequencies of the first and second cross modes were found experimentally to be 756 Hz and 1513 Hz. For the 25 ^{o}C room the theoretical frequencies are 756.5 Hz and 1513 Hz. Since the theoretical and experimental cut-off frequencies agree damping is negligible and the assumption of rigid walls is valid.

The array consisted of four 1/4 inch microphones placed at positions of $x = 0.005$ m, $x = 0.044$ m, $x = 0.079$ m and $x = 0.143$ m fixed in a wire mount as shown in

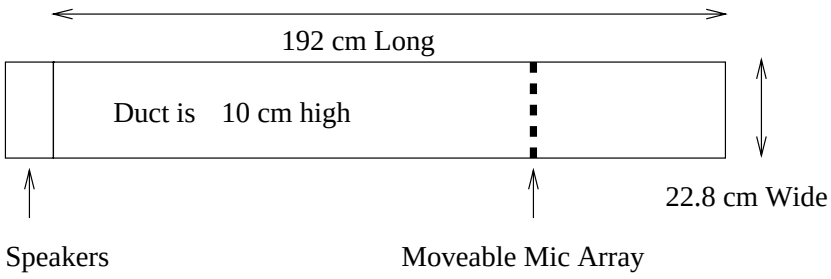

Fig. 6.3. Duct Setup

figure 6.4. The spacing resulted from attempting to place one microphone as close to the wall as possible, one microphone at the horizontal midpoint and the other two at the one third and one fourth points. The small size of the microphones and wire mount ensured that the acoustic field was disturbed very little by the measurement devices. The microphones were placed at a vertical height of $y = 5$ cm, the vertical mid line of the duct. By placing the microphones at that height, only the vertical plane wave and odd order modes would be measured - the first vertical mode would not be measured. The wire mount was attached to a 3/4 in steel tape measure which was used to move the microphone array and measure its axial position.

The microphones were Panasonic W63AT electret microphones which have a frequency response of ± 3 dB from 20 Hz to 20 kHz. A microphone preamplifier with four identical channels was specially designed for use with the Panasonic electret elements. The amplifier has level adjustments for each individual microphone. The bias resistors for the microphones were individually chosen for each microphone element. With optimal bias resistors, the harmonic distortion was as low as a B&K 4130 reference microphone.

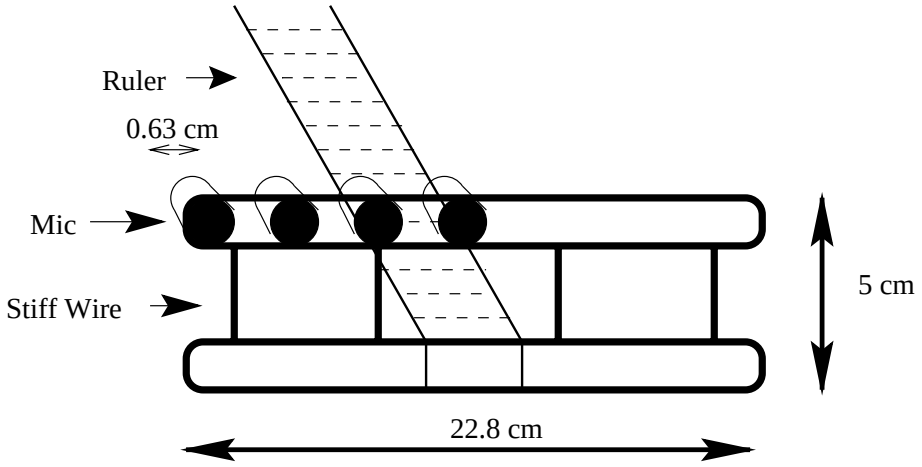

Fig. 6.4. Microphone Array Setup

With different values for the bias resistors, the overall gain of the microphone/amplifier cascade was different between channels, but the difference was removed by the use of the individual level controls on the preamplifier. The phase difference between elements was nominally $\pm 1^o$.

The acoustic source consisted of two 4 inch VIFA loudspeakers end mounted at one end of the duct as shown in figure 6.2. The speakers had a reasonably flat frequency response from 300 Hz to 4000 Hz. Three different modal configurations can be generated by having both speakers in phase (generating mostly plane waves), the two speakers out of phase (generating mostly the first horizontal mode), one speaker being on and one being off (generating both plane waves and the first horizontal mode).

The data was digitized by a Hewlett Packard HP 3566A Signal Analyzer. The HP 3566A can take both FFT and swept sine measurements and allows for auto ranging of

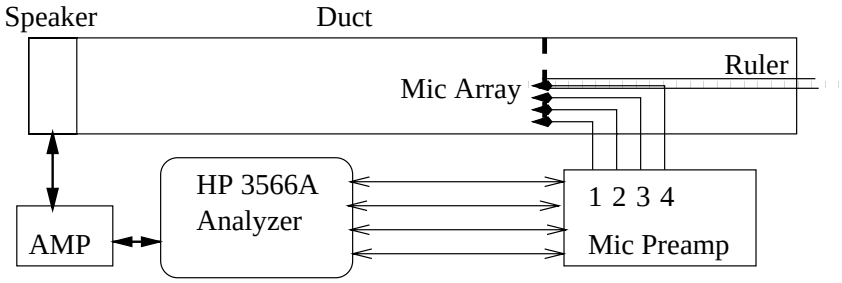

Fig. 6.5. Overall Experimental Setup

the input channels. In auto range mode the analyzer will adjust the maximum input level of each channel to ensure that the full dynamic range of the analog to digital converter is used. The analyzer has a signal-to-noise ratio of 80 dB and a matching of 0.1 dB and 0.5^o between channels.

The analyzer signal generator was set to 200mV output and the inputs were set to auto range. The speaker amplifier was adjusted so that there was a nominal 90 dB re 20 μ Pa acoustic pressure level at the end of the duct - at least 30 dB above the background noise level of the room. The frequency of the generator was swept from 400 Hz to 1800 Hz at 128 evenly spaced points. The analyzer was set so that at each measurement frequency it would wait eight cycles for the signal to settle and then integrate the input for sixteen cycles to achieve a measurement.

All the microphone inputs were referenced to the source signal from the analyzer so that the phase difference in the pressures at different horizontal and axial locations could be measured.

A diagram of the experimental configuration is shown in figure 6.5.

6.4 Data Reduction

The data measured by the signal analyzer was stored in HP's native SDF format. The data was loaded directly into MATLAB for analysis with a specially written program.

From the horizontal measurements for each axial position the modal pressures $P_M(z)$ were extracted using equation 6.9. From the modal pressures $P_M(z)$, the amplitudes A_M and B_M were extracted using equation 6.11. Errors were not included in the decomposition.

6.5 Microphone Calibration and Measurement Caveats

The standard technique for systematic microphone calibration to remove amplitude and phase differences is to expose the microphones to the same field, measure the amplitude and phase differences and use those differences to correct the measured data. An alternate method is the "switching" calibration method where the microphones are physically switched, the measurement redone, and the results are combined in a way to remove the microphone differences. Because of the number of microphones involved in this experiment, the "switching" calibration method is not easily employed thus the other method was used.

To expose the microphones to the same field, the microphones were placed in a 3/8 in thick aluminum plate at the end of a 1M long, 4 in diameter round PVC duct. The duct was driven by a speaker covering the entire width of the duct at the end opposite the microphones. It was found that when measuring the frequency response between

microphones with a random noise applied to the speaker, the microphone calibration was not repeatable. If the microphone was removed and replaced in the same position, the calibration would change by up to $\pm 0.5^o$ at some frequencies. The change was seemingly random - no systematic change could be found. If the plate was rotated 90^o, the calibration would change up to $\pm 0.5^o$. If the plate were rotated back, the calibration would match the previous calibration to within millidegrees. What does this say? First, the rotation results say it is *very* difficult to expose the microphones to a uniform field for calibration purposes. Second, the removal and replacement results say that since it is so difficult to get the microphones back into the same position that the switching method of calibration is essentially useless with these microphones.

A similar problem with repeatability showed itself during the measurement process. When measuring using random noise and frequency response analysis it was found that repeated experiments did not give the same results. Repeated trials were found to differ in phase by as much as 1.5^o.

A possible explanation of part of the measurement and calibration problems comes from Bendat and Piersol[5]. When using FFT analysis, the buffer length of the FFT *must* be longer than the impulse response of the system that is being measured in order to get accurate results. In the calibration tube and in the rigid walled duct, the standing wave ratio is quite high, which means the impulse response is very long. Unless an extremely long buffer length (longer than the HP analyzer allows) is used with the FFT, consistent and accurate results cannot be expected. As a caveat to would be experimenters, *make sure the length of the FFT buffer is longer than the impulse response of the system that is being measured.* A possible solution to the calibration problem is to add damping to

the calibration tube in order to reduce the length of the impulse response. However, one must be careful to add the damping far enough away from the microphones so that they are all still exposed to the same field.

Another solution to the measurement problem is to use swept sine analysis instead of random noise frequency response measurement. It was this solution that was finally used. Upon switching to swept sine analysis, consistent and repeatable results were obtained for both calibration and measurements.

It was found that the microphones matched well enough and were stable enough that phase calibration was unnecessary when the horizontal array was used. The results were repeatable and phase correction did not change the extracted modal coefficients enough to warrant the extra time that phase calibration would add to the measurement. (The match between the theoretical curves and experimental results was the same regardless of whether or not phase calibration was done.) Overall amplitude calibration was achieved as stated earlier, through the use of the individual level controls on the microphone preamplifier.

6.6 Measurement of Reflection at an Infinite Baffle

The reflection coefficient from the end of a duct mounted in an infinite baffle was calculated from measured pressures inside the duct. The "infinite" baffle was two 4 ft x 8 ft pieces of 5/8 in particle board with the duct mounted in the center as shown in figure 6.6.

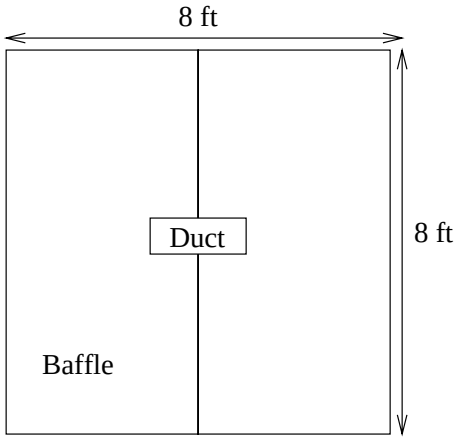

Fig. 6.6. Baffle Used for Reflection Coefficient Measurements.

Measurements of the pressure were taken at four horizontal positions (at $x = 0.5$ cm, 4.4 cm, 7.9 cm, and 14.3 cm) and at six axial positions (at $z = 15.0$ cm, 17.0 cm, 19.0 cm, 21.0 cm, 23.0 cm, and 25.0 cm) where $z = 0$ is the open end of the duct.

Figure 6.7 shows $|R_{00}|$, the magnitude of the plane wave self pressure reflection coefficient, as determined from the in duct pressure measurements compared with the theoretical results. The plot goes from $ka = pi$ to $ka = 3\pi$. The experimental results are slightly higher than the theoretical results, but the shape of the curve is correct. At about $ka = 2\pi$, the experimental results begin to show more variance. $ka = 2\pi$ is the cut-off frequency of the second horizontal mode so it is not surprising that the results are less accurate near and above that frequency.

Figure 6.8 shows $|R_{11}|$, the magnitude of pressure self reflection coefficient for the first mode, as determined from the in duct pressure measurements compared with the theoretical results. The cut-off frequency of the first horizontal mode is $ka = \pi$ so

the experimental results are not expected to be accurate below that point. Just above $ka = \pi$ the reflection coefficient is very close to unity and the standing wave field is very strong so accurate results are not expected there either. From $ka = 4$ to $ka = 2\pi$ the experimental results compare very well with the theoretical results, verifying the validity of the theory. Above the $ka = 2\pi$ cut-off frequency of the second mode the results are again less accurate.

Figure 6.9 shows $|R_{20}|$, the magnitude of the plane wave to first mode mutual pressure reflection coefficient, as determined from the in duct pressure measurements compared with the theoretical results. While the experimental results have a large variance, the theoretical results seem to be a pretty good fit through the middle of the data. Because of the low amplitude of this coefficient the measurement was expected to be difficult and the variance was expected to be large.

Overall the experimental results match the theory quite well. The theoretical curves run through the experimental curves for both self reflection coefficients and mutual reflection coefficients thus validating the theory.

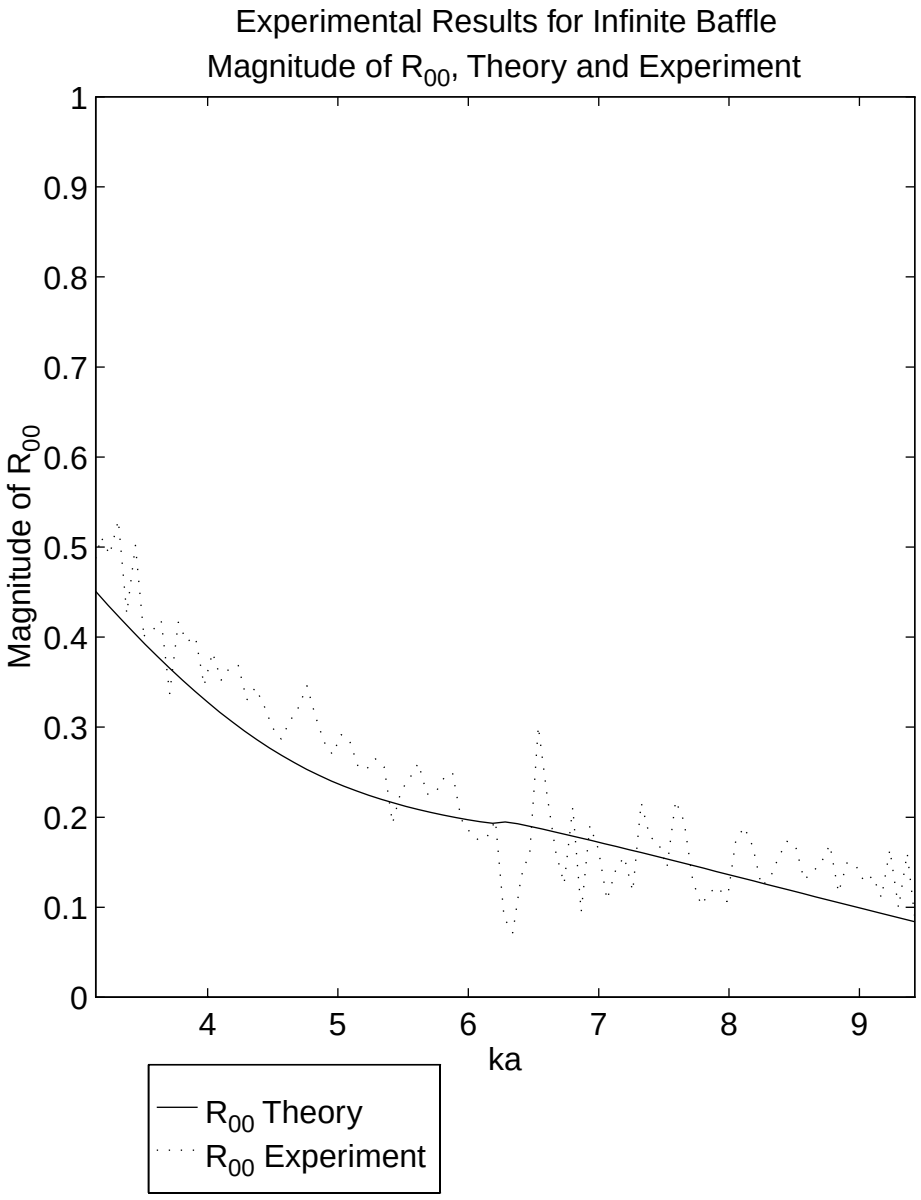

Fig. 6.7. Comparison of theoretical and experimentally determined magnitude of the plane wave mode self pressure reflection coefficient R_{00}.

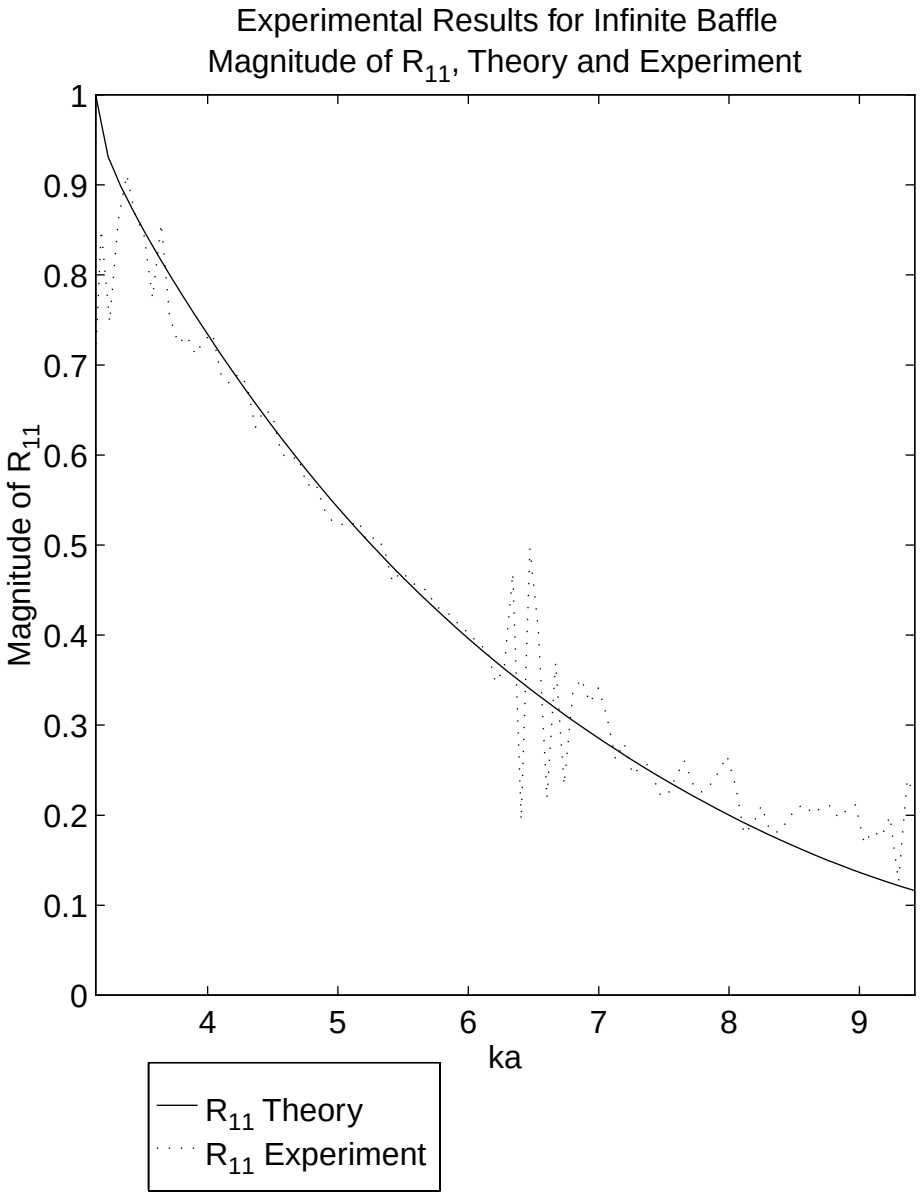

Fig. 6.8. Comparison of theoretical and experimentally determined magnitude of the first mode self pressure reflection coefficient R_{11}.

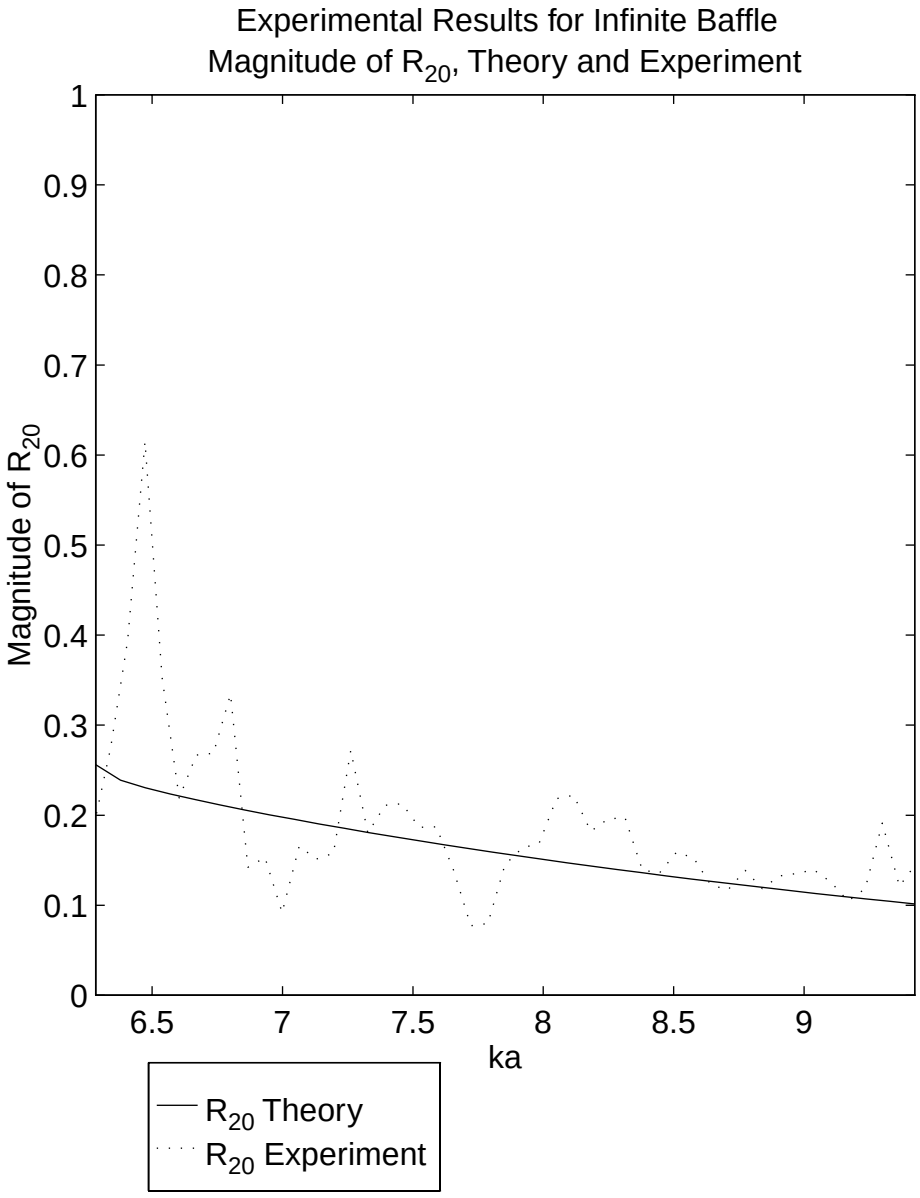

Fig. 6.9. Comparison of theoretical and experimentally determined mutual pressure reflection coefficient magnitude R_{20}.

Chapter 7

Conclusions and Suggestions For Future Research

7.1 Conclusions

While a lot of research has previously been done on duct acoustics, the literature has been severely lacking in regards to scattering of higher order modes. This thesis will help to fill the research gap in regards to rigid walled rectangular ducts.

Throughout the thesis, matrix formalisms are used to solve the resulting sets of simultaneous equations. The simultaneous equations simplify considerably in matrix form and take on familiar forms.

In chapter 3 the reflection and transmission coefficients at a step discontinuity were determined in a straight forward manner through the use of generalized scattering parameters. By solving the problem in this manner both the expansion and constriction coefficients are determined at the same time. When written in matrix form, the reflection coefficient equations take the standard form expected for reflection from an impedance boundary.

The example problems show that the self modal reflection coefficients vary quite a bit with frequency, often approaching unity at the cut-off frequencies of higher order modes. The mutual modal reflection coefficients are shown to be quite high at the cut-off frequency as well, indicating that modal coupling is significant and important in the analysis of step discontinuities.

A more difficult problem, that of a junction, is also handled in a straight forward manner using generalized scattering parameters in chapter 4. Because the Green's function of the junction region is often written as an infinite summation of normal modes, the problem can be significantly more difficult to solve than the step discontinuity. Using the matrix form of the equations, the familiar impedance discontinuity form for the scattering matrix was again obtained.

In the example problems of the right angle bend and the T junction, an infinite summation from the Green's function was able to be removed through the use of digamma functions as shown in appendix A.

The example problems show that the self modal reflection coefficients for a right angle bend start out at zero, but very quickly rise to large values indicating that a significant portion of the incident energy is reflected by the bend, even for the plane wave below the cut-off frequency of the first mode. At and above the cut-off frequency of a given higher order mode, the transmission coefficient from the plane wave to the higher order mode is usually more than the plane wave mode self transmission coefficient, indicating that modal coupling is significant and cannot be ignored in higher frequency analysis of junctions.

The theoretical solutions for the right angle bend match the experimental results of Shepherd and Cabelli quite well, with most points within the error of the measurement. These experimental results verify the junction theory.

In chapter 5 radiation impedances and reflection coefficients for a duct terminating in an infinite baffle were derived. Using the matrix formalism the equation for reflection coefficients was again shown to take the same form as that of a simple impedance discontinuity.

The graphs of the amplitude of the radiation impedance should not be too surprising - they are quite similar to that found for circular duct. It is important to note that above the cut-off frequency of the second mode, the coupling coefficient from the plane wave mode into the second mode is of higher amplitude than the self reflection coefficient of the plane wave mode. This indicates that modal coupling cannot be ignored at frequencies where higher order modes can propagate.

It was shown that the plane wave mode radiates omni-directionally at low frequencies and begins beaming at higher frequencies, while the higher order modes radiate their energy off axis, with the beams getting closer to the axis at higher frequencies.

Equations for the radiated power were derived in terms of the reflection coefficients of the duct termination. Using those equations eliminates the complicated integration of the radiated pressure usually required in determining the radiated power.

The method and results of the experiments were discussed in chapter 6. After deriving the equations describing how the modal amplitudes could be obtained from the pressure measurements, there was a discussion of measurement techniques and array types. It was argued that a horizontal array was probably the best method of determining modal amplitudes.

Some of the limitations of standard measurement and calibration techniques were discussed. In particular, it was noted that the use of FFT methods in a highly reverberant

environment is fraught with difficulties and experiments may not be repeatable. The use of complex swept sine analysis was found to reduce the problem.

Plots of experimentally measured reflection coefficients from an infinite baffled termination were shown along with the theoretical results. The measured plane wave reflection coefficient was slightly higher in amplitude than the theoretical curve, but the shape was correct. The measured amplitude of the reflection coefficient of the first higher order mode matched the theoretical amplitude very well. The measurement of the mutual coupling coefficient matched theory fairly well. The shape and level were about the same as theory, but there was far more variance in the mutual coupling coefficient measurement than with the self reflection coefficient measurement. The match between theory and experiment is close enough to verify the theory.

Overall, it is clear that modal coupling cannot be ignored at frequencies where higher order modes can propagate. Mutual modal coupling coefficients are often higher in amplitude than the modal self reflection coefficients near the cut-off frequency.

7.2 Suggestions for Future Research

The experimental results obtained for the reflection coefficient were adequate but not exemplary. The strong standing waves at resonances made taking accurate measurements difficult, even using the swept sine method. Adding damping to the source end of the duct to reduce the standing waves would probably improve the measurements. The damping must be confined to the source end so that the region near the baffled end of the duct still has rigid walls.

A knowledge of the approximate error in the measurement would be helpful. The relative error in the frequency response can be obtained from the coherence function. The position error can be easily determined. Instead of the simple decomposition algorithm developed in chapter 5, a more complicated algorithm which incorporates the measurement errors should be used [7]. This would weight measurements with large error less, and measurements with small errors more. An error bound on the reflection coefficient computed from the measurements could also be determined.

Because the design of acoustical filters is so important, the method of generalized parameters could be extended to composite structures. From the generalized parameters of a cascade of smaller systems, the overall modal response of a system, from input to output could be determined in a straight forward manner. For example, expansion and constriction chambers are merely a cascade of two step discontinuities.

Examples of only a few discontinuities were given in the thesis. A more complete set of scattering coefficients for a number of important discontinuities could be developed. Handbooks for electro-magnetic waveguides are available which show reflection and transmission coefficients for a variety of different constructions. With a similar set of acoustic coefficients the acoustic waveguide designer would be able to quickly choose the appropriate construct for the desired response.

This thesis derived radiation from a baffled duct. A more difficult and possibly more important problem is to derive expressions for radiation from an unbaffled duct. Unless a Green's function for the end of an unbaffled duct can be obtained, the full Kirchoff-Helmholtz integral will have to be used, resulting in a Fredholm integral equation which has to be solved. At this time an analytic solution to the problem is

unknown. Boundary element or finite element methods could be used to numerically solve the problem to obtain some theoretical results.

Appendix A

Infinite Summations Using Digamma Functions

Infinite summations of the form $\sum_{n=0}^{\infty} \frac{1}{n^2-z^2}$ or $\sum_{n=0}^{\infty} \frac{(1)^n}{n^2-z^2}$ can be rewritten in terms of the Digamma function [1, 25, 29].

The Digamma function is defined as

$$\Psi(z) = \frac{d}{dz} \ln \Gamma(z). \tag{A.1}$$

For $z \neq -1, -2, -3, ...$ the Digamma function can be expanded by the series

$$\Psi(1+z) = -\gamma + \sum_{n=1}^{\infty} \frac{z}{n(n+z)} \tag{A.2}$$

where $\gamma = 0.577215...$ is Euler's constant.

$\Psi(1-z)$ can be subtracted from the above equation to yield the identity

$$\Psi(1+z) - \Psi(1-z) = 2z \sum_{n=1}^{\infty} \frac{1}{(n^2-z^2)}. \tag{A.3}$$

The Digamma function, like many transcendental functions has various recurrence formulae (see [25] p.952-956). In particular

$$\Psi(1+z) = \Psi(z) + \frac{1}{z} \tag{A.4}$$

$$\Psi(\frac{1}{2}+z) = \Psi(\frac{1}{2}-z) + \pi\tan(\pi z) \tag{A.5}$$

and

$$\Psi(1-z) = \Psi(z) + \pi\cot(\pi z). \tag{A.6}$$

Subtracting equation A.6 from A.4 yields the identity

$$\Psi(1+z) - \Psi(1-z) = \frac{1}{z} - \pi\cot(\pi z). \tag{A.7}$$

The infinite summation has thus been reduced to a simple equation with well known functions

$$\sum_{n=1}^{\infty} \frac{1}{(n^2-z^2)} = \frac{1}{2z}\left[\frac{1}{z} - \pi\cot(\pi z)\right]. \tag{A.8}$$

The infinite summation in H_{rm}^{11} in chapter 4 is then

$$\sum_{n=0}^{\infty} \frac{1}{\Lambda(n)(n^2-z^2)} = -\frac{\pi}{z}\cot(\pi z). \tag{A.9}$$

An alternating summation can also be written in terms of the Digamma function since

$$\sum_{n=0}^{\infty} \frac{(-1)^n}{(n+z)} = \beta(z) = \frac{1}{2}\left[\psi(\frac{1+z}{2}) - \psi(\frac{z}{2})\right]. \tag{A.10}$$

Using partial fraction expansion and equation A.5

$$\sum_{n=0}^{\infty} \frac{(-1)^n}{(n^2-z^2)} = \frac{1}{2z}\sum_{n=0}^{\infty} \frac{(-1)^n}{(n-z)} - \frac{(-1)^n}{(n+z)} = \frac{1}{4z}\left[\Psi(\frac{z}{2}) - \Psi(-\frac{z}{2}) - \pi\tan(\pi\frac{z}{2})\right]. \tag{A.11}$$

The remaining two Ψ functions can be removed by using the recurrence relations to show

$$\Psi(-\frac{z}{2}) = \Psi(1-\frac{z}{2}) - \frac{2}{z} = \Psi(\frac{z}{2}) + \pi\cot(\pi\frac{z}{2}). \tag{A.12}$$

And so finally

$$\sum_{n=0}^{\infty} \frac{(-1)^n}{(n^2-z^2)} = \frac{1}{4z}\left[\frac{2}{z} - \pi\tan(\pi\frac{z}{2}) - \pi\cot(\pi\frac{2}{z})\right]. \tag{A.13}$$

With this result the summation for H_{rm}^{13} can be written

$$\sum_{n=0}^{\infty} \frac{(-1)^n}{\Lambda(n)(n^2-z^2)} = -\frac{\pi}{2z}\left[\tan(\pi\frac{z}{2}) + \pi\cot(\pi\frac{z}{2})\right]. \tag{A.14}$$

Appendix B

Alternate Representation of Z_{rRM}

B.1 Conversion to a Convolution Integral

In chapter 4 it was shown that for a baffled duct the elements of the radiation impedance matrix are given by the expression

$$Z_{rRM} = \frac{jk\rho c}{2\pi} \iint_{\mathcal{S}} \iint_{\mathcal{S}} \psi_R(x,y)\psi_M(x_0,y_0) \frac{e^{-jk\sqrt{(x-x_0)^2+(y-y_0)^2}}}{\sqrt{(x-x_0)^2+(y-y_0)^2}} dx_0 dy_0 dx dy. \quad \text{(B.1)}$$

where $\psi_M(x,y)$ are the modes of the duct.

Equation B.1 is a four dimensional integral that is often impossible to solve analytically. It can be solved analytically for cylindrical ducts, but not rectangular ducts. Since the integral is four dimensional and singular whenever $x = x_0$ and $y = y_0$, it may also be difficult to compute numerically. Using the technique of wavenumber transforms the integral can be converted into another form which may be computationally easier to handle.

The Green's function in B.1, e^{-jkr}/r, is merely a function of the difference in positions x and x_0 and y and y_0. The integral over either x and y or x_0 and y_0 can be viewed as a convolution integral. To see the convolution integral more clearly, equation

B.1 can be rewritten

$$Z_{rRM} = \frac{jk\rho c}{2\pi} \iint_{\mathcal{S}} \psi_R(x,y) \left[\iint_{\mathcal{S}} \psi_M(x_0,y_0) \frac{e^{-jk\sqrt{(x-x_0)^2+(y-y_0)^2}}}{\sqrt{(x-x_0)^2+(y-y_0)^2}} dx_0 dy_0 \right] dxdy. \quad \text{(B.2)}$$

If $\psi_M(x_0, y_0) = 0$ outside the duct, the term in brackets in equation B.2 is a convolution integral. Denoting the spatial convolution by $*$ equation B.2 can be rewritten

$$Z_{rRM} = \frac{jk\rho c}{2\pi} \iint_{\mathcal{S}} \psi_R(x,y) \left[\psi_M(x_0,y_0) * \left(\frac{e^{-jk\sqrt{(x-x_0)^2+(y-y_0)^2}}}{\sqrt{(x-x_0)^2+(y-y_0)^2}} \right) \right] dxdy. \quad \text{(B.3)}$$

B.2 Review of Wavenumber Transforms

Just as standard Fourier transforms are a useful tool for analyzing time domain waveforms, the spatial Fourier transform or wavenumber transform is a useful tool in analyzing spatial waveforms. In the time domain Fourier transform, time is transformed into frequency. In the spatial Fourier transform, spatial coordinates are transformed into *wavenumbers*, hence the term wavenumber transform.

The forward wavenumber transform is defined as

$$F(k_x, k_y, k_z, \omega) = \int_{-\infty}^{\infty} \iiint f(x,y,z,\omega) e^{-jk_x x} e^{-jk_y y} e^{-jk_z z} dxdydz. \quad \text{(B.4)}$$

The inverse wavenumber transform is defined as

$$f(x,y,z,\omega) = \frac{1}{(2\pi)^3} \int_{-\infty}^{\infty} \iiint F(k_x, k_y, k_z, \omega) e^{jk_x x} e^{jk_y y} e^{jk_z z} dk_x dk_y dk_z. \quad \text{(B.5)}$$

Just like time domain Fourier transforms, there is a large number of special properties associated with wavenumber transforms. One of these properties is the convolution property.

The convolution theorem of wavenumber transforms as stated in Bracewell [8] states that the wavenumber transform of the convolution of two functions is the product of their wavenumber transforms. In two dimensions the convolution integral is written

$$f(x,y) * g(x,y) = \iint_{-\infty}^{\infty} f(x',y')g(x-x',y-y')dx'dy' \tag{B.6}$$

$$= \frac{1}{(2\pi)^2}\iint_{-\infty}^{\infty} F(k_x,k_y)G(k_x,k_y) \times e^{jk_x x}e^{jk_y y}dk_x dk_y. \tag{B.7}$$

For a baffled duct the Green's function is $G(x-x_0, y-y_0) = e^{-jkr}/r$, where the distance $r = \sqrt{(x-x_0)^2+(y-y_0)^2}$. The wavenumber transform of the baffled Green's function is then

$$G_k(k_x,k_y) = \iint_{-\infty}^{\infty} \frac{e^{-jk\sqrt{(x-x_0)^2+(y-y_0)^2}}}{\sqrt{(x-x_0)^2+(y-y_0)^2}} e^{-jk_x x}e^{-jk_y y}dx_0 dy_0 = \frac{-je^{jk_x x}e^{jk_y y}}{\sqrt{k^2-k_x^2-k_y^2}}. \tag{B.8}$$

In computing the wavenumber transform of $\psi_M(x,y)$ it must be noted that $\psi_M(x,y)$ is confined to the duct region. It is standard practice to define $\psi_M(x,y) = 0$ outside the duct.With this definition the wavenumber transform of of $\psi_M(x,y)$ is

$$\Psi_M(k_x,k_y) = \iint_{-\infty}^{\infty} \psi_M(x,y)e^{-jk_x x}e^{-jk_y y}dxdy = \iint_{\mathcal{S}} \psi_M(x,y)e^{-jk_x x}e^{-jk_y y}dxdy. \tag{B.9}$$

B.3 Transformation of Z_{rRM}

Using the wavenumber transform for the Green's function and the convolution property of wavenumber transforms discussed above, equation B.3 can be rewritten as

$$Z_{rRM} = \frac{k\rho c}{4\pi^2} \iint_{\mathcal{S}} \psi_R(x,y) \left[\iint_{-\infty}^{\infty} \frac{\Psi_M(k_x,k_y)}{\sqrt{k^2-k_x^2-k_y^2}} e^{jk_x x} e^{jk_y y} dk_x dk_y \right] dxdy \tag{B.10}$$

where $\Psi_M(k_x,k_y)$ is the wavenumber transform of $\psi_M(x,y)$.

This can be rearranged once again to form

$$Z_{rRM} = \frac{k\rho c}{4\pi^2} \iint_{-\infty}^{\infty} \frac{\Psi_M(k_x,k_y)}{\sqrt{k^2-k_x^2-k_y^2}} \left[\iint_{\mathcal{S}} \psi_R(x,y) e^{jk_x x} e^{jk_y y} dk_x dk_y \right] dxdy. \tag{B.11}$$

The remaining spatial integral is the same as equation B.9 with k_x replace by $-k_x$ and k_y replaced by $-k_y$. So, one can replace the spatial integration with $\Psi_M(-k_x,-k_y)$ to yield

$$Z_{rRM} = \frac{k\rho c}{4\pi^2} \iint_{-\infty}^{\infty} \frac{\Psi_M(k_x,k_y)\Psi_R(-k_x,-k_y)}{\sqrt{k^2-k_x^2-k_y^2}} e^{jk_x x} e^{jk_y y} dk_x dk_y. \tag{B.12}$$

At this point a finite four dimensional integral which was singular at many points has been reduced to a two dimensional infinite integral which is also singular at many points. This may or may not be easier to deal with computationally. But, the integral can be reduced once again by rewriting it in polar coordinates. The final result is

$$Z_{rRM} = \frac{k\rho c}{4\pi^2} \int_0^{\infty} \int_0^{2\pi} \frac{\Psi_M(\mu\cos\theta,\mu\sin\theta)\Psi_R(-\mu\cos\theta,-\mu\sin\theta)}{\sqrt{k^2-\mu^2}} \mu d\mu d\theta. \tag{B.13}$$

where $k_x = \mu\cos\theta$ and $k_y = \mu\sin\theta$.

This two dimensional integral is infinite in only one dimension and is singular at only one point. Depending upon the form of $\Psi_M(k_x, k_y)$ equation B.13 may be much easier to compute than B.1 or B.12.

B.4 Application to a Rectangular Duct

For a rectangular duct the $\psi_M(x,y) = \cos(\frac{m_x\pi}{a})\cos(\frac{m_y\pi}{b})$. In order compute Z_{rRM} using equations $B.12$ or $B.13$ the wavenumber transform $\Psi_M(k_x, k_y)$ must be computed.

$$\Psi_M(k_x, ky) = \int_0^a \int_0^b \frac{\cos(\frac{m_x\pi}{a}x)\cos(\frac{m_y\pi}{b}y)}{\sqrt{ab\Lambda_{m_x}\Lambda_{m_y}}} e^{-jk_x x} e^{-jk_y y} dxdy. \tag{B.14}$$

When $\frac{m_x\pi}{a} \neq k_x$ and $\frac{m_y\pi}{b} \neq k_y$

$$\Psi_M(k_x, k_y) = \frac{-k_x k_y [1-(-1)^{m_x} e^{-jk_x a}][1-(-1)^{m_y} e^{-jk_y b}]}{\sqrt{ab\Lambda_{m_x}\Lambda_{m_y}}[(\frac{m_x\pi}{a})^2 - k_x^2][(\frac{m_y\pi}{b})^2 - k_y^2]}. \tag{B.15}$$

When $\frac{m_x\pi}{a} = k_x$ but $\frac{m_y\pi}{b} \neq k_y$

$$\Psi_M(k_x, k_y) = \frac{j\sqrt{a}k_y [1-(-1)^{m_y} e^{-jk_y b}]}{\sqrt{b\Lambda_{m_y}}[(\frac{m_y\pi}{b})^2 - k_y^2]}. \tag{B.16}$$

When $\frac{m_x\pi}{a} \neq k_x$ but $\frac{m_y\pi}{b} = k_y$

$$\Psi_M(k_x, k_y) = \frac{j\sqrt{b}k_x [1-(-1)^{m_x} e^{-jk_x a}]}{\sqrt{a\Lambda_{m_x}}[(\frac{m_x\pi}{a})^2 - k_x^2]}. \tag{B.17}$$

When $\frac{m_x\pi}{a} = k_x$ and $\frac{m_y\pi}{b} = k_y$

$$\Psi_M(k_x, k_y) = \sqrt{ab}. \tag{B.18}$$

As a check one can look at the $M = 0$, $R = 0$ term of Z_{rRM}. That term is the radiation impedance of a of a rectangular piston.

For $M = 0$ ($m_x = 0, m_y = 0$) and $R = 0$ ($r_x = 0, r_y = 0$) $k_M = k$ and the wavenumber transform of the mode becomes

$$\Psi(k_x, k_y) = \sqrt{ab}e^{-jk_x\frac{a}{2}}e^{-j_y\frac{b}{2}}\text{sinc}(k_x a/2)(\text{sinc}(k_y b/2). \tag{B.19}$$

and equation B.12 becomes

$$\begin{aligned} Z_{r00} &= \frac{k\rho c(ab)}{4\pi^2}\iint_{-\infty}^{\infty}\frac{\text{sinc}^2(k_x a/2)\text{sinc}^2(k_y b/2)}{\sqrt{k^2 - k_x^2 - k_y^2}}dk_x dk_y \\ &= \frac{k\rho c(ab)}{4\pi^2}\int_0^{\infty}\frac{\mu d\mu}{\sqrt{k^2 - \mu^2}}\int_0^{2\pi}\text{sinc}^2(\frac{\mu a\cos\theta}{2})\text{sinc}^2(\frac{\mu b\sin\theta}{2})d\theta. \end{aligned} \tag{B.20}$$

This is very similar to the equation derived by Morse and Ingard [44] in their development of the the radiation impedance of a square piston. (Morse and Ingard never explicitly derive the radiation impedance in an exact form. In equation 7.4.43 they derive and expression for the force on the piston in terms of the piston velocity. The radiation impedance can be obtained by dividing the force by the velocity and the area of the piston. The resulting equation is the same as B.20. Also note that equation 7.4.43 of [44] is missing a square root over the denominator of the integral.)

Appendix C

Numerical Integration of ζ_{RM}

Recall that for a rectangular duct, the equation for ζ_{RM} is

$$\zeta_{RM} = \frac{jk\rho c}{2\pi} \int_0^a \int_0^b \int_0^a \int_0^b \frac{\cos(\frac{m_x\pi}{a}x)}{\sqrt{a\Lambda_{m_x}}} \frac{\cos(\frac{m_y\pi}{b}y)}{\sqrt{b\Lambda_{m_y}}} \frac{\cos(\frac{m_x\pi}{a}x_0)}{\sqrt{a\Lambda_{m_x}}} \frac{\cos(\frac{m_y\pi}{b}y_0)}{\sqrt{b\Lambda_{m_y}}} \frac{e^{-jkr}}{r} dx_0 dy_0 dx dy. \tag{C.1}$$

Numerical evaluation of C.1 is not an easy process. While the four dimensional integral looks straight forward, the integrand is singular, so caution must be taken.

At frequencies low enough for only a few modes to propagate, an approximation to the integral in equation C.1 can be obtained by discretization of the region into sub-regions and approximating the integral over each sub-region. Then the integral is obtained by summation of the portion from each sub-region.

If the end of the duct is broken into a series of rectangular regions of size 2 α by 2 β equation C.1 becomes

$$\zeta_{RM} = \frac{jk\rho c}{2\pi} \sum_{\mu} \sum_{\nu} I_{\mu\nu} \tag{C.2}$$

where

$$I_{\mu\nu} = \int_{-\alpha}^{\alpha} \int_{-\beta}^{\beta} \int_{-\alpha}^{\alpha} \int_{-\beta}^{\beta} \psi_R(x_\mu + \epsilon_x, y_\mu + \epsilon_y) \psi_M(x_\nu + \delta_x, y_\nu + \delta_y) \frac{e^{-jkr}}{r} d\epsilon_x d\epsilon_y d\delta_x d\delta_y. \tag{C.3}$$

The integrals in equation C.3 can be approximated for both $\mu \neq \nu$ and $\mu = \nu$.

For $\mu \neq \nu$ standard Gaussian quadratures can be used to compute the integral over this sub-region [51].

For $\mu = \nu$ the integral in equation C.3 is singular. However, the singularity must be integrable because physically it is known that ζ_{RM} is not infinite. The singularity can be removed by a transformation into polar coordinates, but the resulting integral is still difficult to do numerically. An alternate change of variables is used by CHIEF, a program which was written to solve the integral equations resulting from acoustic radiation from a general vibrating surface [6].

Consider an integral over a rectangular region of the form

$$I = \int_{u_l}^{u_u} \int_{v_l}^{v_u} F(u', v') du' dv'. \tag{C.4}$$

The $u' - v'$ region can be broken into four triangular regions T_1, T_2, T_3, and T_4 as shown in figure C.1.

Then, the integral becomes

$$I = \iint_{T_1} + \iint_{T_2} + \iint_{T_3} + \iint_{T_4} F du' dv'. \tag{C.5}$$

Assume that the integral is singular at the center of the rectangle, at $u'_0 = (u_u - u_l)/2$ and $v'_0 = (v_u - v_l)/2$.

Consider the following change of variables in region T_1:

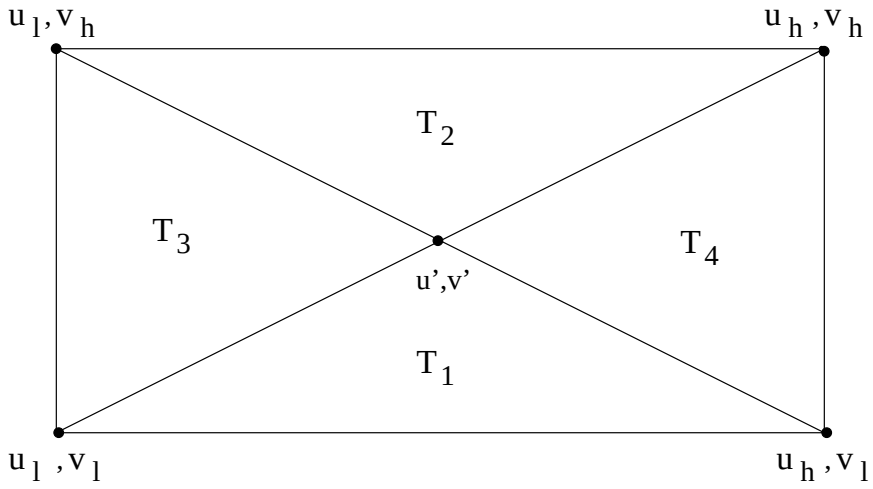

Fig. C.1. integration of the rectangular region

$$\begin{aligned} u &= u' + \xi(\frac{1+\eta}{2})(\frac{u_u - u_l}{2}) \\ v &= v' - (\frac{1+\eta}{2})(\frac{v_u - v_l}{2}). \end{aligned} \tag{C.6}$$

The determinate of the Jacobian of the transformation is

$$|\det J| = \begin{vmatrix} (\frac{1+\eta}{2})(\frac{u_u-u_l}{2}) & \frac{1}{2}\xi(\frac{u_u-u_l}{2}) \\ 0 & -\frac{1}{2}(\frac{v_u-v_l}{2}) \end{vmatrix} = \frac{1}{16}(u_u - u_l)(v_u - v_l)(1+\eta). \tag{C.7}$$

With the change of variable the integral over T_1 becomes

$$\iint_{T_1} = \int_{-1}^{+1}\int_{-1}^{+1} F(\xi,\eta)|\det J| d\xi d\eta. \tag{C.8}$$

Although $F(\xi,\eta)$ still has a singularity at $\eta=-1$, $|\det J|$ has a zero at $\eta=-1$ which cancels the singularity of F.

The integrals over T_2, T_3, and T_4 can be handled in the same manner and the results can be combined. The final result is

$$\begin{aligned} I &= \frac{1}{16}(u_u-u_l)(v_u-v_l)\int_{-1}^{1}\int_{-1}^{1}\Big\{(1+\eta)[F(u_1,v_1)+F(u_2,v_2)] \\ &\quad +(1+\xi)[F(u_3,v_3)+F(u_4,v_4)]\Big\}d\xi d\eta \end{aligned} \tag{C.9}$$

where

$$\begin{aligned} u_1 &= u_2 = u' + \xi(\frac{1+\eta}{2})(\frac{u_u-u_l}{2}) \\ v_1 &= v' - (\frac{1+\eta}{2})(\frac{v_u-v_l}{2}) \\ v_2 &= v' + (\frac{1+\eta}{2})(\frac{v_u-v_l}{2}) \\ u_3 &= u' - (\frac{1+\xi}{2})(\frac{u_u-u_l}{2}) \\ u_3 &= u' + (\frac{1+\xi}{2})(\frac{u_u-u_l}{2}) \\ v_3 &= v_4 = v' + \eta(\frac{1+\xi}{2})(\frac{v_u-v_l}{2}). \end{aligned} \tag{C.10}$$

This integral is non-singular and easier to compute using standard Gaussian quadratures than had the singularity been removed via the standard polar coordinates transformation.

References

[1] Milton Abramowitz and Irene A. Stegun. *Handbook of Mathematical Functions.* Dover, New York, 1965.

[2] George Arfken. *Mathematical Methods for Physicists, Third Edition.* Academic Press, 1985.

[3] David C. Baumann and R. A. Greiner. Modal identification approach to multi-modal cancellation. In *Proceedings of Internoise 92*, pages 341–344, 1992.

[4] David C. Baumann and R. A. Greiner. Number of error microphones for multi-modal cancellation. In *Proceedings of Internoise 92*, pages 345–348, 1992.

[5] Julius S. Bendat and Allan G. Piersol. *Engineering Applications of Correlation And Spectral Analysis.* Wiley Interscience, New York, 2 edition, 1993.

[6] G. Benthien, D. Barach, and D. Gillette. *CHIEF Users Manual, NOSC Technical Document 970.* Naval Ocean Systems Center, 1988.

[7] P. R. Bevington. *Data Reduction and Error Analysis for the Physical Sciences.* McGraw Hill, New York, 1969.

[8] Ronald N. Bracewell. *The Fourier Transform and its Applications.* McGraw Hill, New York, 1978.

[9] Jan C. Bruggeman. The propagation of low-frequency sound in a two-dimensional duct system with t joints and right angle bends: Theory and experiment. *Journal of the Acoustical Society of America*, 82(3):1045–1051, 1987.

[10] Herbert J. Carlin and Anthony B. Giordano. *Network Theory, An Introduction to Reciprocal and Nonreciprocal Circuits*. Prentice Hall, Englewood Cliffs, NJ, 1964.

[11] R. E. Collins. *Foundations for Microwave Engineering*. McGraw-Hill, New York, 1966.

[12] R. Courant and D. Hilbert. *Methods of Mathematical Physics*, volume 1. Wiley, 1989.

[13] R. Courant and D. Hilbert. *Methods of Mathematical Physics*, volume 2. Wiley, 1989.

[14] A. Craggs. A finite element method for damped acoustic systems: An application to evaluate the performance of reactive mufflers. *Journal of Sound and Vibration*, 48(3):377–392, 1976.

[15] A. Craggs. The application of the transfer matrix and matrix condensation methods with finite elements to duct acoustics. *Journal of Sound and Vibration*, 132(2):393–402, 1989.

[16] D.G. Crighton, A. P. Dowling, J. E. Ffowcs Williams, M. Heckl, and F. G. Leppington. *Modern Methods in Analytical Acoustics*. Springer-Verlag, 1992.

[17] A. Cummings. Sound transmission in 180 ° duct bends of rectangular section. *Journal of Sound and Vibration*, 41(3):321–332, 1975.

[18] P. E. Doak. Excitation, transmission and radiation of sound from source distributions in hard-walled ducts of finite length (i): The effects of duct cross-section geometry and source distription space-time pattern. *Journal of Sound and Vibration*, 31(1):1–72, 1973.

[19] P. E. Doak. Excitation, transmission and radiation of sound from source distributions in hard-walled ducts of finite length (ii): The effects of duct length. *Journal of Sound and Vibration*, 31(2):137–174, 1973.

[20] Frank Fahy. *Sound and Structural Vibration.* Academic Press, London, 1993.

[21] D. Firth and F. J. Fahy. Acoustic characteristic of ciruclar bends in pipes. *Journal of Sound and Vibration*, 97(2):287–303, 1984.

[22] C. R. Fuller. Propagation and radiation of sound from flanged circular ducts with circumferentially varying wall admittances, i: Semi-infinite ducts. *Journal of Sound and Vibration*, 93(3):321–340, 1984.

[23] G. D. Furnell and D. A. Bies. Characteristics of modal wave propagatin within longitudinally curved acoustic waveguides. *Journal of Sound and Vibration*, 130(3):405–423, 1989.

[24] G. D. Furnell and D. A. Bies. Matrix analysis of acoustic wave propagation within curved ducting systems. *Journal of Sound and Vibration*, 132(2):245–263, 1989.

[25] I. S. Gradshteyn and I. M. Ryzhik. *Table of Integrals, Series, and Products*. Academic Press, London, 5 edition, 1994.

[26] Herbert Hudde. Acoustical higher order mode scattering matrix of circular nonuniform lossy tubes without flow. *Journal of the Acoustical Society of America*, 85(6):2316–2330, 1989.

[27] Herbert Hudde and Uwe Letens. Scattering matrix of a discontinuity with a nonrigid wall in a lossless circular duct. *Journal of the Acoustical Society of America*, 78(5):1826–1837, 1985.

[28] Tatsuo Itoh, editor. *Numerical Techniques for Microwave and Millimeter-Wave Passive Structures*. Wiley-Interscience, New York, 1989.

[29] L. B. W. Jolley. *Summation of Series*. Dover, New York, 1961.

[30] Miguel C. Junger and David Feit. *Sound, Structures and Their Interaction*. MIT Press, Cambridge, Massachussettes, second edition, 1986.

[31] Cornelius Lanczos. *Linear Differential Operators*. Van Nostrad, 1961.

[32] Harold Levine and Julian Schwinger. On the radiation of sound from an unflanged circular duct. *Physical Review*, 73(4):383–406, 1948.

[33] W. K. Lippert. A method of measuring discontinuity effects in ducts. *Acoustica*, 4(2):308–312, 1954.

[34] W. K. Lippert. The meadurement of sound reflection and transmission at right-angled bends in rectangular tubes. *Acoustica*, 4(2):314–318, 1954.

[35] Robert H. Macphie and Amir I. Zaghloul. Radiation form a rectangualr waveguide with infintie flange - exact solution by the correlation matrix method. *IEEE Transactions on Microwave Theory and Techniques*, 28(4):497–503, 1980.

[36] W. P. Mason. A study of the regular combination of acoustic element, with applications to recurrent acoustic filters, taper acoustic filters, and horns. *Bell System Technical Journal*, 6:258–275, 1927.

[37] W. L. Meyer and B. T. Zinn. Sound radiation from fitie length axissymmetric ducts. *Journal of Sound and Vibration*, 90(2):286–290, 1983.

[38] John W. Miles. The analysis of plane discontinuities in cylindrical tubes. part i. *Journal of the Acoustical Society of America*, 17(3):259–271, 1945.

[39] John W. Miles. The analysis of plane discontinuities in cylindrical tubes. part ii. *Journal of the Acoustical Society of America*, 17(3):272–284, 1945.

[40] John W. Miles. The diffraction of sound due to right-angled joints in rectangular tubes. *Journal of the Acoustical Society of America*, 19(4):572–579, 1947.

[41] R. Mittra and S. W. Lee. *Analytical Techniques in the Theory of Guided Waves*. The MacMillan Company, 1971.

[42] Philip M. Morse and Herman Feshbach. *Methods of Theoretical Physics*, volume 2. McGraw Hill, 1953.

[43] Philip M. Morse and Herman Feshbach. *Methods of Theoretical Physics*, volume 1. McGraw Hill, 1953.

[44] Philip M. Morse and K. Uno Ingard. *Theoretical Acoustics*. Princeton Univerisity Press, Princeton, New Jersey, 1968.

[45] Ralph T. Muehleisen and David C. Swanson. An impedance model for actively controlled finite waveguides. *Journal of the Acoustical Society of America*, 91(4):2349, 1992.

[46] M. L. Munjal. *Acoustics of Ducts and Mufflers*. John Wiley and Sons, 1987.

[47] B. Noble. *Methods based on The Wiener-Hopf Technique for the solution of partial differential equations*. Pergamon Press Inc., 1958.

[48] A. N. Norris and I. C. Sheng. Acoustic radiation from a circular pipe with an infinite flange. *Journal of Sound and Vibration*, 135(1):85–93, 1989.

[49] T. Okoshi. *Planar Circuits for Microwaves and Lightwaves*. Springer-Verlag, Berlin, 1985.

[50] Allan D. Pierce. *Acoustics - An Introduction into Its Physical Principles and Applications*. Acoustical Society of America, Woodbury, New York, 1989 edition, 1989.

[51] William H. Press, Saul A. Teukolsky, William T. Vetterling, and Brian P. Flannery. *Numerical Recipies in Fortran*. Cambridge University Press, 2 edition, 1992.

[52] J. W. S. Rayleigh. *The Theory of Sound*, volume 2. Dover, New York, 1945.

[53] J. W. S. Rayleigh. *The Theory of Sound*, volume 1. Dover, New York, 1945.

[54] T. L. Redmore and K. A. Mulholland. The application of mode coupling theory to the transmission of sound in the sidebrance of a rectangualar duct system. *Journal of Sound and Vibration*, 85(3):323–331, 1982.

[55] S. P. Rubenstein, S. R. Popovich, D. E. Melton, and M. C. Allie. Active cancellation of higher order modes in a duct using recursively-coupled multi-channel adaptive control system. In *Proceedings of Internoise 92*, pages 337–340, 1992.

[56] Reza Safavi-Naini and Robert H. Macphie. On solving waveguide junction scattering problems by the conservation of complex power techniques. *IEEE Transactions on Microwave Theory and Techniques*, 29(4):337–343, 1981.

[57] Reza Safavi-Naini and Robert H. Macphie. Scattering at rectangular-to-rectangular waveguide junctions. *IEEE Transactions on Microwave Theory and Techniques*, 30(11):2060–2063, 1982.

[58] A. Said. Theorie der schallausbreitun in kanälen mit rechtwinkligen ecken und verzweigungen. *Acoustica*, 33(2):203–210, 1975.

[59] I. C. Shepherd and A. Cabelli. Transmission and reflection of higher order acoustic modes in a mitred duct bend. *Journal of Sound and Vibration*, 77(4):495–511, 1981.

[60] I. C. Shepherd and A. Cabelli. Duct acoustics - a numerical technique for the higher order mode solution of three-dimensional problems with rigid walls and no flow. *Journal of Sound and Vibration*, 92(3):419–426, 1984.

[61] R. J. Silcox. Active control of multi-modal random sound in ducts. Technical report, NASA Langley Research Center.

[62] J. D. Stell and R. J. Bernhard. Active control of high order acoustical modes in a seminfinite waveguide. *Transactions of the ASME, Journal of Vibration and Acoustics*, 113:523–531, 1991.

[63] J. D. Stell and R. J. Bernhard. Active control of sound in acoustic waveguides, part i: Theory. *Journal of Sound and Vibration*, 173(2):179–196, 1994.

[64] J. D. Stell and R. J. Bernhard. Active control of sound in acoustic waveguides, part ii: Considerations for implementation in ducts. *Journal of Sound and Vibration*, 173(2):197–215, 1994.

[65] J. Tichy, G. E. Warneka, and L. A. Poole. A study of active control of noise in ducts. *Transactions of the ASME, Journal of Vibration, Acoustics, Stress, and Reliability in Design*, 106:399–404, 1984.

[66] C. E. Wallace. Radiation resistance of a rectangular panel. *Journal of the Acoustical Society of America*, 51(3):946–952, 1972.

[67] K. S. Wang and T. C. Tszeng. Propagation and radiation of sound in a finite length duct. *Journal of Sound and Vibration*, 93(1):57–79, 1984.

[68] Lev Albertovich Weinstein. *The Theory of Diffraction and The Factorization Method*. The Golem Press, Boulder, Colorado, 1969.

[69] Erich Zauderer. *Partial Differential Equations of Applied Mathematics*. Wiley-Interscience, New York, 1983.

[70] William E. Zorumski. Generalized radiation impedances and reflection coefficients of circular and annular ducts. *Journal of the Acoustical Society of America*, 54(6):1667–1673, 1973.

Vita

Ralph Terry Muehleisen was born in Oconomowoc, Wisconsin on February 10, 1967. He graduated from Arrowhead High School in Hartland, Wisconsin in June of 1985. He began studies at the University of Wisconsin - Madison in August 1985. He married Sally Laurent in May of 1989. He received the Bachelor of Science degree from the University of Wisconsin - Madison with majors in Electrical and Computer Engineering and Physics in December of 1989. As a student he worked as a lab assistant in the Physics department on the Madison Symmetric Torus plasma fusion device. He also worked in the Electroacoustic Lab in the Department of Electrical and Computer Engineering. He began studies in the Graduate Program in Acoustics at Penn State in August of 1990. Upon completion of his degree Ralph plans to pursue Postdoctoral studies with his thesis advisor David Swanson at the Penn State Applied Research Lab.

During his undergraduate and graduate studies Ralph has received numerous awards. As an undergraduate he received an "Outstanding Tutor Award" in 1988 from the University of Wisconsin - Madison physics club. He was a "Dean's Fellow" of the College of Engineering at Penn State from 1990-1992. He received a "Graduate School Fellowship Honorable Mention" from the Penn State Graduate School in 1993. He received the "Outstanding Presentation by a Young Professional" award and a "Physical Acoustics Summer School Fellowship" from the Acoustical Society of America in 1992.

Ralph is a member of ASA, IEEE, the Audio Engineering Society and the Institute of Noise Control Engineers.